

## Metallicity Structure in the Milky Way Disk Revealed by Galactic H II Regions

TREY V. WENGER,<sup>1,2,3</sup> DANA S. BALSER,<sup>3</sup> L. D. ANDERSON,<sup>4,5,6</sup> AND T. M. BANIA<sup>7</sup>

<sup>1</sup>*Dominion Radio Astrophysical Observatory, Herzberg Astronomy and Astrophysics Research Centre, National Research Council, P.O. Box 248, Penticton, BC V2A 6J9, Canada.*

<sup>2</sup>*Astronomy Department, University of Virginia, P.O. Box 400325, Charlottesville, VA 22904-4325, USA.*

<sup>3</sup>*National Radio Astronomy Observatory, 520 Edgemont Road, Charlottesville, VA 22903, USA.*

<sup>4</sup>*Department of Physics and Astronomy, West Virginia University, Morgantown, WV 26505, USA.*

<sup>5</sup>*Center for Gravitational Waves and Cosmology, West Virginia University, Morgantown, Chestnut Ridge Research Building, Morgantown, WV 26505, USA.*

<sup>6</sup>*Adjunct Astronomer at the Green Bank Observatory, P.O. Box 2, Green Bank, WV 24944, USA.*

<sup>7</sup>*Institute for Astrophysical Research, Astronomy Department, Boston University, 725 Commonwealth Ave., Boston, MA 02215, USA.*

(Revised November 1, 2019, accepted for ApJ publication – tvw)

### ABSTRACT

The metallicity structure of the Milky Way disk stems from the chemodynamical evolutionary history of the Galaxy. We use the National Radio Astronomy Observatory Karl G. Jansky Very Large Array to observe  $\sim 8 - 10$  GHz hydrogen radio recombination line and radio continuum emission toward 82 Galactic H II regions. We use these data to derive the electron temperatures and metallicities for these nebulae. Since collisionally excited lines from metals (e.g., oxygen, nitrogen) are the dominant cooling mechanism in H II regions, the nebular metallicity can be inferred from the electron temperature. Including previous single dish studies, there are now 167 nebulae with radio-determined electron temperature and either parallax or kinematic distance determinations. The interferometric electron temperatures are systematically 10% larger than those found in previous single dish studies, likely due to incorrect data analysis strategies, optical depth effects, and/or the observation of different gas by the interferometer. By combining the interferometer and single dish samples, we find an oxygen abundance gradient across the Milky Way disk with a slope of  $-0.052 \pm 0.004$  dex kpc<sup>-1</sup>. We also find significant azimuthal structure in the metallicity distribution. The slope of the oxygen gradient varies by a factor of  $\sim 2$  when Galactocentric azimuths near  $\sim 30^\circ$  are compared with those near  $\sim 100^\circ$ . This azimuthal structure is consistent with simulations of Galactic chemodynamical evolution influenced by spiral arms.

**Keywords:** Galaxy: abundances – Galaxy: disk – H II regions – ISM: abundances – radio lines: ISM – surveys

### 1. INTRODUCTION

The present day chemical structure of the Milky Way disk is an important constraint on models of Galactic chemodynamical evolution (e.g., Chiappini et al. 2003; Minchev et al. 2014; Snaith et al. 2015; Minchev et al. 2018). Radial metallicity gradients, for example, are found in both the Milky Way and other spiral galaxies in studies using collisionally excited lines in ionized star forming regions (e.g., Searle 1971; Shaver et al. 1983)

and stellar abundances (e.g., Hayden et al. 2014; Bovy et al. 2014). These gradients reveal the history of star formation, stellar migration, and chemical enrichment by stars across galactic disks (Minchev et al. 2018). Stellar and gaseous tracers provide complementary information about the chemodynamical history of the Galaxy. The chemical abundances of stars represent the enrichment of the interstellar medium (ISM) when the stars were born, whereas the abundances of gaseous tracers represent the end product of billions of years of stellar evolution and ISM enrichment.

Evidence for azimuthal variations in galactic radial metallicity gradients is observed in both the Milky Way

(e.g., Balser et al. 2015, hereafter, B15) and other galaxies (e.g., Sánchez-Menguiano et al. 2016, 2017; Ho et al. 2017, 2018). Azimuthal abundance variations in the Milky Way are identified in multiple elements and tracers, such as the oxygen abundances of H II regions (e.g., B15) and the iron abundances of Cepheids (e.g., Luck et al. 2006; Pedicelli et al. 2009). Such variations are not expected in an old and well-mixed galaxy (Balser et al. 2011), and chemodynamical models of galaxies typically assume axisymmetric metallicity gradients (e.g., Chiappini et al. 2003). Azimuthal variations may be caused by streaming motions and radial migration induced by galactic bars (Di Matteo et al. 2013), spiral arms (Grand et al. 2016; Ho et al. 2017; Spitoni et al. 2019; Mollá et al. 2019b), and/or perturbations from minor galaxy interactions (Bird et al. 2012).

Here we expand the Galactic H II region metallicity surveys of Quireza et al. (2006b), Balser et al. (2011), and B15 to create a more complete map of metallicity structure in the Milky Way disk and to search for evidence of azimuthal variations in the Galactic radial metallicity gradient. H II regions are the sites of recent high-mass star formation. These nebulae are an ideal tracer of Galactic metallicity structure because (1) they live for  $\lesssim 10$  Myr, and they therefore reveal the current enrichment of the ISM; (2) their distances can be derived accurately using maser parallax measurements (e.g., Reid et al. 2014) or kinematic techniques (e.g., Wenger et al. 2018); and (3) their metallicities are easily derived using optical and infrared collisionally excited lines or inferred from the nebular electron temperatures. The radio recombination line (RRL) and radio continuum emission from H II regions are an extinction-free diagnostic of the nebular electron temperature (Mezger & Henderson 1967), which is empirically related to the H II region metallicity (Shaver et al. 1983). Radio wavelength observations of H II regions can reveal metallicity structure across the Milky Way disk due to the lack of dust extinction.

The local thermodynamic equilibrium (LTE) electron temperature of an ionized gas can be derived from the RRL-to-continuum brightness ratio when the nebula is optically thin (B15). The electron temperature surveys of Galactic H II regions by B15, Balser et al. (2011), and Quireza et al. (2006b) used single dish telescopes. Although these instruments are extremely sensitive to faint RRL emission, they are not ideal for measuring accurate RRL-to-continuum brightness ratios because of the uncertainties in the continuum brightnesses. The single dish continuum brightness of an H II region is measured by scanning the telescope across the source in multiple directions. Then, a baseline fit to the diffuse background

continuum emission is removed. The accuracy of the radio continuum brightness is limited by the ability to accurately remove this diffuse component.

An interferometer is the ideal tool for measuring the RRL-to-continuum brightness ratio of Galactic H II regions. By their nature, interferometers are not sensitive to large scale, diffuse emission, such as the non-thermal radio continuum emission that permeates the Galactic plane. We measure the total continuum flux density of nebulae more accurately with an interferometer than with a single dish telescope if the angular size of the source is smaller than the largest angular scale of the telescope. Too, interferometer data can be constructed as a high angular resolution image or data cube. These images and cubes reduce source confusion and can provide maps of electron temperature variations across a resolved nebula. Finally, interferometers like the National Radio Astronomy Observatory (NRAO) Karl G. Jansky Very Large Array (VLA) simultaneously measure both radio continuum and RRL emission. Any systematic calibration or weather issues affecting the data will be removed in the RRL-to-continuum flux ratio.

We use the VLA to derive the nebular electron temperatures and metallicities of Galactic H II regions across the Milky Way disk. A subset of these nebulae overlap with previous single dish surveys, which allows us to compare the interferometer-derived electron temperatures with those derived from single dish observations.

## 2. TARGET SAMPLE

Recent RRL surveys have more than doubled the number of known Galactic H II regions (Bania et al. 2010, 2012; Anderson et al. 2014, 2015a,b, 2018; Wenger et al. 2019). The *Widefield Infrared Survey Explorer (WISE)* Catalog of Galactic H II Regions (hereafter, *WISE* Catalog) contains the infrared and radio properties of more than 2000 known nebulae (Anderson et al. 2014). To derive accurate electron temperatures, we require the subset of *WISE* Catalog nebulae observable by the VLA. Our selection criteria are nebulae with 1) a single RRL velocity component, 2) a maser parallax measurement or an accurate kinematic distance, and 3) a predicted RRL flux density  $> 1.7 \text{ mJy beam}^{-1}$ .

When this survey began, the *WISE* Catalog contained RRL measurements of  $\sim 1200$  unique Galactic H II regions. Many of these nebulae are clustered in H II region groups or complexes, and a single dish observation will see the combined emission from multiple discrete sources. These star forming complexes are the source of ionizing photons, which may leak out into and ionize the diffuse ISM. In these cases, the RRL spectrum of the H II region will show multiple velocity components

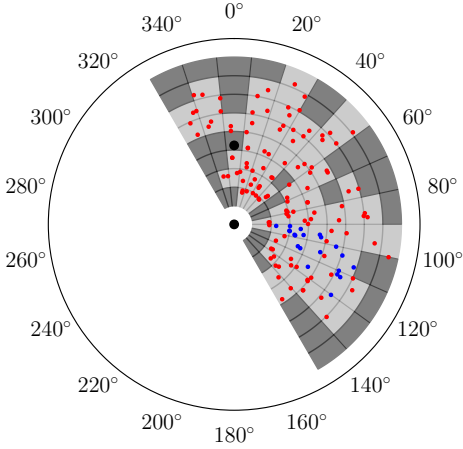


**Figure 1.** Galactocentric positions and Milky Way disk coverage of the VLA survey H II regions. The Galactic Center is the black point at the origin and the Sun is the black point 8.34 kpc in the direction  $\theta = 0^\circ$ . The colored points are the H II regions in the pilot survey (blue) and main survey (red). The Galactic disk is divided into 120 bins of size  $12^\circ$  in Galactocentric azimuth, over the azimuth range  $-30^\circ$  to  $150^\circ$ , and 2 kpc in Galactocentric radius, up to 18 kpc. Bins that contain at least one nebulae are colored light gray, whereas empty bins are dark gray.

from either multiple discrete H II regions or a mix of H II regions and diffuse ionized gas. The presence of spectrally confused, or blended, RRL components will limit our ability to derive the nebular RRL flux density accurately. Therefore, we remove  $\sim 100$  nebulae with multiple velocity component RRLs in the *WISE* Catalog.

In order to study Galactic metallicity structure, accurate distances to tracers are needed. Therefore, we further limit the *WISE* Catalog sample to those nebulae with published maser parallax measurements and/or accurate kinematic distances. We adopt the kinematic distance uncertainty model of Anderson et al. (2012) to estimate the accuracy of kinematic distances in the *WISE* Catalog. Because we aim to generate a Galactocentric map of the Milky Way metallicity structure, we require kinematic distance accuracies such that the uncertainty in the Galactocentric radius is  $\sigma_R < 2$  kpc and the uncertainty in Galactocentric azimuth is  $\sigma_\theta < 20^\circ$ . Out of our sample of  $\sim 1100$  single velocity RRL component nebulae, 107 have an associated maser parallax measurement and 364 have a kinematic distance meeting these accuracy thresholds. This brings our total sample of H II regions to 471 nebulae.

Finally, we identify the subset of this sample with previously measured RRL flux densities bright enough to be detected by the VLA in a 10 minute observation. The point source sensitivity of the VLA with this integra-

tion time is  $\sim 2 \text{ mJy beam}^{-1}$  per 31.25 kHz channel at  $\sim 9$  GHz. By smoothing the spectra to  $5 \text{ km s}^{-1}$  resolution and averaging 7 hydrogen RRL transitions, we estimate a spectral rms noise of  $\sim 0.3 \text{ mJy beam}^{-1}$  per channel. We thus require our sample of H II regions to have a predicted 9 GHz RRL flux density greater than 5 times this sensitivity limit,  $\sim 1.7 \text{ mJy beam}^{-1}$ .

All previously measured RRL flux densities of northern sky H II regions in the *WISE* catalog were made with single dish telescopes around  $\sim 9$  GHz. We first scale the observed RRL brightness temperatures to exactly 9 GHz assuming the RRL brightness temperature is proportional to the RRL frequency (B15). We convert these scaled RRL brightness temperatures to point source flux densities assuming telescope gains of  $\sim 2 \text{ K Jy}^{-1}$  for the Green Bank Observatory (GBO) Green Bank Telescope (GBT; Balser et al. 2011),  $\sim 0.27 \text{ K Jy}^{-1}$  for the NRAO 140 Foot Telescope (hereafter, 140 Foot; Balser et al. 2016), and  $\sim 5 \text{ K Jy}^{-1}$  for the Arecibo Observatory (Bania et al. 2012). Any source with a predicted 9 GHz RRL flux density  $S_{L,9\text{GHz}} > 1.7 \text{ mJy beam}^{-1}$  fulfills our sensitivity criterion. This threshold removes only 10 nebulae from our sample, bringing the total number of observable H II regions to 461.

The VLA is not sensitive to emission on scales larger than  $\sim 145$  arcsec in the D (most compact) configuration at  $\sim 9$  GHz. If we assume that the radio size of an H II region is approximately half of the infrared size (e.g., Bihr et al. 2016), then 30% of the H II regions in our sample have radio diameters greater than this largest angular scale. Our observations will not be sensitive to these angularly large nebulae if their emission is uniform on such large spatial scales. We expect to detect clumpy emission within these large H II regions, however, so we do not use any size restriction when defining our sample.

Finally, we select our observing targets from this sample of 461 nebulae to maximize our coverage of the Galactic disk. We divide the Galaxy into 120 bins of size  $12^\circ$  in Galactocentric azimuth, over the azimuth range  $-30^\circ$  to  $150^\circ$ , and 2 kpc in Galactocentric radius, up to 18 kpc. Using the maser parallax distance, when available, or the *WISE* Catalog kinematic distance to compute the Galactocentric radii and azimuths of the nebulae, we identify the two brightest and most compact H II regions in each bin. Some bins only have one (or zero) nebulae that meet our distance accuracy and predicted RRL flux density requirements. Figure 1 shows the Galactocentric positions of the 128 H II regions we select using these criteria as well as the 20 nebulae observed in the pilot survey. One H II region, G032.272–0.226, is observed in both the pilot survey and main survey. Of the 120 position bins, 78 (65%)

Table 1. Survey Targets

Field	Project	R.A. J2000 (hh:mm:ss)	Decl. J2000 (dd:mm:ss)	$R_{\text{IR}}$ (arcsec)	$S_{9\text{ GHz}, L}$ (mJy beam <sup>-1</sup> )	Telescope <sup>a</sup>	RRL Author <sup>b</sup>	$S_L/S_C$	$T_e$ (K)	$T_e$ Author <sup>c</sup>
G005.883-0.399	15B-178	18:00:31.5	-24:04:18.9	22.35	844.15 ± 5.77	140 Foot	Q06	...	...	...
G009.598+0.199	15B-178	18:06:11.1	-20:32:36.5	34.09	226.92 ± 20.00	140 Foot	L89	...	...	...
G010.596-0.381	15B-178	18:10:24.6	-19:57:08.4	60.00	586.69 ± 4.23	140 Foot	Q06	0.0686 ± 0.0006	9810 ± 90	Q06b;B15
G012.804-0.207	15B-178	18:14:15.0	-17:55:56.4	21.15	3034.62 ± 23.85	140 Foot	Q06	0.0808 ± 0.0007	7620 ± 100	Q06b;B15
G013.880+0.285	15B-178	18:14:35.7	-16:45:09.7	144.31	587.42 ± 5.00	140 Foot	Q06	0.1210 ± 0.0012	6960 ± 80	Q06b;B15
G015.212+0.167	15B-178	18:17:40.0	-15:38:13.8	176.72	10.95 ± 0.11	GBT	A15b	...	...	...
G017.336-0.146	15B-178	18:22:57.2	-13:54:41.0	102.77	6.70 ± 0.18	GBT	A11	...	...	...
G017.928-0.677	15B-178	18:26:01.7	-13:38:14.6	164.84	13.00 ± 0.30	GBT	A11	...	...	...
G018.584+0.344	15B-178	18:23:34.9	-12:34:48.7	42.50	14.00 ± 0.28	GBT	A11	...	...	...
G019.030+0.423	15B-178	18:24:09.0	-12:08:53.0	77.79	4.05 ± 0.38	GBT	A11	...	...	...
G019.716-0.261	15B-178	18:27:56.0	-11:51:39.4	58.90	14.80 ± 0.27	GBT	A15b	...	...	...
G019.728-0.113	15B-178	18:27:25.2	-11:46:55.1	42.50	7.70 ± 0.20	GBT	A11	...	...	...
G020.227+0.110	15B-178	18:27:33.8	-11:14:11.4	71.07	5.25 ± 0.12	GBT	A11	...	...	...
G020.363-0.014	15B-178	18:28:16.1	-11:10:25.6	42.50	10.90 ± 0.24	GBT	A11	...	...	...
G021.386-0.255	15B-178	18:31:04.0	-10:22:43.4	57.60	15.65 ± 0.14	GBT	A11	...	...	...
G021.603-0.169	15B-178	18:31:10.0	-10:08:48.4	31.87	4.10 ± 0.20	GBT	A15b	...	...	...
G023.041-0.399	15B-178	18:34:41.3	-8:58:37.1	151.85	65.35 ± 0.66	GBT	A11	...	...	...
G023.423-0.216	15B-178	18:34:44.5	-8:33:10.9	96.79	816.54 ± 3.65	140 Foot	Q06	0.1162 ± 0.0008	6500 ± 55	Q06b;B15
G023.661-0.252	15B-178	18:35:18.9	-8:21:34.2	56.59	24.30 ± 0.23	GBT	A11	...	...	...
G023.787+0.223	15B-178	18:33:50.6	-8:01:42.3	189.71	146.15 ± 22.69	140 Foot	L89	...	...	...
G024.185+0.211	15B-178	18:34:37.6	-7:40:51.3	178.07	176.92 ± 16.15	140 Foot	L89	...	...	...
G024.724-0.084	15B-178	18:36:41.1	-7:20:16.7	254.14	253.85 ± 26.92	140 Foot	L89	...	...	...
G024.728+0.159	15B-178	18:35:49.5	-7:13:20.1	75.57	42.20 ± 0.25	GBT	A11	...	...	...
G024.734+0.087	15B-178	18:36:05.6	-7:15:01.3	85.58	93.95 ± 0.50	GBT	A11	...	...	...
G025.397+0.033	15B-178	18:37:30.8	-6:41:08.8	39.69	88.46 ± 10.38	140 Foot	L89	...	...	...
G025.398+0.562	15B-178	18:35:37.4	-6:26:34.0	42.50	23.25 ± 0.15	GBT	A11	...	...	...

Table 1 continued

Table 1 (*continued*)

Field	Project	R.A. J2000 (hh:mm:ss)	Decl. J2000 (dd:mm:ss)	$R_{\text{IR}}$ (arcsec)	$S_9$ GHz, $L$ (mJy beam $^{-1}$ )	Telescope <sup>a</sup>	RRL Author <sup>b</sup>	$S_L/S_C$	$T_e$ (K)	$T_e$ Author <sup>c</sup>
G025.477+0.040	15B-178	18:37:38.2	-6:36:45.1	42.50	4.60 ± 0.20	GBT	A11	...	...	...
G026.597-0.024	15B-178	18:39:55.9	-5:38:45.0	26.61	16.65 ± 0.25	GBT	A15a	...	...	...
G027.210+0.282	15B-178	18:39:58.0	-4:57:39.4	42.50	6.00 ± 0.17	GBT	A15b	...	...	...
G027.562+0.084	13A-030	18:41:19.3	-4:44:21.4	42.50	22.60 ± 0.15	GBT	A11	0.1601 ± 0.0021	5827 ± 94	B11;B15
G028.320+1.243	15B-178	18:38:34.9	-3:32:04.8	60.00	2.25 ± 0.10	GBT	A15b	...	...	...
G028.451+0.001	15B-178	18:43:14.9	-3:59:11.0	28.70	9.20 ± 0.20	GBT	A15b	...	...	...
G028.581+0.145	15B-178	18:42:58.4	-3:48:18.8	42.50	6.75 ± 0.10	GBT	A11	...	...	...
G029.019+0.165	15B-178	18:43:42.1	-3:24:19.3	106.80	14.35 ± 0.19	GBT	A11	...	...	...
G029.770+0.219	15B-178	18:44:53.2	-2:42:49.6	42.50	7.60 ± 0.10	GBT	A11	...	...	...
G029.816+2.225	15B-178	18:37:49.6	-1:45:17.9	168.83	9.25 ± 0.16	GBT	A15b	...	...	...
G029.956-0.020	15B-178	18:46:04.5	-2:39:25.2	94.36	896.81 ± 3.69	140 Foot	Q06	0.0992 ± 0.0064	6510 ± 90	Q06b;B15
G030.211+0.428	15B-178	18:44:56.7	-2:13:30.7	37.11	2.75 ± 0.20	GBT	A15b	...	...	...
G031.269+0.064	15B-178	18:48:10.6	-1:27:00.7	24.84	92.31 ± 10.38	140 Foot	L89	...	...	...
G031.274+0.485	13A-030	18:46:41.9	-1:15:43.8	83.38	4.15 ± 0.10	GBT	A11	0.0944 ± 0.0042	8690 ± 462	B11;B15
G031.577+0.103	15B-178	18:48:35.9	-1:09:28.0	117.27	80.77 ± 8.46	140 Foot	L89	...	...	...
G032.030+0.048	15B-178	18:49:37.2	+0:46:47.7	42.50	6.35 ± 0.13	GBT	A11	...	...	...
G032.272-0.226	13A-030	18:51:02.3	+0:41:25.4	42.50	32.90 ± 0.14	GBT	A11	0.0889 ± 0.0008	8238 ± 104	B11;B15
G032.272-0.226	15B-178	18:51:02.3	+0:41:25.4	42.50	32.90 ± 0.14	GBT	A11	0.0889 ± 0.0008	8238 ± 104	B11;B15
G032.733+0.209	13A-030	18:50:19.9	+0:04:54.3	42.50	11.95 ± 0.27	GBT	A11	0.1638 ± 0.0037	5856 ± 156	B11;B15
G032.876-0.423	13A-030	18:52:50.7	+0:14:57.6	126.62	15.20 ± 0.32	GBT	A11	0.1817 ± 0.0043	6074 ± 176	B11;B15
G032.928+0.607	13A-030	18:49:16.4	+0:16:22.3	65.68	25.60 ± 0.09	GBT	A11	0.0680 ± 0.0006	9843 ± 170	B11;B15
G032.976-0.334	13A-030	18:52:44.0	+0:06:31.4	131.80	12.50 ± 0.20	GBT	A11	0.1485 ± 0.0040	6411 ± 207	B11;B15
G033.643-0.229	15B-178	18:53:32.9	+0:31:44.7	42.50	3.35 ± 0.16	GBT	A11	...	...	...
G034.041+0.053	13A-030	18:53:16.4	+1:00:40.2	42.50	19.45 ± 0.20	GBT	A11	0.1384 ± 0.0021	6105 ± 120	B11;B15
G034.133+0.471	13A-030	18:51:57.1	+1:17:01.3	42.50	58.55 ± 0.18	GBT	A11	0.1021 ± 0.0005	7655 ± 63	B11;B15
G034.686+0.068	13A-030	18:54:23.8	+1:35:31.5	42.50	21.75 ± 0.15	GBT	A11	0.1492 ± 0.0026	5335 ± 112	B11;B15
G035.126-0.755	15B-178	18:58:07.6	+1:36:30.0	169.39	36.85 ± 0.26	GBT	A15b	...	...	...
G035.948-0.149	15B-178	18:57:28.4	+2:37:01.0	42.50	3.35 ± 0.21	GBT	A11	...	...	...
G036.918+0.482	15B-178	18:56:59.9	+3:46:04.5	29.02	6.25 ± 0.17	GBT	A11	...	...	...

Table 1 (*continued*)

Table 1 (*continued*)

Field	Project	R.A. J2000 (hh:mm:ss)	Decl. J2000 (dd:mm:ss)	$R_{\text{IR}}$ (arcsec)	$S_9$ GHz, $L$ (mJy beam $^{-1}$ )	Telescope <sup>a</sup>	RRL Author <sup>b</sup>	$S_L/S_C$	$T_e$ (K)	$T_e$ Author <sup>c</sup>
G037.445−0.212	15B-178	19:00:26.2	+3:55:11.2	124.08	17.35 ± 0.15	GBT	A11	...	...	...
G037.469−0.105	15B-178	19:00:05.9	+3:59:22.0	41.03	5.14 ± 0.10	Arecibo	B12	...	...	...
G038.550+0.163	13A-030	19:01:07.7	+5:04:22.6	42.50	15.50 ± 0.20	GBT	A11	0.1008 ± 0.0016	8216 ± 167	B11;B15
G038.643−0.227	15B-178	19:02:41.5	+4:58:37.5	42.50	5.30 ± 0.09	GBT	A11	...	...	...
G038.651+0.087	13A-030	19:01:35.3	+5:07:43.9	42.50	8.70 ± 0.07	GBT	A11	0.0738 ± 0.0015	9428 ± 245	B11;B15
G038.738−0.140	15B-178	19:02:33.4	+5:06:05.0	105.52	9.75 ± 0.10	GBT	A11	...	...	...
G038.840+0.497	13A-030	19:00:28.5	+5:28:58.5	84.39	7.45 ± 0.07	GBT	A11	0.0734 ± 0.0020	9221 ± 317	B11;B15
G038.875+0.308	13A-030	19:01:12.5	+5:25:41.8	42.50	27.05 ± 0.12	GBT	A11	0.0822 ± 0.0008	8384 ± 116	B11;B15
G039.183−1.422	15B-178	19:07:56.9	+4:54:31.2	60.00	4.95 ± 0.16	GBT	A15b	...	...	...
G039.196+0.224	15B-178	19:02:05.8	+5:40:32.2	60.00	2.32 ± 0.10	Arecibo	B12	...	...	...
G039.869+0.645	13A-030	19:01:49.3	+6:27:45.5	68.19	10.80 ± 0.09	GBT	A11	0.0708 ± 0.0013	9373 ± 214	B11;B15
G041.750+0.034	15B-178	19:07:29.9	+7:51:27.3	121.00	2.90 ± 0.10	GBT	A15b	...	...	...
G041.762+1.479	15B-178	19:02:19.9	+8:31:54.0	268.99	2.35 ± 0.09	GBT	A15b	...	...	...
G043.149+0.028	15B-178	19:10:07.7	+9:05:47.0	35.18	3129.19 ± 10.23	140 Foot	Q06	...	...	...
G043.240+0.131	15B-178	19:09:55.7	+9:13:28.1	42.50	5.40 ± 0.17	GBT	A11	...	...	...
G043.432+0.521	13A-030	19:08:54.1	+9:34:22.2	74.33	11.25 ± 0.15	GBT	A11	0.1021 ± 0.0019	8338 ± 198	B11;B15
G043.523−0.648	15B-178	19:13:15.5	+9:06:54.0	88.57	2.20 ± 0.18	GBT	A11	...	...	...
G043.818+0.393	13A-030	19:10:03.7	+9:51:31.6	108.26	14.80 ± 0.09	GBT	A11	0.0781 ± 0.0013	8802 ± 196	B11;B15
G043.818+0.395	15B-178	19:10:03.7	+9:51:31.6	108.26	14.80 ± 0.09	GBT	A11	0.0781 ± 0.0013	8802 ± 196	B11;B15
G043.968+0.993	15B-178	19:08:11.3	+10:16:04.7	50.84	5.55 ± 0.25	GBT	A15b	...	...	...
G044.417+0.536	13A-030	19:10:41.0	+10:27:22.6	84.69	6.55 ± 0.08	GBT	A11	0.0926 ± 0.0026	8492 ± 299	B11;B15
G044.501+0.335	13A-030	19:11:34.3	+10:26:07.5	50.65	24.25 ± 0.12	GBT	A11	0.1017 ± 0.0017	8350 ± 153	B11;B15
G045.197+0.738	13A-030	19:11:24.5	+11:14:28.3	80.49	9.35 ± 0.10	GBT	A11	0.0556 ± 0.0010	10841 ± 245	B11;B15
G045.391−0.725	15B-178	19:17:03.7	+10:43:57.9	191.48	26.50 ± 0.26	GBT	A11	...	...	...
G046.173+0.533	15B-178	19:14:00.4	+12:00:39.7	60.00	2.04 ± 0.04	Arecibo	B12	...	...	...
G048.719+1.147	15B-178	19:16:38.2	+14:32:58.9	82.92	6.30 ± 0.32	GBT	A15b	...	...	...
G049.399−0.490	15B-178	19:23:55.6	+14:22:54.6	51.68	68.15 ± 0.23	GBT	A11	...	...	...
G049.690−0.166	15B-178	19:23:19.0	+14:47:29.5	178.62	76.92 ± 7.69	140 Foot	L96	...	...	...
G050.032+0.605	15B-178	19:21:09.8	+15:27:24.2	139.55	5.50 ± 0.20	GBT	A15b	...	...	...

Table 1 (*continued*)

Table 1 (*continued*)

Field	Project	R.A. J2000 (hh:mm:ss)	Decl. J2000 (dd:mm:ss)	$R_{\text{IR}}$ (arcsec)	$S_9$ GHz, $L$ (mJy beam $^{-1}$ )	Telescope <sup>a</sup>	RRL Author <sup>b</sup>	$S_L/S_C$	$T_e$ (K)	$T_e$ Author <sup>c</sup>
G052.001+1.602	15B-178	19:21:21.4	+17:39:45.1	49.60	2.00 ± 0.07	GBT	A15b	...	...	...
G052.098+1.042	15B-178	19:23:37.1	+17:29:01.8	122.52	38.40 ± 0.17	GBT	A11	...	...	...
G052.160+0.708	15B-178	19:24:58.5	+17:22:49.6	67.26	7.00 ± 0.20	GBT	A11	...	...	...
G052.256+0.702	15B-178	19:25:11.2	+17:27:43.9	120.73	5.30 ± 0.08	Arecibo	B12	...	...	...
G054.093+1.748	15B-178	19:24:58.5	+19:34:32.6	81.06	2.60 ± 0.10	GBT	A15b	...	...	...
G054.490+0.930	15B-178	19:28:49.9	+19:32:08.0	245.76	4.95 ± 0.09	GBT	A11	...	...	...
G054.490+1.579	15B-178	19:26:24.4	+19:50:41.1	87.52	3.50 ± 0.10	GBT	A15b	...	...	...
G055.114+2.422	15B-178	19:24:29.9	+20:47:33.2	146.16	28.75 ± 0.17	GBT	A15b	0.0423 ± 0.0003	13126 ± 144	B11;B15
G059.796+0.241	15B-178	19:42:32.9	+23:50:02.4	159.46	53.38 ± 0.41	GBT	B11	0.0975 ± 0.0008	9068 ± 120	B11;B15
G060.592+1.572	15B-178	19:39:11.2	+25:10:59.4	126.28	13.05 ± 0.13	GBT	A15b	...	...	...
G061.431+2.081	15B-178	19:39:02.7	+26:09:52.0	143.57	3.65 ± 0.17	GBT	A15b	...	...	...
G061.720+0.863	15B-178	19:44:23.6	+25:48:44.2	72.00	9.30 ± 0.10	GBT	A11	...	...	...
G062.577+2.389	15B-178	19:40:21.9	+27:18:45.9	141.52	31.60 ± 0.18	GBT	A15b	...	...	...
G068.144+0.915	15B-178	19:59:09.7	+31:21:32.3	160.08	23.91 ± 0.27	GBT	B11	0.0697 ± 0.0009	10834 ± 207	B11;B15
G070.280+1.583	15B-178	20:01:47.8	+33:31:33.4	53.06	328.08 ± 1.75	GBT	B11	...	...	...
G070.673+1.190	15B-178	20:04:24.0	+33:38:59.2	120.63	2.65 ± 0.13	GBT	A15b	...	...	...
G070.765+1.820	15B-178	20:02:03.9	+34:03:47.8	86.97	12.10 ± 0.14	GBT	A15b	...	...	...
G071.150+0.397	15B-178	20:08:50.5	+33:37:30.8	144.06	33.75 ± 0.10	GBT	A15b	...	...	...
G073.878+1.023	15B-178	20:13:34.7	+36:15:00.4	71.21	7.80 ± 0.10	GBT	A15b	...	...	...
G074.155+1.646	15B-178	20:11:45.0	+36:49:26.5	95.39	3.70 ± 0.11	GBT	A15b	...	...	...
G074.753+0.912	15B-178	20:16:27.5	+36:54:57.7	91.43	6.40 ± 0.12	GBT	A15b	...	...	...
G075.175-0.593	15B-178	20:23:50.1	+36:24:39.5	306.78	8.80 ± 0.14	GBT	A15b	...	...	...
G075.768+0.344	15B-178	20:21:41.2	+37:26:02.9	197.80	273.60 ± 0.56	GBT	B11	0.0790 ± 0.0004	8590 ± 47	B11;B15
G078.174-0.550	15B-178	20:32:30.2	+38:52:15.1	160.63	10.20 ± 0.15	GBT	A15b	...	...	...
G078.886+0.709	15B-178	20:29:24.7	+40:11:18.7	174.84	9.75 ± 0.23	GBT	A15b	...	...	...
G080.191+0.534	15B-178	20:34:13.7	+41:08:14.5	53.88	4.85 ± 0.12	GBT	A15b	...	...	...
G091.113+1.580	15B-178	21:09:36.0	+50:13:22.5	278.16	37.75 ± 0.17	GBT	A15b	...	...	...
G093.518+2.611	15B-178	21:15:22.5	+52:40:39.6	107.51	4.45 ± 0.16	GBT	A15b	...	...	...
G094.263-0.414	15B-178	21:32:32.7	+51:02:19.3	100.14	2.10 ± 0.10	GBT	A15b	...	...	...

Table 1 (*continued*)

Table 1 (*continued*)

Field	Project	R.A. J2000 (hh:mm:ss)	Decl. J2000 (dd:mm:ss)	$R_{\text{IR}}$ (arcsec)	$S_9$ GHz, $L$ (mJy beam $^{-1}$ )	Telescope <sup>a</sup>	RRL Author <sup>b</sup>	$S_L/S_C$	$T_e$ (K)	$T_e$
G096.289+2.593	15B-178	21:28:42.4	+54:37:05.8	193.20	23.60 ± 0.11	GBT	A15b	0.0570 ± 0.0009	11039 ± 314	B11;B15
G096.434+1.324	15B-178	21:35:20.3	+53:47:14.1	91.59	5.05 ± 0.14	GBT	A15b	...	...	...
G097.444+3.083	15B-178	21:32:14.7	+55:45:52.4	95.94	2.00 ± 0.18	GBT	A15b	...	...	...
G097.515+3.173	15B-178	21:32:10.8	+55:52:44.6	122.86	33.60 ± 0.18	GBT	A15b	...	...	...
G101.016+2.590	15B-178	21:54:19.5	+57:43:06.4	101.64	3.40 ± 0.18	GBT	A15b	...	...	...
G104.700+2.784	15B-178	22:16:25.9	+60:03:01.8	102.78	6.25 ± 0.18	GBT	A15b	...	...	...
G109.104−0.347	15B-178	22:59:09.0	+59:28:36.7	95.34	6.00 ± 0.12	GBT	A15b	...	...	...
G111.802+0.526	15B-178	23:16:32.4	+61:19:49.6	96.95	5.10 ± 0.20	GBT	A15b	...	...	...
G118.276+2.490	15B-178	00:07:14.9	+64:57:44.9	239.84	2.35 ± 0.17	GBT	A15b	...	...	...
G118.592+2.828	15B-178	00:09:40.8	+65:20:50.2	161.64	3.30 ± 0.18	GBT	A15b	...	...	...
G124.637+2.535	15B-178	01:07:47.3	+65:21:12.5	165.16	18.30 ± 0.21	GBT	A15b	0.0576 ± 0.0012	10758 ± 288	B11;B15
G125.092+0.778	15B-178	01:10:51.9	+63:34:06.7	136.99	2.85 ± 0.17	GBT	A15b	...	...	...
G135.188+2.701	15B-178	02:42:24.6	+62:54:07.3	142.05	6.05 ± 0.12	GBT	A15b	...	...	...
G136.119+2.118	15B-178	02:47:33.7	+61:58:48.1	127.23	3.30 ± 0.13	GBT	A15b	...	...	...
G136.884+0.911	15B-178	02:48:55.9	+60:33:38.8	805.95	69.23 ± 8.08	140 Foot	L89	0.0995 ± 0.0025	8204 ± 257	B11;B15
G141.084−1.063	15B-178	03:10:16.0	+56:50:04.3	249.15	7.80 ± 0.12	GBT	A15b	...	...	...
G148.474+1.982	15B-178	04:05:41.7	+54:54:55.2	104.17	2.55 ± 0.14	GBT	A15b	...	...	...
G150.859−1.115	15B-178	04:03:50.6	+51:00:57.9	123.28	2.85 ± 0.13	GBT	A15b	...	...	...
G154.646+2.438	15B-178	04:36:48.8	+50:52:42.5	370.38	25.02 ± 0.33	GBT	B11	0.0673 ± 0.0009	9734 ± 175	B11;B15
G189.830+0.417	15B-178	06:08:58.1	+20:38:29.2	199.15	82.62 ± 1.35	140 Foot	Q06	...	...	...
G192.638−0.008	15B-178	06:13:07.5	+17:58:33.5	174.27	52.91 ± 0.44	GBT	B11	0.0971 ± 0.0010	8833 ± 107	B11;B15
G196.448−1.673	15B-178	06:14:37.3	+13:50:02.6	302.50	30.80 ± 0.37	GBT	B11	0.0773 ± 0.0010	9945 ± 164	B11;B15
G201.535+1.597	15B-178	06:36:11.8	+10:51:56.8	790.64	12.79 ± 0.26	GBT	B11	0.0713 ± 0.0015	10063 ± 283	B11;B15
G212.021−1.309	15B-178	06:45:07.1	+0:12:49.8	1075.77	50.00 ± 5.38	140 Foot	L96	...	...	...
G218.737+1.850	15B-178	07:08:39.2	−4:18:55.1	215.23	35.22 ± 0.28	GBT	B11	0.0509 ± 0.0005	14578 ± 195	B11;B15
G224.158+1.213	15B-178	07:16:29.0	−9:24:51.3	558.98	8.35 ± 0.12	GBT	A15b	...	...	...
G227.760−0.127	15B-178	07:18:30.6	−13:13:29.4	324.34	7.54 ± 0.09	GBT	B11	0.0485 ± 0.0007	12495 ± 249	B11;B15
G231.481−4.401	15B-178	07:09:54.3	−18:29:53.7	511.74	21.11 ± 0.49	GBT	B11	0.1011 ± 0.0024	9098 ± 286	B11;B15
G233.753−0.193	15B-178	07:30:04.6	−18:32:03.8	311.06	27.16 ± 0.41	GBT	B11	0.0822 ± 0.0015	9482 ± 209	B11;B15

Table 1 (*continued*)



Table 1 (*continued*)

Field	Project	R.A. J2000 (hh:mm:ss)	Decl. J2000 (dd:mm:ss)	$R_{\text{IR}}$ (arcsec)	$S_9 \text{ GHz}, L$ (mJy beam <sup>-1</sup> )	Telescope <sup>a</sup>	RRL Author <sup>b</sup>	$S_L/S_C$	$T_e$ (K)	$T_e$ Author <sup>c</sup>
G243.244+0.406	15B-178	07:52:42.5	-26:29:00.1	941.61	49.06 ± 0.47	GBT	B11	0.0764 ± 0.0012	10220 ± 110	Q06b;B15
G253.694-0.414	15B-178	08:15:34.9	-35:45:30.3	1540.80	42.31 ± 4.23	140 Foot	L89	...	...	...
G341.207-0.232	15B-178	16:52:20.7	-44:28:06.8	58.11	90.60 ± 0.45	GBT	A15b	...	...	...
G348.691-0.826	15B-178	17:19:06.6	-38:51:37.7	1328.28	3132.27 ± 13.38	140 Foot	Q06	...	...	...
G351.246+0.673	15B-178	17:20:17.7	-35:54:29.2	131.55	2251.35 ± 7.73	140 Foot	Q06	0.0896 ± 0.0006	8560 ± 70	Q06b;B15
G351.311+0.663	15B-178	17:20:31.2	-35:51:37.7	119.03	3356.38 ± 10.69	140 Foot	Q06	...	...	...

<sup>a</sup>Original RRL detection telescope<sup>b</sup>Original RRL detection reference<sup>c</sup>RRL-to-continuum flux ratio measurement and electron temperature derivation reference

**References**—(L89) Lockman (1989); (L96) Lockman et al. (1996); (Q06a) Quireza et al. (2006a); (Q06b) Quireza et al. (2006b); (A11) Anderson et al. (2011); (B11) Balser et al. (2011); (B12) Bania et al. (2012); (A15a) Anderson et al. (2015a); (A15b) Anderson et al. (2015b); (B15) Balser et al. (2015)

contain at least one H II region that meets our selection criteria.

Our final H II region target catalog contains 147 unique nebulae. Table 1 lists information about these H II regions: the *WISE* Catalog name; the VLA project in which it was observed (13A–030 is the pilot survey and 15B–178 is the main survey); the *WISE* infrared position; the *WISE* infrared radius,  $R_{\text{IR}}$ ; the estimated 9 GHz RRL flux density,  $S_{9\text{ GHz}, L}$ ; the telescope and reference for the previous RRL detection; the previously measured RRL-to-continuum brightness ratio,  $S_L/S_C$ , and derived electron temperature,  $T_e$ ; and the reference for the RRL-to-continuum brightness ratio and electron temperature.

### 3. OBSERVATIONS AND DATA REDUCTION

We used the VLA to simultaneously observe radio continuum and RRL emission toward our sample of 147 Galactic H II regions. The data were acquired in the most compact (D) antenna configuration as part of two projects: the pilot survey (13A–030; 5 hours) in Feb and Apr 2013, and the main survey (15B–178; 30 hours) in Oct and Nov 2015. A summary of the observations is in Table 2.

The VLA X-band receiver covers the frequency range  $\sim 8\text{--}12$  GHz. We used the Wideband Interferometric Digital ARchitecture (WIDAR) correlator in the 8-bit sampler mode to simultaneously measure  $\sim 8\text{--}10$  GHz radio continuum emission and 8 hydrogen RRL transitions in both linear polarizations. The continuum data were measured by 16 low spectral resolution spectral windows (hereafter, continuum windows) covering 7.8–8.9 GHz and 9–10 GHz continuously. The RRL spectra were measured by 8 high spectral resolution (31.25 kHz) spectral windows (hereafter, spectral line windows), each with 16 MHz of frequency coverage. There are only 7 H $\alpha$  RRL transitions in this frequency range (H87 $\alpha$  to H93 $\alpha$ ), so we tuned one of the spectral line windows to H109 $\beta$ . The native velocity resolution ranges from  $0.9\text{ km s}^{-1}$  at H87 $\alpha$  to  $1.2\text{ km s}^{-1}$  at H93 $\alpha$ , with a velocity coverage ranging from  $488\text{ km s}^{-1}$  to  $600\text{ km s}^{-1}$  for these transitions, respectively. In one observing session of the pilot survey, the spectral line window for H88 $\alpha$  was mistuned, so we exclude that spectral window from these analyses. Table 3 lists the following properties for each spectral window: the center frequency,  $\nu_{\text{center}}$ ; the bandwidth; the number of channels; the channel width,  $\Delta\nu$ ; the targeted RRL transition; and the RRL rest frequency,  $\nu_{\text{RRL}}$ .

Our targets are clustered into 12 observing sessions based on position, with  $\sim 10$  H II regions per group. Every observing session begins with a  $\sim 15$  minute inte-

gration on a primary calibrator, which is used for the absolute flux, delay, and bandpass calibration, followed by a  $\sim 10$  minute integration on a secondary calibrator located near the H II region science targets, which is used for the complex gain calibration. These calibrators are listed in Table 2. We observe each science target for 10–15 minutes to reach the necessary spectral sensitivity, then we return to the secondary calibrator for  $\sim 5$  more minutes. During each observing session, we repeat this process for each science target.

We use the Wenger Interferometry Software Package (WISP) to calibrate, reduce, and analyze these data (Wenger 2018). WISP is a *Python* wrapper for the Common Astronomy Software Applications package (CASA; McMullin et al. 2007). Although WISP was developed to reduce Australia Telescope Compact Array data for the Southern H II Region Discovery Survey (Wenger et al. 2019), its modular framework can be applied to any radio interferometric dataset. We follow the Wenger et al. (2019) data reduction process, which we briefly describe here.

#### 3.1. Calibration

The WISP calibration pipeline derives calibration solution tables using the calibrator source data, flags radio frequency interference (RFI) and other bad data, and applies the calibration solutions to the science target data. We inspect both the calibration solutions and calibrated data to assess the quality of the calibration solutions and to manually flag bad data that was missed by the WISP automatic flagging routines. The most common issues we flag are (1) antennas with poor calibration solutions, (2) broad frequency RFI that contaminates an entire spectral window, and (3) shadowed antennas. In rare cases, RFI can compromise nearly half of all of our spectral windows.

#### 3.2. Imaging

We use the WISP imaging pipeline to automatically generate and clean images from the calibrated visibility data. We begin by regridding all of the data to a common kinematic local standard of rest (LSR) velocity frame with a channel width  $\Delta\nu_{\text{LSR}} = 1.2\text{ km s}^{-1}$ . Using the *TCLEAN* task in *CASA*, we generate several images and data cubes: (1) a multiscale, multi-frequency synthesis (MS-MFS) continuum image of the combined continuum spectral windows, (2) an MS-MFS image of each continuum and spectral line window, and (3) a multiscale data cube of each spectral line window. Following the strategy of Wenger et al. (2019), we use *CLEAN* masks from each spectral line window MS-MFS image to *CLEAN* the data cube for that spectral window.

**Table 2.** Observation Summary

	13A-030	15B-178
Dates	2013 Feb and Apr	2015 Oct and Nov
Observing Time (hr)	5	30
H II Region Targets	20	128
Primary Calibrators	3C286	3C286, 3C48
Secondary Calibrators	J1733–1304, J1822–0938 J1824+1044, J1922+1530	J0019+7327, J0102+5824 J0244+6228, J0349+4609 J0358+5606, J0625+1440 J0653–0625, J0735–1735 J0804–2749, J1604–4441 J1744–3116, J1820–2528 J1822–0938, J1824+1044 J1922+1530, J1924+3329 J1925+2106, J2007+4029 J2025+3343, J2137+5101 J2137+5101 J2148+6107

Many of our observed H II regions are spatially resolved. We increase our surface brightness sensitivity to resolved emission by *uv*-tapering our visibilities when generating images. This process, however, reduces our point source sensitivity and worsens our angular resolution. Therefore, we generate both non-tapered and *uv*-tapered images/data cubes for each field. The latter are tapered to a synthesized half-power beam width (HPBW) of 15 arcsec, which is about twice the native VLA resolution at X-band.

#### 4. DATA ANALYSIS

The data analysis process for this survey closely follows the [Wenger et al. \(2019\)](#) strategy. Because multiple nebulae may be observed in a single VLA pointing, we first identify unique *WISE* Catalog sources in each 8–10 GHz MS-MFS continuum image. Emission is associated with the *WISE* Catalog nebulae as long as the peak continuum brightness pixel is within a circle centered on the *WISE* Catalog position with a radius equal to the *WISE* Catalog infrared radius. We manually locate these peak continuum brightness pixels for each nebula with detected radio continuum emission.

Unlike [Wenger et al. \(2019\)](#), we wish to derive the total fluxes of extended sources in addition to their peak fluxes. We use a watershed segmentation algorithm to identify the pixels associated with the manually identified continuum peaks in our images and data cubes. This algorithm considers an image as a three dimensional topological surface, where the image brightness

corresponds to the “depth” of the surface. The algorithm identifies the basins that would be filled by flooding the surface from a given starting point (see [Bertrand 2005](#)). In cases where multiple starting points will flood the same basin (i.e., in confused fields), the algorithm divides the basin into separate regions for each flooding source. Hereafter, we will use “watershed region” to describe the regions identified by the watershed segmentation algorithm.

We set the manually identified continuum brightness peak locations as the flooding sources for the watershed segmentation algorithm. Using the MS-MFS images clipped at 5 times the spatial rms noise, we run the algorithm to identify the watershed regions associated with each continuum source. Figure 2 shows an example region identified by this algorithm. We use the clipped continuum images to avoid low-brightness noise spikes in the watershed regions, but, as a result, we also miss faint emission associated with the nebulae. Therefore, our total continuum fluxes are systematically under-estimated, especially for faint sources.

For each continuum source we measure the brightness and total flux at the location of the peak brightness and within the watershed region, respectively. The uncertainty of the peak continuum brightness is derived as the spatial rms of the *CLEAN* residual image divided by the VLA primary beam response at the peak continuum brightness position. To compute the uncertainty on the total continuum flux, we must consider that the spatial noise in an interferometric image is correlated on

**Table 3.** Correlator Setup

Window	$\nu_{\text{center}}$ ( MHz )	Bandwidth ( MHz )	Channels	$\Delta\nu$ ( kHz )	RRL	$\nu_{\text{RRL}}$ ( MHz )
0	7949.3	128	128	1000	...	...
1	8049.1	128	128	1000	...	...
2	8049.1	16	512	31.25	H93 $\alpha$	8045.605
3	8205.3	128	128	1000	...	...
4	8333.3	128	128	1000	...	...
5	8313.0	16	512	31.25	H92 $\alpha$	8309.385
6	8461.3	128	128	1000	...	...
7	8589.3	128	128	1000	...	...
8	8588.5	16	512	31.25	H91 $\alpha$	8584.823
9	8717.3	128	128	1000	...	...
10	8845.3	128	128	1000	...	...
11	8876.4	16	512	31.25	H90 $\alpha$	8872.571
12	9082.3	128	128	1000	...	...
13	9210.3	128	128	1000	...	...
14	9177.3	16	512	1000	H89 $\alpha$	9173.323
15	9338.3	128	128	1000	...	...
16	9466.3	128	128	1000	...	...
17	9491.9	16	512	31.25	H88 $\alpha$	9487.824
18	9594.3	128	128	1000	...	...
19	9722.3	128	128	1000	...	...
20	9850.3	128	128	1000	...	...
21 <sup>a</sup>	9821.1	16	512	31.25	H87 $\alpha$	9816.867
22	9887.3	16	512	31.25	H109 $\beta$	9883.083
23	9978.3	128	128	1000	...	...

<sup>a</sup>Spectral window 21 was mistuned for one observing session in 13A-030.

the scale of the synthesized beam. The variance in the sum of the brightnesses of  $N$  pixels within a region is

$$\sigma_T^2 = \sum_i^N \sum_j^N \rho_{ij} \sigma_i \sigma_j, \quad (1)$$

where  $\sigma_i$  is the spatial rms of the *CLEAN* residual image divided by the VLA primary beam response at the position of the  $i$ th pixel,  $\rho_{ij}$  is the correlation coefficient between the  $i$ th and  $j$ th pixels, and the sums are taken over all  $N$  pixels within the region. We use the two-dimensional Gaussian synthesized beam to define the correlation coefficient:

$$\rho_{ij} = \exp [-A\Delta x^2 - 2B\Delta x\Delta y - C\Delta y^2], \quad (2)$$

where

$$\begin{aligned} A &= \frac{\cos^2 \phi}{2\theta_{\text{maj}}^2} + \frac{\sin^2 \phi}{2\theta_{\text{min}}^2}, \\ B &= -\frac{\sin(2\phi)}{4\theta_{\text{maj}}^2} + \frac{\sin(2\phi)}{4\theta_{\text{min}}^2}, \\ C &= \frac{\sin^2 \phi}{2\theta_{\text{maj}}^2} + \frac{\cos^2 \phi}{2\theta_{\text{min}}^2}, \end{aligned}$$

$\Delta x$  and  $\Delta y$  are the angular separations between the  $i$ th and  $j$ th pixels in the east-west and north-south directions, respectively, and  $\theta_{\text{maj}}$ ,  $\theta_{\text{min}}$ , and  $\phi$  are the synthesized beam major axis, minor axis, and north-through-east position angle, respectively. In the simple case where  $\sigma_i \simeq \sigma_j \simeq \sigma$  (i.e., the noise is constant across the source), equation 1 reduces to

$$\sigma_T^2 \simeq \sigma^2 \sum_i^N \sum_j^N \rho_{ij} \simeq \sigma^2 N_{\text{beam}}, \quad (3)$$

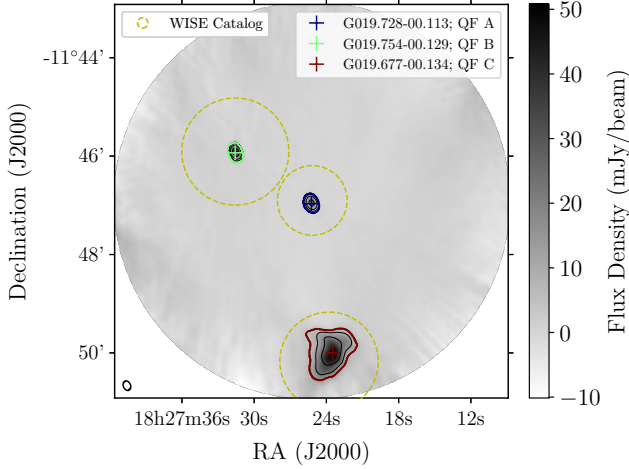


**Figure 2.** Watershed regions in a  $\sim 2$  GHz combined MS-MFS continuum image. This field is centered on G019.728–0.113 and contains three *WISE* Catalog H II regions. The black contours are at 5, 10, 20, and 50 times the spatial rms noise ( $\sim 0.6$  mJy beam $^{-1}$  at the field center), and the yellow dashed circles represent the position and infrared radii of the *WISE* Catalog nebulae. The manually identified peak continuum brightness pixels are indicated by the colored plus symbols, and the watershed regions by the colored contours. These regions were created using the MS-MFS image clipped at 5 times the spatial rms noise to avoid including noise spikes in the watershed regions. These nebulae are examples of continuum quality factors (QF) A, B, and C, as indicated in the legend (see Section 5.1).

where  $N_{\text{beam}}$  is the number of synthesized beams contained within the region. Many of our sources are extended or located near the edge of the primary beam, such that the primary beam response and noise varies across the source. Therefore, we use equation 1 to derive the total continuum flux uncertainties.

We maximize our sensitivity to the faint RRL emission by averaging each observed  $\text{Hn}\alpha$  RRL transition and both polarizations. This average spectrum is denoted by  $\langle \text{Hn}\alpha \rangle$ . For non-tapered images, we extract spectra from each line spectral window data cube at the location of the peak continuum brightness. The  $\langle \text{Hn}\alpha \rangle$  spectrum is computed as the weighted average of the individual RRL transitions. The weights are given by  $w_i = S_{C,i}/\text{rms}_i^2$  where  $S_{C,i}$  is the continuum brightness and  $\text{rms}_i$  is the spectral rms noise of the  $i$ th spectral window, both measured in the line-free region of the spectrum. For  $uv$ -tapered images, we spatially smooth the data cubes to a common beam size, then extract the spectra and compute the  $\langle \text{Hn}\alpha \rangle$  spectrum in the same fashion.

The total RRL emission within the watershed regions is extracted from the data cubes differently than for the

peak position. For each pixel in the region, we measure the median continuum brightness in the line-free region of the spectrum,  $S_{C,i}$ . Then, we sum each pixel's spectrum,  $S_{L,i}$ , weighted by the median continuum brightness in that pixel. The final extracted spectrum for this spectral window is normalized by the ratio of the median non-weighted sum and median weighted sum:

$$S_L(\nu) = \left( \sum_i S_{L,i}(\nu) S_{C,i} \right) \times \frac{\text{median}(\sum_i S_{L,i})}{\text{median}(\sum_i S_{L,i}(\nu) S_{C,i})}. \quad (4)$$

This complicated procedure correctly weights the final spectrum by the continuum level in each pixels' spectra, thereby maximizing the signal-to-noise ratio of the RRL and ensuring that the final spectrum has the correct flux density. The watershed region  $\langle \text{Hn}\alpha \rangle$  spectrum is then computed using the same weighted average of the individual RRL transitions as for the peak positions.

Finally, we measure the  $\langle \text{Hn}\alpha \rangle$  RRL properties. We first identify the line-free regions of the spectrum to estimate the spectral rms noise and to fit and remove a third-order polynomial baseline. Then, we fit a Gaussian to the baseline-subtracted spectrum and measure the RRL brightness, the FWHM line width, and the LSR velocity.

## 5. RESULTS

### 5.1. VLA Data Products

Our goal is to derive an accurate nebular electron temperature for as many of the observed Galactic H II regions as possible. Given that some of these nebulae will be extremely faint, spatially resolved, and/or in confusing fields, no single data analysis method will work for each nebula. For each source, we therefore employ a suite of different analysis methods and then we pick the combination of non-tapered or  $uv$ -tapered images and peak position  $\langle \text{Hn}\alpha \rangle$  or watershed region  $\langle \text{Hn}\alpha \rangle$  spectra that maximizes our RRL sensitivity and minimizes our electron temperature uncertainty.

We detect radio continuum emission in 88 (59%) of the 148 observed fields. This low detection rate is a result of the relatively poor surface brightness sensitivity of the VLA. Many of the fields, however, contain multiple *WISE* Catalog H II regions and/or H II region candidates. We detect radio continuum emission toward 114 known or candidate H II regions. Table 4 lists the measured radio continuum properties of these nebulae: the *WISE* Catalog source name; the MS-MFS synthesized frequency of the combined continuum spectral windows,  $\nu_C$ ; the peak continuum flux density,  $S_C^P$ ; a quality factor for the peak flux density, QF $_C^P$ ; a column indicating

whether the peak flux density was measured using the non-tapered (N) or *uv*-tapered (Y) image; the total flux density within the watershed region,  $S_C^T$ ; a quality factor for the total flux density,  $QF_C^T$ ; and a column indicating whether the peak flux density was measured using the non-tapered or *uv*-tapered image. The MS-MFS synthesized frequency varies slightly for each field due to differences in data flagging. We select either non-tapered or

*uv*-tapered based on which gives the smallest fractional uncertainty in the final electron temperature derivation (if the source also has a RRL detection), or which has the smallest fractional uncertainty in the continuum flux density. For resolved nebulae, the *uv*-tapered images typically have a smaller fractional electron temperature or continuum flux density uncertainty.

**Table 4.** Continuum Data Products

Name	$\nu_C$	$S_C^P$	$QF_C^P$	Taper <sup>P a</sup>	$S_C^T$	$QF_C^T$	Taper <sup>P a</sup>
	(MHz)	(mJy beam <sup>-1</sup> )			(mJy)		
G005.885−00.393	8962.2	4516.01 ± 13.31	A	N	5254.49 ± 35.45	A	N
G010.596−00.381	8962.2	395.02 ± 6.66	A	Y	907.08 ± 18.66	A	Y
G013.880+00.285	8962.2	1696.64 ± 3.26	A	Y	3368.06 ± 10.64	B	N
G017.336−00.146	8962.1	10.91 ± 0.29	B	Y	51.38 ± 0.84	B	N
G017.928−00.677	8962.1	14.48 ± 0.37	B	Y	57.76 ± 1.07	B	N
G018.584+00.344	8962.1	22.53 ± 0.82	A	Y	46.79 ± 1.20	A	N
G018.630+00.309	8962.1	13.01 ± 4.37	C	Y	0.04 ± 0.18	C	N
G019.677−00.134	8962.1	163.19 ± 3.36	C	Y	469.63 ± 7.10	C	N
G019.728−00.113	8962.1	24.23 ± 0.40	A	N	27.24 ± 0.68	A	N
G019.754−00.129	8962.1	46.45 ± 0.59	B	N	45.73 ± 1.01	B	N
G020.227+00.110	8962.1	8.61 ± 0.13	B	Y	41.72 ± 0.36	B	N
G020.363−00.014	8962.1	50.30 ± 0.09	A	N	58.28 ± 0.23	A	N
G020.387−00.018	8962.1	8.58 ± 0.16	B	Y	26.85 ± 0.46	B	Y
G021.386−00.255	8962.1	122.94 ± 0.12	A	N	136.88 ± 0.45	A	N
G021.596−00.161	8962.2	5.70 ± 0.16	A	N	6.77 ± 0.26	A	N
G021.603−00.169	8962.2	19.32 ± 0.15	A	N	27.62 ± 0.34	A	N
G023.661−00.252	8962.2	30.11 ± 0.46	B	Y	152.51 ± 1.16	B	N
G024.153+00.163	8962.2	10.94 ± 1.62	C	N	4.60 ± 1.14	C	N
G024.166+00.250	8962.2	16.56 ± 0.79	B	N	17.44 ± 1.11	B	N
G024.195+00.242	8962.2	9.77 ± 0.57	B	N	47.78 ± 1.69	B	N
G024.713−00.125	8962.2	32.51 ± 2.11	C	N	138.58 ± 5.73	C	N
G025.397+00.033	8962.2	229.49 ± 0.56	B	N	494.08 ± 2.57	B	N
G025.398+00.562	8962.1	203.74 ± 0.36	A	Y	221.10 ± 1.21	A	N
G025.401+00.021	8962.2	54.54 ± 0.60	B	N	150.97 ± 1.87	B	N
G027.562+00.084	8898.2	47.71 ± 0.23	A	N	111.74 ± 0.71	A	N
G028.320+01.243	8962.1	21.17 ± 0.04	A	N	30.22 ± 0.11	A	N
G028.438+00.014	8962.2	4.01 ± 0.35	A	N	11.73 ± 0.74	A	N
G028.451+00.001	8962.2	36.09 ± 0.30	A	N	84.81 ± 1.30	A	N
G028.581+00.145	8962.2	25.87 ± 0.18	A	N	39.68 ± 0.41	A	N
G029.770+00.219	8962.2	35.40 ± 0.16	A	N	72.53 ± 0.45	A	N
G029.956−00.020	8962.2	1770.38 ± 4.48	A	N	4299.65 ± 22.54	A	N

**Table 4** *continued*

**Table 4** (*continued*)

Name	$\nu_C$	$S_C^P$	QF $_C^P$	Taper $^{Pa}$	$S_C^T$	QF $_C^T$	Taper $^{Pa}$
	(MHz)	(mJy beam $^{-1}$ )			(mJy)		
G030.211+00.428	8962.2	15.61 $\pm$ 0.04	A	N	25.81 $\pm$ 0.12	A	N
G031.269+00.064	8962.2	2.70 $\pm$ 0.34	A	N	1.00 $\pm$ 0.22	A	N
G031.279+00.061	8962.2	125.29 $\pm$ 0.35	A	N	306.72 $\pm$ 1.15	A	N
G031.580+00.074	8962.2	13.41 $\pm$ 0.21	B	N	15.17 $\pm$ 0.38	B	N
G032.030+00.048	8962.2	17.10 $\pm$ 0.19	A	N	25.83 $\pm$ 0.40	A	N
G032.057+00.077	8962.2	13.36 $\pm$ 1.03	C	Y	94.17 $\pm$ 2.13	C	N
G032.272-00.226	8962.2	147.87 $\pm$ 0.18	A	N	330.84 $\pm$ 0.75	A	N
G032.928+00.606	8898.2	173.86 $\pm$ 0.27	A	N	336.64 $\pm$ 1.38	A	N
G033.643-00.229	8962.2	6.37 $\pm$ 0.09	A	Y	10.85 $\pm$ 0.15	A	N
G034.041+00.052	8962.2	25.97 $\pm$ 0.48	A	Y	83.27 $\pm$ 1.08	A	N
G034.089+00.438	8962.2	34.42 $\pm$ 2.87	C	N	83.68 $\pm$ 7.38	C	Y
G034.133+00.471	8962.2	378.58 $\pm$ 1.10	A	Y	517.00 $\pm$ 2.35	A	N
G034.686+00.068	8962.2	55.42 $\pm$ 0.60	A	Y	107.24 $\pm$ 0.95	A	N
G035.126-00.755	8962.2	123.85 $\pm$ 0.43	A	Y	241.91 $\pm$ 0.71	A	N
G035.948-00.149	8962.2	12.05 $\pm$ 0.03	A	N	26.66 $\pm$ 0.08	A	N
G036.870+00.462	8962.2	3.03 $\pm$ 0.31	C	N	9.77 $\pm$ 0.67	C	N
G036.877+00.498	8962.2	1.22 $\pm$ 0.17	C	N	1.90 $\pm$ 0.22	C	N
G036.918+00.482	8962.2	6.21 $\pm$ 0.08	A	N	7.56 $\pm$ 0.15	A	N
G038.550+00.163	8962.2	54.11 $\pm$ 0.25	A	N	122.86 $\pm$ 0.77	A	N
G038.643-00.227	8962.3	18.70 $\pm$ 0.05	A	N	24.79 $\pm$ 0.18	A	N
G038.652+00.087	8962.2	19.77 $\pm$ 0.24	A	N	49.91 $\pm$ 0.96	A	N
G038.840+00.495	8962.2	4.49 $\pm$ 0.09	B	N	84.27 $\pm$ 0.66	B	N
G038.875+00.308	8962.2	279.04 $\pm$ 0.43	A	N	320.84 $\pm$ 1.04	A	N
G039.183-01.422	8962.3	20.75 $\pm$ 0.15	A	Y	57.82 $\pm$ 0.30	A	N
G039.196+00.224	8962.3	62.54 $\pm$ 0.06	A	N	67.11 $\pm$ 0.19	A	N
G039.213+00.202	8962.3	5.13 $\pm$ 0.09	B	N	5.85 $\pm$ 0.16	B	N
G039.864+00.645	8962.3	67.52 $\pm$ 0.51	A	Y	103.48 $\pm$ 0.79	A	N
G043.146+00.013	8962.3	1434.45 $\pm$ 126.49	B	Y	1427.47 $\pm$ 158.00	B	Y
G043.165-00.031	8962.3	2330.17 $\pm$ 78.58	C	N	3341.55 $\pm$ 144.37	C	N
G043.168+00.019	8962.3	332.86 $\pm$ 17.06	B	N	600.24 $\pm$ 31.78	B	N
G043.170-00.004	8962.3	4331.44 $\pm$ 149.88	B	Y	11158.53 $\pm$ 398.42	B	Y
G043.432+00.516	8962.3	11.08 $\pm$ 0.35	B	Y	82.31 $\pm$ 0.83	B	N
G043.523-00.648	8962.3	5.84 $\pm$ 0.04	A	Y	13.22 $\pm$ 0.09	A	N
G043.818+00.395	8962.3	21.54 $\pm$ 0.97	B	Y	94.69 $\pm$ 1.89	B	N
G043.968+00.993	8962.2	47.26 $\pm$ 0.07	A	N	49.81 $\pm$ 0.20	A	N
G043.999+00.978	8962.2	22.23 $\pm$ 0.22	C	N	25.05 $\pm$ 0.42	C	N
G044.501+00.332	8962.3	21.92 $\pm$ 1.24	B	Y	135.68 $\pm$ 2.23	B	N
G044.503+00.349	8962.3	7.16 $\pm$ 0.36	A	N	8.58 $\pm$ 0.54	A	N
G045.197+00.740	8962.3	7.76 $\pm$ 0.18	B	N	140.36 $\pm$ 1.42	B	N
G048.719+01.147	8962.4	37.12 $\pm$ 0.10	A	Y	69.80 $\pm$ 0.29	A	N

**Table 4** *continued*

**Table 4** (*continued*)

Name	$\nu_C$	$S_C^P$	QF $_C^P$	Taper $^Pa$	$S_C^T$	QF $_C^T$	Taper $^Pa$
	(MHz)	(mJy beam $^{-1}$ )			(mJy)		
G049.399−00.490	8962.4	166.98 ± 7.12	A	Y	232.47 ± 8.75	A	N
G052.098+01.042	8962.3	287.77 ± 0.50	A	Y	432.07 ± 0.89	A	N
G052.232+00.735	8962.4	68.65 ± 4.32	C	Y	162.56 ± 5.42	C	N
G054.093+01.748	8962.3	18.84 ± 0.03	A	Y	34.60 ± 0.08	A	Y
G054.490+01.579	8962.3	24.30 ± 0.06	A	Y	44.24 ± 0.13	A	N
G054.543+01.560	8962.3	3.73 ± 0.26	C	Y	3.52 ± 0.21	C	N
G055.114+02.422	8962.3	138.55 ± 1.25	A	Y	618.76 ± 2.79	B	N
G060.592+01.572	8962.3	55.66 ± 0.22	A	Y	166.35 ± 0.51	A	N
G061.720+00.863	8962.7	90.28 ± 0.16	A	N	97.51 ± 0.38	A	N
G062.577+02.389	8962.7	51.31 ± 0.28	B	N	359.10 ± 1.71	B	N
G068.144+00.915	8962.7	42.25 ± 1.61	B	Y	302.02 ± 4.24	B	N
G070.280+01.583	8962.6	542.61 ± 15.70	A	Y	1930.78 ± 37.24	A	N
G070.293+01.599	8962.6	3550.27 ± 9.03	A	N	5690.67 ± 39.20	A	N
G070.304+01.595	8962.6	245.05 ± 9.37	A	N	1829.40 ± 41.28	A	N
G070.329+01.589	8962.6	1067.39 ± 23.78	B	N	2670.68 ± 65.51	B	N
G070.673+01.190	8962.6	260.40 ± 0.72	A	Y	407.26 ± 1.43	A	N
G070.765+01.820	8962.6	28.79 ± 0.52	A	Y	173.85 ± 1.36	B	N
G071.150+00.397	8962.7	208.43 ± 0.25	A	N	392.62 ± 0.92	A	N
G073.878+01.023	8962.6	75.77 ± 0.09	A	N	120.61 ± 0.26	A	N
G074.155+01.646	8962.6	10.25 ± 0.04	A	N	37.97 ± 0.21	A	N
G074.753+00.912	8962.6	55.70 ± 0.07	A	N	74.69 ± 0.20	A	N
G075.768+00.344	8962.6	1059.58 ± 10.20	A	Y	4104.53 ± 20.67	B	N
G078.114−00.550	8962.6	14.17 ± 3.03	C	Y	0.04 ± 0.10	C	N
G078.174−00.550	8962.6	4.21 ± 0.19	B	N	23.01 ± 0.72	B	N
G078.886+00.709	8962.6	83.02 ± 0.08	A	N	110.14 ± 0.25	A	N
G080.191+00.534	8962.6	5.14 ± 0.09	A	N	40.72 ± 0.45	A	N
G094.263−00.414	8963.1	4.40 ± 0.04	B	Y	18.73 ± 0.14	B	N
G096.289+02.593	8963.1	27.93 ± 0.32	B	N	442.24 ± 2.68	B	N
G096.434+01.324	8963.1	23.34 ± 0.10	A	N	36.94 ± 0.25	A	N
G097.515+03.173	8963.1	131.05 ± 0.65	A	Y	508.47 ± 1.73	B	N
G097.528+03.184	8963.1	41.23 ± 0.29	A	N	49.32 ± 0.55	A	N
G101.016+02.590	8963.0	17.71 ± 0.06	A	Y	21.24 ± 0.14	A	N
G104.700+02.784	8963.0	9.00 ± 0.17	A	Y	39.99 ± 0.36	A	N
G109.104−00.347	8963.0	7.10 ± 0.07	A	N	19.36 ± 0.20	A	N
G124.637+02.535	8963.4	252.56 ± 0.20	A	N	293.16 ± 0.62	A	N
G125.092+00.778	8963.5	6.70 ± 0.02	A	Y	20.65 ± 0.07	B	N
G135.188+02.701	8963.4	19.82 ± 0.09	A	Y	65.47 ± 0.18	B	N
G141.084−01.063	8963.8	12.17 ± 0.19	A	Y	62.35 ± 0.37	B	N
G150.859−01.115	8963.8	11.73 ± 0.10	A	Y	18.02 ± 0.15	A	N
G196.448−01.673	8964.0	10.93 ± 0.47	B	N	350.13 ± 4.13	B	N

**Table 4** *continued*



Table 4 (continued)

Name	$\nu_C$	$S_C^P$	QF $_C^P$	Taper $^Pa$	$S_C^T$	QF $_C^T$	Taper $^Pa$
	(MHz)	(mJy beam $^{-1}$ )			(mJy)		
G218.737+01.850	8964.1	202.41 $\pm$ 0.69	A	Y	554.43 $\pm$ 1.73	A	N
G351.246+00.673	8962.2	7191.06 $\pm$ 24.43	A	Y	11722.85 $\pm$ 66.92	A	N
G351.311+00.663	8962.2	2809.89 $\pm$ 29.27	A	Y	5561.39 $\pm$ 64.30	A	N

<sup>a</sup>”N” if non-tapered image measurement; ”Y” if  $uv$ -tapered image measurement

The quality factor (QF) is a qualitative assessment of the accuracy of the continuum flux measurement. QF A detections are isolated, unresolved, and near the center of the primary beam, QF B detections are slightly resolved, in crowded fields, and/or are located off-center from the primary beam, QF C detections are well-resolved, in very crowded fields, and/or are located near the edge of the primary beam. Any continuum sources that are confused/blended are assigned QF D. These nebulae are excluded from the tables and all subsequent analysis since we are unable to measure their continuum fluxes accurately. The three nebulae in Figure 2 are examples of each continuum QF: G019.728–00.113 is a QF A detection, G019.754–00.129 is a QF B detection because it is off-center, and G019.677–00.134 is a QF C detection because it is resolved and near the edge of the primary beam.

We detect  $\langle \text{Hn}\alpha \rangle$  RRL emission toward 82 (72%) of our 114 continuum sources. All RRL detections are toward previously-known H II regions. Figure 3 shows representative  $\langle \text{Hn}\alpha \rangle$  RRL detections with different signal-to-noise ratios. Our typical spectral rms noise is  $\sim 1$  mJy beam $^{-1}$ , about three times greater than what we estimated using the VLA sensitivity calculator. This decrease in sensitivity is likely due to RFI that compromised entire spectral line spectral windows. We may be able to further increase our spectral line sensitivity by self-calibration.

Table 5 lists the measured  $\langle \text{Hn}\alpha \rangle$  RRL properties of our detections: the *WISE* Catalog source name; the weighted average frequency of the  $\langle \text{Hn}\alpha \rangle$  spectrum,  $\nu_L$ , where the weights are the same as those used to average the individual RRL transitions (see Section 4); the amplitude of the Gaussian fit to the spectrum extracted from the location of peak continuum brightness,  $S_L^P$ ; the spectral rms at this position,  $\text{rms}_L^P$ ; the center LSR velocity of the fitted Gaussian,  $v_{\text{LSR}}^P$ ; the FWHM line width of the fitted Gaussian,  $\Delta V^P$ ; a column indicating whether the spectrum was extracted from the non-tapered (N) or  $uv$ -tapered (Y) image; the amplitude of the Gaussian fit to the spectrum summed within the watershed region,  $S_L^T$ ; the spectral rms in this region,  $\text{rms}_L^T$ ;

the center LSR velocity of the fitted Gaussian,  $v_{\text{LSR}}^T$ ; the FWHM line width of the fitted Gaussian,  $\Delta V^T$ ; and a column indicating whether the spectrum was extracted from the non-tapered or  $uv$ -tapered image. As before, we use either the non-tapered or  $uv$ -tapered image depending on which gives the smallest fractional uncertainty in the derived electron temperature. Unlike B15, we do not assign quality factors to our RRL detections. Our spectral baselines are always flat and well-modeled by a third-order polynomial, therefore no qualitative assessment is necessary. Two nebulae, G005.885–00.393 and G070.293+01.599, are excluded from Table 5 because they have blended, non-Gaussian line profiles.

## 5.2. Electron Temperatures

Thermal bremsstrahlung (free-free) emission is the primary source of H II region radio continuum emission. Its intensity depends on the plasma electron temperature, the plasma electron density, and the stellar ionizing photon rate. The free-free opacity of an H II region in LTE is well-approximated by

$$\tau_C \simeq 3.28 \times 10^{-7} \left( \frac{T_e}{10^4 \text{ K}} \right)^{-1.35} \left( \frac{\nu}{\text{GHz}} \right)^{-2.1} \times \left( \frac{\text{EM}}{\text{pc cm}^{-6}} \right) \quad (5)$$

where  $T_e$  is the plasma electron temperature, EM is the emission measure, and  $\nu$  is the frequency (Mezger & Henderson 1967). The emission measure is the integral of the squared electron number density,  $n_e^2$ , along the line of sight path through the nebula:  $\text{EM} = \int n_e^2 dl$ . An optically thin H II region has a continuum brightness temperature  $T_C \simeq \tau_C T_e$ . Without an independent determination of the emission measure, we are unable to use the continuum emission alone to derive the nebular electron temperature.

The RRL intensity and line width reveal the physical characteristics of an H II region. The line center opacity of an H II region in LTE is approximated by

$$\tau_L \simeq 1.92 \times 10^3 \left( \frac{T_e}{\text{K}} \right)^{-2.5} \left( \frac{\text{EM}}{\text{pc cm}^{-6}} \right) \left( \frac{\Delta \nu}{\text{kHz}} \right)^{-1} \quad (6)$$

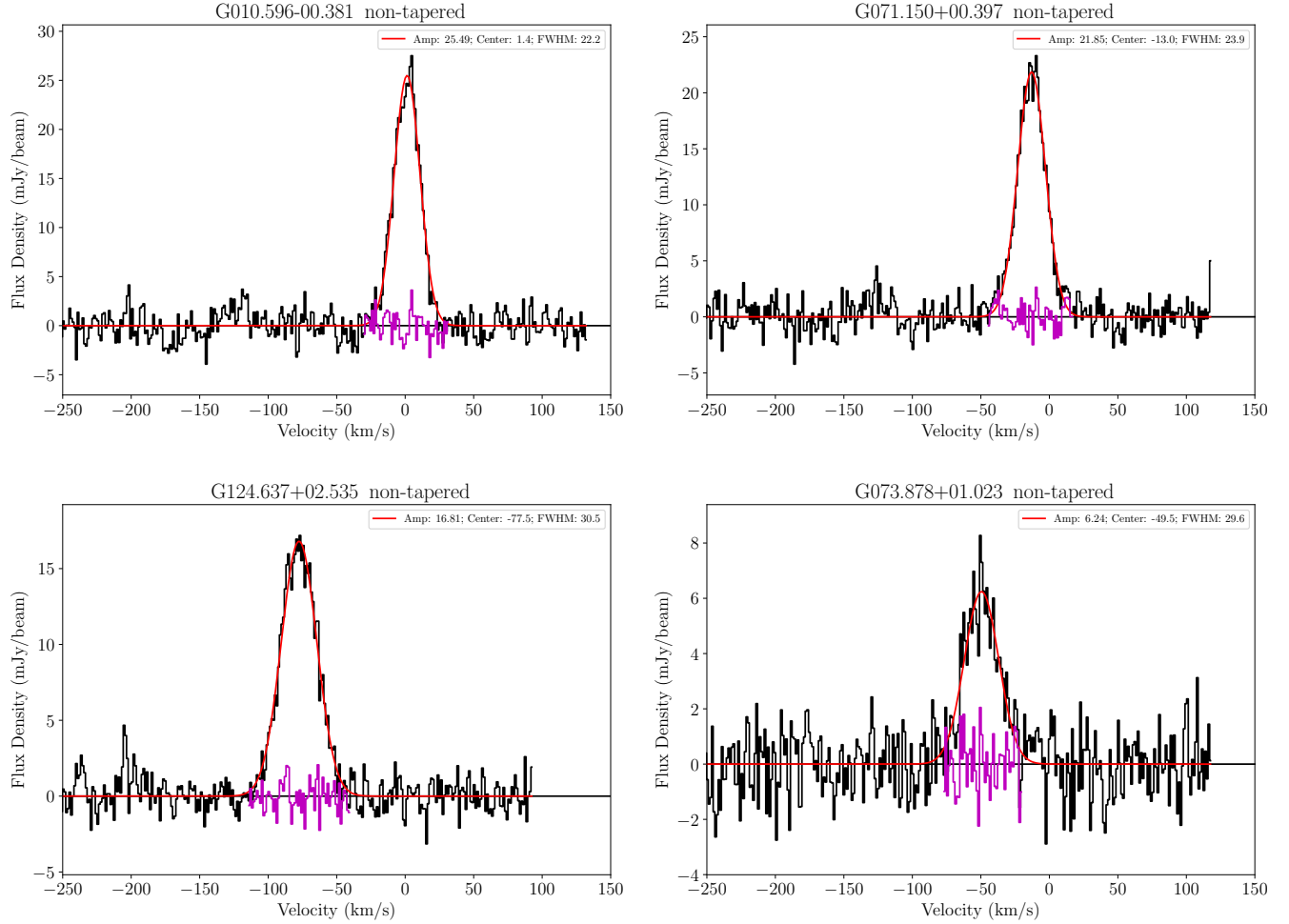


**Figure 3.** Representative  $\langle \text{Hn}\alpha \rangle$  stacked spectra. The spectra for G010.596–00.381 (top-left), G071.150+00.397 (top-right), G124.637+02.535 (bottom-left), and G073.878+01.023 (bottom-right) span the range of typical RRL detection signal-to-noise ratios. The black histogram is the data, the red curve is the Gaussian fit with parameters listed in the legend, and the magenta curve is the fit residuals. These spectra were extracted from the non-tapered data cubes at the location of the peak continuum brightness.

where  $\Delta\nu$  is the full-width half-maximum (FWHM) line width in frequency units (Kardashev 1959; Mezger & Hoglund 1967). Similar to the continuum, we need an independent measurement of the emission measure in order to use the RRL properties to derive the electron temperature.

The typical hydrogen RRL line width for Galactic H II regions is  $\sim 25 \text{ km s}^{-1}$  (Wenger et al. 2019). There are four physical effects that contribute to the RRL FWHM line width: (1) intrinsic broadening, due to the uncertainty principle; (2) collisional broadening, due to the collisions of the emitting atoms; (3) thermal Doppler broadening, due to the Maxwellian velocity distribution of emitting atoms in the plasma; and (4) non-thermal Doppler broadening. Of these, thermal and non-thermal Doppler broadening are the most significant contributors to the width of RRLs. The non-

thermal (i.e., turbulent) components can only be constrained with additional information. RRL line width measurements for nebular plasma atoms other than hydrogen are needed, since atoms with different masses have different Maxwellian velocity distributions. Alternatively, the thermal contribution to the RRL line width can be determined by deriving the plasma temperature.

We derive the nebular electron temperature from the RRL-to-continuum brightness ratio. For an H II region in LTE that is optically thin to both continuum and RRL emission, the ratio of the radio continuum brightness temperature to the RRL peak brightness temperature is equal to the ratio of the continuum opacity to the line center opacity. This ratio is independent of the emission measure. A complete derivation of the electron temperature equation is in Appendix A. For RRLs near  $\text{H}90\alpha$ , assuming the continuum and RRL emission

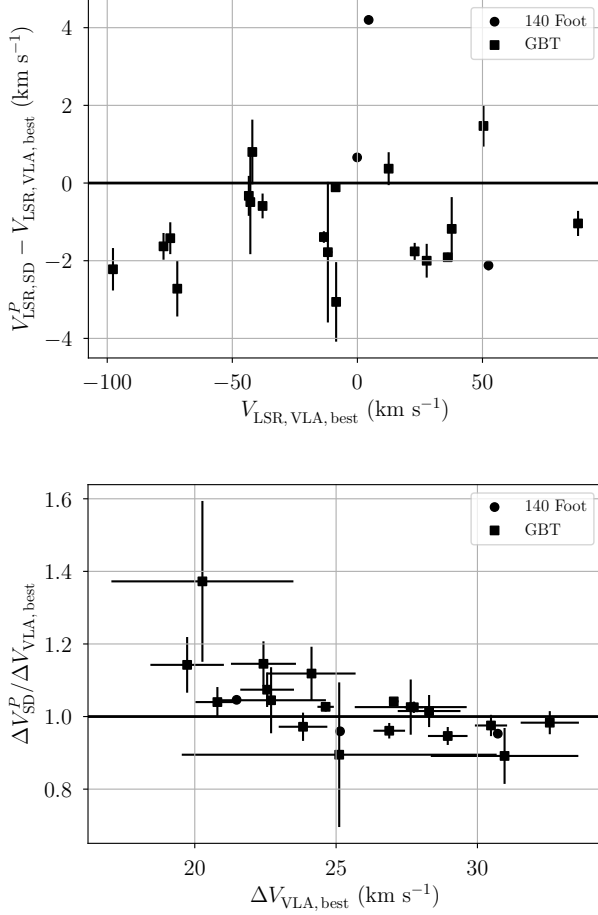


**Figure 4.** Difference between single dish and VLA RRL LSR velocities (top) and ratio of single dish to VLA RRL FWHM line widths (bottom) as a function of the VLA values for 22 nebulae also observed by the GBT (squares) or 140 Foot (circles). We use the “best” VLA images and spectral extraction technique, which minimizes the fractional uncertainty of the derived electron temperature. The weighted mean LSR velocity difference is  $-0.09 \pm 0.34 \text{ km s}^{-1}$  and the weighted mean FWHM line width ratio is  $0.99 \pm 0.02$ , where the weights are the reciprocal variances in the differences or ratios derived from the fitted Gaussian parameter uncertainties.

originate in the same volume of gas, we find

$$\frac{T_e}{\text{K}} \simeq \left[ 7.100 \times 10^3 \left( \frac{\nu_L}{\text{GHz}} \right)^{1.1} \left( \frac{S_C}{S_L} \right) \times \left( \frac{\Delta V}{\text{km s}^{-1}} \right)^{-1} (1 + y^+)^{-1} \right]^{0.87} \quad (7)$$

where  $\nu_L$  is the RRL frequency,  $S_C$  is the continuum flux density,  $S_L$  is the RRL center flux density,  $\Delta V$  is the RRL FWHM line width in velocity units, and  $y^+$  is

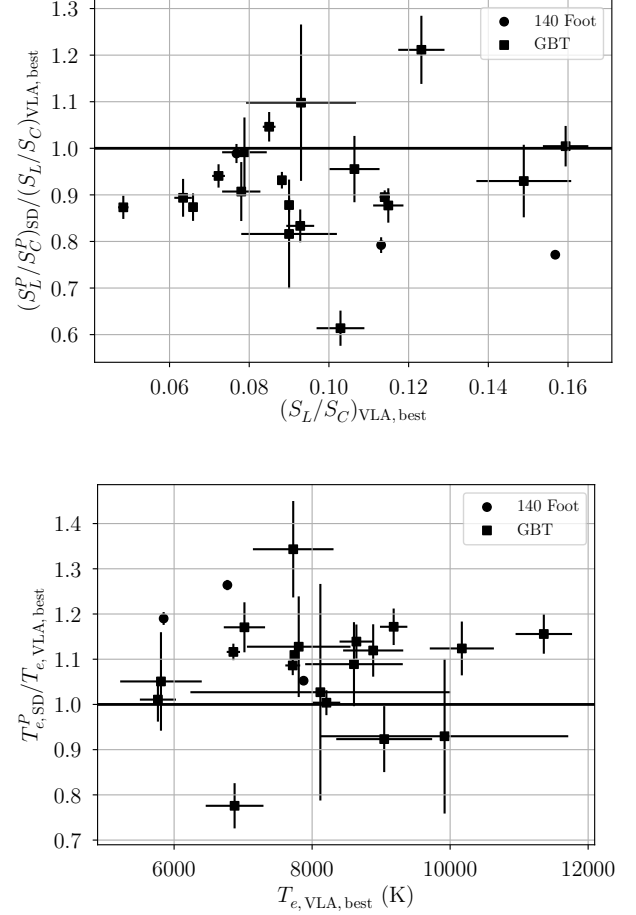


**Figure 5.** Ratio of single dish to VLA RRL-to-continuum brightness ratios (top) and electron temperatures (bottom) as a function of the VLA values for the same nebulae as in Figure 4. The weighted mean ratio of the single dish and VLA RRL-to-continuum brightness ratios is  $0.86 \pm 0.03$  and the weighted mean electron temperature ratio is  $1.12 \pm 0.03$ , where the weights are the reciprocal variances in the ratios derived from the fitted Gaussian parameter uncertainties.

the ratio of the number density of singly ionized helium to hydrogen.

We use Equation 7 to derive the electron temperatures of the 72 nebulae in our sample with a VLA  $\langle \text{Hn}\alpha \rangle$  RRL detection and a continuum quality factor A, B, or C. We only detect helium RRLs in a few, bright sources, so we assume  $y^+ = 0.08$  for all VLA detections, following Balser et al. (2011) and B15. Equation 7 is only weakly dependent on  $y^+$ . A 10% increase from  $y^+ = 0.08$  results in a mere 0.6% increase in  $T_e$ . We do not consider uncertainties in  $y^+$  in the subsequent analyses because the electron temperature uncertainties are typically much greater than 0.6%. Furthermore, we assume non-LTE effects and collisional broadening are negligible at these

frequencies (see Balser et al. 1999). The RRL flux density, RRL FWHM line width, and continuum flux density are measured in the  $\langle \text{Hn}\alpha \rangle$  stacked spectrum, and the RRL frequency is the weighted average frequency of the individual RRL transitions. Again, the frequency weights are the same as those used to average the individual RRL transitions (see Section 4). In Appendix A, we show that this strategy can produce accurate electron temperatures.

Table 6 lists the *WISE* Catalog source name, the telescope used for the observation, the measured RRL-to-continuum flux ratios, the RRL FWHM line widths, and the derived electron temperatures for the B15 single dish and our VLA H II region samples. This table only lists the highest quality electron temperature derivations; we remove all QF D sources from the B15 and VLA samples. The electron temperature uncertainties are computed by propagating the RRL-to-continuum flux ratio and FWHM line width uncertainties through Equation 7. For VLA sources, the “Type” column indicates whether the position of peak continuum brightness (P) or watershed region (T) is used to measure the RRL-to-continuum flux ratio. The “Taper” column identifies which data cube is used (N for non-tapered and Y for *uv*-tapered). We select the combination of “Type” and “Taper” that minimizes the fractional uncertainty in the derived electron temperature. In cases where the same source is detected in multiple surveys, we only list the VLA values, if available. If the source is not observed or detected in the VLA survey, we list the GBT values. If the source is not in the VLA survey nor the GBT survey, we list the 140 Foot values. Table 6 also includes information about the H II region distances, which is discussed in Section 5.4.

In total, there are now 189 Galactic H II regions with accurate electron temperature determinations. This is an increase of 99 nebulae (110%) over the B15 sample. A fraction of these nebulae have inaccurate distances, however, and can not be used to investigate Galactic metallicity structure.

### 5.3. Comparison with Single Dish

Our sample combines measurements from three telescopes: the 140 Foot, the GBT, and the VLA. Each of these telescopes may be affected by systematics that lead to discrepancies between the derived electron temperatures because each is sampling a different volume of gas within and surrounding the H II regions. For example, diffuse foreground and background emission may affect the single dish observations, but such extended emission is filtered out by the VLA. In principle, there may be differences between the different single dish measurements

as well. Balser et al. (2011) find no significant difference between the derived electron temperatures for 16 nebulae observed by both the 140 Foot and the GBT. Here we compare the single dish and VLA observations of 22 nebulae in common between the B15 single dish catalog and our VLA catalog.

We first compare the fitted LSR velocity of these nebulae. The top panel of Figure 4 shows the difference between the single dish RRL LSR velocity and that measured by the VLA for the 22 nebulae observed by the VLA and either the GBT or the 140 Foot. Here and in all subsequent analyses, we use the “best” combination of non-tapered or *uv*-tapered data cubes and continuum peak brightness location or watershed region for spectral extraction. “Best” means the combination of tapering and spectral extraction technique that minimizes the fractional uncertainty in the derived electron temperature. The single dish and VLA LSR velocities are in good agreement, with a weighted mean difference of  $-0.09 \pm 0.34 \text{ km s}^{-1}$  (the error here is the uncertainty of the mean), a median difference of  $-1.28 \text{ km s}^{-1}$ , and a standard deviation of  $1.59 \text{ km s}^{-1}$ . Throughout these analyses, we use the reciprocal variances of the fitted Gaussian parameters as the weights in the averages.

Next we compare the single dish and VLA RRL FWHMs. The bottom panel of Figure 4 shows the ratio of the single dish RRL line width to that measured by the VLA for the overlapping nebulae. The weighted mean of the line width ratios is  $0.99 \pm 0.02$ , the median ratio is 1.03, and the standard deviation is 0.10. For the narrowest RRLs, the VLA line widths are  $\sim 5$ -10% smaller than those measured by the single dish telescopes. This trend is likely due to the fact that the VLA is probing a denser and less turbulent component of the nebulae.

Finally we compare the measured RRL-to-continuum brightness ratios and derived electron temperatures between the single dish and VLA surveys. Figure 5 shows the ratio of the single dish and VLA measured RRL-to-continuum flux ratios (top) and electron temperatures (bottom). The single dish RRL-to-continuum brightness ratios are systematically  $\sim 10\%$  less than the VLA brightness ratios. The weighted mean of these ratios is  $0.86 \pm 0.03$  with a median of 0.90 and a standard deviation of 0.12. Consequently, the single dish electron temperatures are  $\sim 10\%$  greater than the VLA electron temperatures. The weighted mean of the electron temperature ratios is  $1.12 \pm 0.03$  with a median of 1.10 and a standard deviation of 0.12.

The cause of the systematic difference between the single dish and VLA RRL-to-continuum brightness ratios and electron temperatures is unclear. The differ-

Table 5. RRL Data Products

Name	$\nu_L$ (MHz)	$S_L^P$ (mJy beam $^{-1}$ )	rms $^P$ (mJy beam $^{-1}$ )	$v_{LSR}^P$ (km s $^{-1}$ )	$\Delta V^P$ (km s $^{-1}$ )	Taper $^P a$	$S_L^T$ (mJy)	rms $^T$ (mJy)	$v_{LSR}^T$ (km s $^{-1}$ )	$\Delta V^T$ (km s $^{-1}$ )	Taper $^T a$
G009.612+00.205	8862.2	5.53 $\pm$ 0.39	1.19	2.5 $\pm$ 0.8	22.2 $\pm$ 1.9	N	2.71 $\pm$ 0.08	0.24	3.2 $\pm$ 0.3	22.1 $\pm$ 0.8	N
G009.613+00.200	8786.3	81.07 $\pm$ 0.67	1.97	4.0 $\pm$ 0.1	20.4 $\pm$ 0.2	Y	133.99 $\pm$ 1.12	3.29	3.8 $\pm$ 0.1	20.5 $\pm$ 0.2	N
G010.596-00.381	8816.4	59.07 $\pm$ 0.60	1.87	1.1 $\pm$ 0.1	23.3 $\pm$ 0.3	Y	107.40 $\pm$ 0.98	3.06	1.1 $\pm$ 0.1	23.1 $\pm$ 0.2	Y
G010.621-00.380	8789.6	80.22 $\pm$ 0.52	1.67	-0.5 $\pm$ 0.1	24.8 $\pm$ 0.2	N	3.61 $\pm$ 0.03	0.10	-0.7 $\pm$ 0.1	24.9 $\pm$ 0.2	N
G010.623-00.385	8737.2	175.69 $\pm$ 1.08	4.12	1.1 $\pm$ 0.1	35.0 $\pm$ 0.2	Y	182.71 $\pm$ 0.99	4.03	0.9 $\pm$ 0.1	39.9 $\pm$ 0.2	N
G012.805-00.196	8779.1	1097.15 $\pm$ 3.02	11.78	36.3 $\pm$ 0.0	36.4 $\pm$ 0.1	Y	2079.31 $\pm$ 5.80	22.02	36.7 $\pm$ 0.0	34.5 $\pm$ 0.1	Y
G012.813-00.200	8767.2	199.79 $\pm$ 1.44	4.85	30.2 $\pm$ 0.1	27.2 $\pm$ 0.2	N	74.74 $\pm$ 0.65	2.20	30.4 $\pm$ 0.1	27.7 $\pm$ 0.3	N
G013.880+00.285	8806.2	267.42 $\pm$ 0.64	1.90	52.4 $\pm$ 0.0	21.5 $\pm$ 0.1	Y	530.66 $\pm$ 1.35	4.06	52.0 $\pm$ 0.0	21.6 $\pm$ 0.1	Y
G017.928-00.677	8738.1	...	...	...	...	...	10.52 $\pm$ 1.04	3.06	38.4 $\pm$ 1.0	21.1 $\pm$ 2.5	Y
G018.584+00.344	8806.1	3.57 $\pm$ 0.35	1.09	14.4 $\pm$ 1.2	24.1 $\pm$ 3.0	Y	7.58 $\pm$ 0.60	1.80	14.3 $\pm$ 0.9	22.2 $\pm$ 2.1	Y
G019.677-00.134	8595.3	18.57 $\pm$ 1.27	4.14	54.7 $\pm$ 0.9	27.0 $\pm$ 2.4	Y	50.04 $\pm$ 2.52	8.33	55.6 $\pm$ 0.7	26.6 $\pm$ 1.6	N
G019.728-00.113	8883.1	4.09 $\pm$ 0.34	1.08	53.6 $\pm$ 1.0	25.3 $\pm$ 2.5	Y	3.29 $\pm$ 0.25	0.81	52.9 $\pm$ 0.9	25.0 $\pm$ 2.3	N
G020.363-00.014	8832.6	7.16 $\pm$ 0.32	0.98	55.1 $\pm$ 0.5	22.3 $\pm$ 1.2	N	7.90 $\pm$ 0.34	1.05	55.5 $\pm$ 0.5	22.5 $\pm$ 1.1	N
G021.603-00.169	8886.8	2.67 $\pm$ 0.30	0.87	-4.9 $\pm$ 1.3	23.0 $\pm$ 3.8	Y	...	...	...	...	...
G023.661-00.252	8885.9	5.28 $\pm$ 0.34	1.03	66.5 $\pm$ 0.7	22.2 $\pm$ 1.7	Y	26.59 $\pm$ 1.08	3.17	67.2 $\pm$ 0.4	20.5 $\pm$ 1.0	Y
G024.195+00.242	8819.2	3.38 $\pm$ 0.50	1.53	33.0 $\pm$ 1.8	24.3 $\pm$ 4.8	Y	3.52 $\pm$ 0.55	1.72	31.9 $\pm$ 1.9	25.1 $\pm$ 5.0	N
G025.397+00.033	8826.1	20.71 $\pm$ 0.28	0.94	-14.0 $\pm$ 0.2	28.0 $\pm$ 0.4	N	35.95 $\pm$ 0.56	1.88	-14.0 $\pm$ 0.2	27.3 $\pm$ 0.5	N
G025.398+00.562	8775.9	15.47 $\pm$ 0.27	0.98	11.7 $\pm$ 0.3	32.0 $\pm$ 0.6	Y	15.69 $\pm$ 0.29	1.07	11.5 $\pm$ 0.3	31.3 $\pm$ 0.7	N
G025.401+00.021	8867.2	10.30 $\pm$ 0.55	1.73	-10.7 $\pm$ 0.6	24.3 $\pm$ 1.5	Y	12.38 $\pm$ 0.51	1.54	-10.2 $\pm$ 0.4	22.4 $\pm$ 1.1	N
G026.597-00.024	8892.9	7.09 $\pm$ 0.21	0.80	17.3 $\pm$ 0.5	34.6 $\pm$ 1.2	N	15.57 $\pm$ 0.51	1.78	18.6 $\pm$ 0.5	30.0 $\pm$ 1.1	Y
G027.562+00.084	8542.6	15.65 $\pm$ 0.53	1.55	88.2 $\pm$ 0.3	20.4 $\pm$ 0.8	Y	18.08 $\pm$ 0.59	1.74	88.2 $\pm$ 0.3	20.8 $\pm$ 0.8	N
G028.320+01.243	8893.2	1.77 $\pm$ 0.26	0.65	-40.5 $\pm$ 1.1	15.0 $\pm$ 2.7	N	1.76 $\pm$ 0.30	0.86	-39.6 $\pm$ 4.5	34.1 $\pm$ 21.9	N
G028.451+00.001	8840.4	5.07 $\pm$ 0.32	1.10	-7.2 $\pm$ 0.9	28.7 $\pm$ 2.2	Y	5.96 $\pm$ 0.36	1.20	-6.9 $\pm$ 0.8	27.2 $\pm$ 1.9	N
G028.581+00.145	8860.3	2.84 $\pm$ 0.24	0.76	-13.1 $\pm$ 1.0	24.4 $\pm$ 2.5	N	3.58 $\pm$ 0.28	0.94	-13.0 $\pm$ 1.0	26.9 $\pm$ 2.6	N
G029.770+00.219	8778.8	5.85 $\pm$ 0.38	1.15	-30.9 $\pm$ 0.7	21.6 $\pm$ 1.7	Y	7.10 $\pm$ 0.47	1.39	-30.9 $\pm$ 0.7	21.4 $\pm$ 1.6	N
G030.211+00.428	8715.8	2.83 $\pm$ 0.37	0.97	-10.8 $\pm$ 1.1	16.6 $\pm$ 2.6	Y	3.00 $\pm$ 0.38	1.02	-11.5 $\pm$ 1.1	17.6 $\pm$ 2.6	N

Table 5 continued

Table 5 (continued)

Name	$\nu_L$ (MHz)	$S_L^P$ (mJy beam $^{-1}$ )	rms $^P$ (mJy beam $^{-1}$ )	$v_{LSR}^P$ (km s $^{-1}$ )	$\Delta V^P$ (km s $^{-1}$ )	Taper $^P a$	$S_L^T$ (mJy)	rms $^T$ (mJy)	$v_{LSR}^T$ (km s $^{-1}$ )	$\Delta V^T$ (km s $^{-1}$ )	Taper $^T a$
G031.580+00.074	8828.1	3.51 $\pm$ 0.46	1.04	100.4 $\pm$ 0.8	12.0 $\pm$ 1.8	N	3.27 $\pm$ 0.39	0.93	100.8 $\pm$ 0.8	13.5 $\pm$ 1.9	N
G032.030+00.048	8848.2	5.13 $\pm$ 0.39	0.99	89.8 $\pm$ 0.6	15.3 $\pm$ 1.3	Y	4.81 $\pm$ 0.31	0.80	90.3 $\pm$ 0.5	16.1 $\pm$ 1.2	N
G032.272-00.226	8819.0	21.61 $\pm$ 0.40	1.32	22.9 $\pm$ 0.2	26.5 $\pm$ 0.6	Y	27.01 $\pm$ 0.49	1.63	22.9 $\pm$ 0.2	26.9 $\pm$ 0.6	N
G032.928+00.606	8590.7	13.70 $\pm$ 0.29	1.00	-37.9 $\pm$ 0.3	28.9 $\pm$ 0.7	N	20.89 $\pm$ 0.49	1.63	-38.2 $\pm$ 0.3	26.9 $\pm$ 0.7	N
G034.041+00.052	8776.4	4.10 $\pm$ 0.40	1.26	36.9 $\pm$ 1.1	23.6 $\pm$ 2.7	Y	12.60 $\pm$ 0.91	2.80	37.7 $\pm$ 0.8	22.7 $\pm$ 1.9	Y
G034.133+00.471	8801.3	42.46 $\pm$ 0.44	1.41	36.1 $\pm$ 0.1	24.6 $\pm$ 0.3	Y	56.32 $\pm$ 0.58	1.86	36.1 $\pm$ 0.1	24.6 $\pm$ 0.3	N
G034.686+00.068	8724.2	7.06 $\pm$ 0.37	1.15	50.5 $\pm$ 0.6	23.8 $\pm$ 1.4	Y	14.29 $\pm$ 0.63	1.94	50.4 $\pm$ 0.5	22.4 $\pm$ 1.1	Y
G035.126-00.755	8814.3	17.99 $\pm$ 0.40	1.17	35.0 $\pm$ 0.2	20.0 $\pm$ 0.5	Y	34.45 $\pm$ 0.71	2.05	35.3 $\pm$ 0.2	19.9 $\pm$ 0.5	N
G035.948-00.149	8872.5	1.87 $\pm$ 0.24	0.74	51.4 $\pm$ 1.4	22.6 $\pm$ 3.6	N	3.15 $\pm$ 0.41	1.19	49.3 $\pm$ 1.4	21.0 $\pm$ 3.6	N
G038.550+00.163	8758.9	11.79 $\pm$ 0.37	1.18	27.6 $\pm$ 0.4	23.7 $\pm$ 0.9	Y	14.88 $\pm$ 0.46	1.46	27.7 $\pm$ 0.4	23.8 $\pm$ 0.9	N
G038.643-00.227	8762.5	2.70 $\pm$ 0.41	1.12	69.4 $\pm$ 1.4	18.5 $\pm$ 3.5	Y	3.81 $\pm$ 0.64	1.61	68.4 $\pm$ 1.3	15.6 $\pm$ 3.3	Y
G038.840+00.495	8764.1	...	...	...	...	...	7.57 $\pm$ 0.98	2.80	-42.8 $\pm$ 1.3	20.3 $\pm$ 3.2	Y
G038.875+00.308	8808.9	25.36 $\pm$ 0.26	0.89	-13.4 $\pm$ 0.1	27.8 $\pm$ 0.3	N	27.91 $\pm$ 0.31	1.07	-13.8 $\pm$ 0.2	28.3 $\pm$ 0.4	N
G039.196+00.224	8787.5	4.51 $\pm$ 0.24	0.84	-21.7 $\pm$ 0.8	28.7 $\pm$ 1.9	N	4.88 $\pm$ 0.27	0.95	-21.1 $\pm$ 0.8	29.2 $\pm$ 2.0	N
G039.864+00.645	8738.8	5.21 $\pm$ 0.34	1.14	-41.3 $\pm$ 0.9	27.3 $\pm$ 2.1	Y	8.57 $\pm$ 0.51	1.72	-42.0 $\pm$ 0.8	27.6 $\pm$ 2.0	N
G043.146+00.013	8708.1	134.45 $\pm$ 0.75	2.67	8.7 $\pm$ 0.1	30.2 $\pm$ 0.2	Y	101.01 $\pm$ 0.52	1.86	8.5 $\pm$ 0.1	31.1 $\pm$ 0.2	Y
G043.151+00.011	8695.6	62.31 $\pm$ 0.51	1.84	5.8 $\pm$ 0.1	31.8 $\pm$ 0.3	N	48.52 $\pm$ 0.35	1.27	6.0 $\pm$ 0.1	31.9 $\pm$ 0.3	N
G043.162+00.005	8768.7	42.28 $\pm$ 0.66	2.22	6.5 $\pm$ 0.2	27.0 $\pm$ 0.5	N	15.82 $\pm$ 0.21	0.70	6.2 $\pm$ 0.2	27.1 $\pm$ 0.4	N
G043.165-00.031	8665.8	154.87 $\pm$ 2.24	8.99	6.8 $\pm$ 0.3	38.8 $\pm$ 0.7	N	128.59 $\pm$ 1.59	6.41	7.5 $\pm$ 0.2	39.0 $\pm$ 0.6	N
G043.168+00.019	8762.5	46.09 $\pm$ 0.53	1.69	9.9 $\pm$ 0.1	24.1 $\pm$ 0.3	N	20.67 $\pm$ 0.22	0.70	9.8 $\pm$ 0.1	24.1 $\pm$ 0.3	N
G043.170-00.004	8670.2	223.40 $\pm$ 0.87	3.38	7.8 $\pm$ 0.1	36.0 $\pm$ 0.2	Y	851.52 $\pm$ 2.80	10.04	4.5 $\pm$ 0.0	30.7 $\pm$ 0.1	Y
G043.175+00.025	8739.0	40.65 $\pm$ 0.58	2.02	14.9 $\pm$ 0.2	28.7 $\pm$ 0.5	N	22.55 $\pm$ 0.27	0.95	14.9 $\pm$ 0.2	29.6 $\pm$ 0.4	N
G043.432+00.516	8896.0	...	...	...	...	...	6.81 $\pm$ 0.97	2.92	-11.8 $\pm$ 1.8	25.1 $\pm$ 5.6	Y
G043.818+00.395	8881.8	...	...	...	...	...	8.70 $\pm$ 0.60	2.11	-8.5 $\pm$ 1.0	31.0 $\pm$ 2.6	Y
G043.968+00.993	8789.7	3.87 $\pm$ 0.24	0.87	-25.5 $\pm$ 1.0	31.9 $\pm$ 2.5	N	3.92 $\pm$ 0.26	0.94	-25.4 $\pm$ 1.0	31.2 $\pm$ 2.6	N
G044.501+00.332	8806.0	2.80 $\pm$ 0.29	0.85	-41.6 $\pm$ 1.1	22.0 $\pm$ 2.8	Y	6.46 $\pm$ 0.37	1.05	-43.4 $\pm$ 0.5	19.7 $\pm$ 1.3	Y
G048.719+01.147	8828.4	3.70 $\pm$ 0.32	1.05	-25.6 $\pm$ 1.1	26.5 $\pm$ 2.8	Y	6.51 $\pm$ 0.55	1.79	-25.9 $\pm$ 1.1	26.6 $\pm$ 2.8	N
G049.399-00.490	8880.6	21.50 $\pm$ 0.43	1.34	62.7 $\pm$ 0.2	22.7 $\pm$ 0.5	Y	24.46 $\pm$ 0.40	1.28	61.5 $\pm$ 0.2	24.1 $\pm$ 0.5	Y
G052.098+01.042	8835.7	24.43 $\pm$ 0.33	1.15	37.5 $\pm$ 0.2	29.3 $\pm$ 0.5	Y	36.72 $\pm$ 0.47	1.63	37.3 $\pm$ 0.2	28.7 $\pm$ 0.4	N

Table 5 continued

Table 5 (continued)

Name	$\nu_L$ (MHz)	$S_L^P$ (mJy beam $^{-1}$ )	rms $^P$ (mJy beam $^{-1}$ )	$v_{LSR}^P$ (km s $^{-1}$ )	$\Delta V^P$ (km s $^{-1}$ )	Taper $^P a$	$S_L^T$ (mJy)	rms $^T$ (mJy)	$v_{LSR}^T$ (km s $^{-1}$ )	$\Delta V^T$ (km s $^{-1}$ )	Taper $^T a$
G052.232+00.735	8756.0	5.54 $\pm$ 0.90	2.72	-1.1 $\pm$ 2.2	26.2 $\pm$ 6.9	Y	19.84 $\pm$ 1.48	4.37	-2.3 $\pm$ 0.8	20.8 $\pm$ 1.8	Y
G055.114+02.422	8859.8	6.60 $\pm$ 0.30	1.08	-73.6 $\pm$ 0.7	32.8 $\pm$ 1.8	Y	29.62 $\pm$ 0.78	2.87	-74.8 $\pm$ 0.4	32.6 $\pm$ 1.0	Y
G060.592+01.572	8864.6	3.93 $\pm$ 0.32	1.05	-50.2 $\pm$ 1.1	27.2 $\pm$ 2.7	Y	11.25 $\pm$ 0.76	2.50	-48.5 $\pm$ 0.9	26.8 $\pm$ 2.2	Y
G061.720+00.863	8808.8	7.00 $\pm$ 0.67	2.11	-69.6 $\pm$ 1.2	25.9 $\pm$ 3.3	N	7.39 $\pm$ 0.78	2.42	-68.4 $\pm$ 1.3	24.5 $\pm$ 3.3	N
G062.577+02.389	8747.3	8.53 $\pm$ 0.98	2.95	-71.2 $\pm$ 1.3	22.3 $\pm$ 3.2	Y	24.80 $\pm$ 2.49	7.44	-72.0 $\pm$ 1.1	22.0 $\pm$ 2.7	Y
G070.280+01.583	8782.7	49.01 $\pm$ 0.86	2.68	-23.6 $\pm$ 0.2	23.4 $\pm$ 0.5	Y	186.56 $\pm$ 1.83	5.95	-25.1 $\pm$ 0.1	25.3 $\pm$ 0.3	Y
G070.304+01.595	8763.0	72.95 $\pm$ 1.10	3.53	-18.2 $\pm$ 0.2	24.5 $\pm$ 0.4	Y	51.50 $\pm$ 0.84	2.63	-17.6 $\pm$ 0.2	23.4 $\pm$ 0.4	N
G070.329+01.589	8694.4	157.24 $\pm$ 2.52	8.96	-18.4 $\pm$ 0.2	30.4 $\pm$ 0.6	Y	123.82 $\pm$ 1.89	6.77	-17.8 $\pm$ 0.2	30.6 $\pm$ 0.5	N
G070.765+01.820	8843.3	...	...	...	...	...	13.56 $\pm$ 1.53	4.85	-78.1 $\pm$ 1.4	24.9 $\pm$ 3.4	N
G071.150+00.397	8783.3	34.14 $\pm$ 0.49	1.56	-12.2 $\pm$ 0.2	24.2 $\pm$ 0.4	Y	38.36 $\pm$ 0.62	1.99	-12.2 $\pm$ 0.2	24.6 $\pm$ 0.5	Y
G073.878+01.023	8815.2	6.24 $\pm$ 0.32	1.12	-49.5 $\pm$ 0.7	29.6 $\pm$ 1.8	N	8.50 $\pm$ 0.41	1.47	-50.3 $\pm$ 0.7	30.8 $\pm$ 1.8	N
G074.155+01.646	8798.0	4.15 $\pm$ 0.46	1.18	-32.2 $\pm$ 0.9	15.9 $\pm$ 2.0	Y	5.86 $\pm$ 0.74	1.88	-31.6 $\pm$ 1.0	15.7 $\pm$ 2.3	Y
G074.753+00.912	8840.0	5.45 $\pm$ 0.33	1.04	-48.9 $\pm$ 0.7	23.7 $\pm$ 1.7	N	6.42 $\pm$ 0.37	1.25	-49.6 $\pm$ 0.8	27.9 $\pm$ 1.9	N
G075.768+00.344	8789.4	100.01 $\pm$ 0.64	2.09	-8.6 $\pm$ 0.1	25.5 $\pm$ 0.2	Y	364.25 $\pm$ 1.98	6.65	-8.7 $\pm$ 0.1	27.0 $\pm$ 0.2	Y
G078.886+00.709	8821.1	12.24 $\pm$ 0.37	1.04	-1.9 $\pm$ 0.3	19.1 $\pm$ 0.7	N	15.90 $\pm$ 0.46	1.31	-1.9 $\pm$ 0.3	19.5 $\pm$ 0.7	N
G096.289+02.593	8873.2	4.36 $\pm$ 0.29	0.97	-87.5 $\pm$ 0.9	26.8 $\pm$ 2.1	Y	27.37 $\pm$ 0.93	3.18	-97.7 $\pm$ 0.5	28.3 $\pm$ 1.1	Y
G096.434+01.324	8856.1	3.89 $\pm$ 0.28	0.85	-77.8 $\pm$ 0.8	21.8 $\pm$ 1.9	Y	4.08 $\pm$ 0.29	0.88	-77.9 $\pm$ 0.8	21.8 $\pm$ 1.8	N
G097.515+03.173	8865.1	9.56 $\pm$ 0.29	1.00	-76.8 $\pm$ 0.4	28.0 $\pm$ 1.0	Y	35.06 $\pm$ 0.79	2.72	-74.4 $\pm$ 0.3	28.2 $\pm$ 0.7	Y
G097.528+03.184	8901.3	4.34 $\pm$ 0.26	0.79	-71.6 $\pm$ 0.7	23.1 $\pm$ 1.6	N	4.55 $\pm$ 0.25	0.79	-72.0 $\pm$ 0.7	24.1 $\pm$ 1.6	N
G101.016+02.590	8896.8	2.57 $\pm$ 0.36	0.92	-70.2 $\pm$ 1.1	16.3 $\pm$ 2.7	Y	2.85 $\pm$ 0.38	1.00	-70.2 $\pm$ 1.1	16.8 $\pm$ 2.7	N
G109.104-00.347	8852.5	2.98 $\pm$ 0.29	0.90	-44.1 $\pm$ 1.1	22.7 $\pm$ 2.6	Y	3.60 $\pm$ 0.34	1.09	-44.4 $\pm$ 1.2	25.7 $\pm$ 2.9	N
G124.637+02.535	8817.1	16.81 $\pm$ 0.27	0.96	-77.5 $\pm$ 0.2	30.5 $\pm$ 0.6	N	18.35 $\pm$ 0.33	1.18	-77.6 $\pm$ 0.3	30.7 $\pm$ 0.6	N
G135.188+02.701	8974.4	2.61 $\pm$ 0.37	1.06	-73.2 $\pm$ 1.4	19.9 $\pm$ 3.3	Y	6.42 $\pm$ 0.88	2.59	-72.2 $\pm$ 2.8	31.9 $\pm$ 12.6	Y
G141.084-01.063	8853.2	...	...	...	...	...	8.50 $\pm$ 1.15	3.15	-25.2 $\pm$ 1.3	18.8 $\pm$ 3.2	Y
G196.448-01.673	8872.6	4.71 $\pm$ 0.37	1.08	10.9 $\pm$ 0.8	20.8 $\pm$ 1.9	Y	27.00 $\pm$ 0.98	3.00	12.5 $\pm$ 0.4	22.6 $\pm$ 0.9	Y
G351.246+00.673	8789.9	851.65 $\pm$ 2.69	8.64	-0.4 $\pm$ 0.0	24.7 $\pm$ 0.1	Y	1474.38 $\pm$ 3.93	12.75	-0.1 $\pm$ 0.0	25.1 $\pm$ 0.1	Y
G351.311+00.663	8839.3	356.60 $\pm$ 1.81	5.76	-6.9 $\pm$ 0.1	24.2 $\pm$ 0.1	Y	774.71 $\pm$ 2.46	7.79	-6.2 $\pm$ 0.0	24.1 $\pm$ 0.1	Y

 $a^a$  N $^a$  if non-tapered image measurement, "Y" if  $w$ -tapered image measurement

**Table 6.** H II Region Distances and Properties

Name	Telescope	$S_L/S_C$	$\Delta V$ (km s <sup>-1</sup> )	$T_e$ (K)	Type <sup>a</sup>	Taper <sup>b</sup>	$d$ (kpc)	$R$ (kpc)	Distance <sup>c</sup> Method	Distance Reference
G000.666-00.036	140 Foot	0.0569 ± 0.0033	40.5 ± 0.4	8170 ± 180	...	...	7.59 <sup>+0.84</sup> <sub>-0.65</sub>	0.21 <sup>+0.91</sup> <sub>-0.11</sub>	P	R09c
G001.125-00.106	140 Foot	0.1070 ± 0.0018	24.5 ± 0.2	7130 ± 70	...	...	...	...	K	...
G003.266-00.061	140 Foot	0.0978 ± 0.0100	25.3 ± 0.4	7440 ± 280	...	...	...	...	K	...
G005.900-00.431	140 Foot	0.0691 ± 0.0006	22.5 ± 0.2	11130 ± 170	...	...	2.99 <sup>+0.17</sup> <sub>-0.20</sub>	5.38 <sup>+0.19</sup> <sub>-0.16</sub>	P	S14
G005.987-01.191	140 Foot	0.0840 ± 0.0008	26.5 ± 0.2	8180 ± 70	...	...	...	...	K	...
G008.137+00.232	140 Foot	0.1019 ± 0.0007	25.4 ± 0.1	7090 ± 60	...	...	...	...	K	...
G010.160-00.350	140 Foot	0.0911 ± 0.0005	31.2 ± 0.2	6830 ± 30	...	...	...	...	K	...
G010.308-00.150	140 Foot	0.0874 ± 0.0005	31.6 ± 0.2	6800 ± 40	...	...	...	...	K	...
G010.596-00.381	VLA	0.1506 ± 0.0015	23.1 ± 0.2	5704 ± 72	T	Y	4.87 <sup>+0.55</sup> <sub>-0.44</sub>	3.64 <sup>+0.42</sup> <sub>-0.48</sub>	P	Sa14
G012.804-00.207	140 Foot	0.0808 ± 0.0007	30.7 ± 0.3	7620 ± 100	...	...	2.83 <sup>+0.38</sup> <sub>-0.28</sub>	5.61 <sup>+0.26</sup> <sub>-0.35</sub>	P	I13
G013.880+00.285	VLA	0.1568 ± 0.0004	21.5 ± 0.1	5848 ± 19	P	Y	3.79 <sup>+0.49</sup> <sub>-0.26</sub>	4.61 <sup>+0.39</sup> <sub>-0.31</sub>	P	S14
G015.097-00.729	140 Foot	0.0938 ± 0.0008	35.3 ± 0.3	5720 ± 60	...	...	1.94 <sup>+0.16</sup> <sub>-0.10</sub>	6.49 <sup>+0.09</sup> <sub>-0.15</sub>	P	X11
G016.993+00.873	140 Foot	0.0928 ± 0.0006	23.6 ± 0.1	6890 ± 60	...	...	2.38 <sup>+0.27</sup> <sub>-0.24</sub>	6.10 <sup>+0.22</sup> <sub>-0.30</sub>	K	...
G017.928-00.677	VLA	0.1461 ± 0.0158	21.1 ± 2.5	6269 ± 877	T	Y	12.65 <sup>+0.37</sup> <sub>-0.37</sub>	5.41 <sup>+0.23</sup> <sub>-0.31</sub>	K	...
G018.144-00.281	140 Foot	0.1052 ± 0.0008	25.2 ± 0.2	7180 ± 70	...	...	4.00 <sup>+0.36</sup> <sub>-0.30</sub>	4.68 <sup>+0.28</sup> <sub>-0.26</sub>	K	...
G018.584+00.344	VLA	0.1547 ± 0.0135	22.2 ± 2.1	5712 ± 645	T	Y	14.36 <sup>+0.42</sup> <sub>-0.39</sub>	7.02 <sup>+0.25</sup> <sub>-0.31</sub>	K	...
G018.669+01.965	140 Foot	0.0907 ± 0.0006	28.4 ± 0.2	7210 ± 60	...	...	2.42 <sup>+0.25</sup> <sub>-0.25</sub>	6.08 <sup>+0.27</sup> <sub>-0.25</sub>	K	...
G019.064-00.282	140 Foot	0.2916 ± 0.0052	25.2 ± 0.3	5440 ± 70	...	...	4.44 <sup>+0.39</sup> <sub>-0.29</sub>	4.37 <sup>+0.25</sup> <sub>-0.27</sub>	K	...
G019.677-00.134	VLA	0.1166 ± 0.0063	26.6 ± 1.6	6141 ± 429	T	N	11.66 <sup>+0.43</sup> <sub>-0.36</sub>	4.75 <sup>+0.29</sup> <sub>-0.27</sub>	K	...
G019.728-00.113	VLA	0.1363 ± 0.0115	25.0 ± 2.3	5813 ± 629	T	N	11.89 <sup>+0.36</sup> <sub>-0.43</sub>	4.89 <sup>+0.28</sup> <sub>-0.25</sub>	K	...
G020.363-00.014	VLA	0.1416 ± 0.0067	22.5 ± 1.1	6150 ± 367	T	N	11.68 <sup>+0.40</sup> <sub>-0.40</sub>	4.86 <sup>+0.24</sup> <sub>-0.29</sub>	K	...
G020.728-00.105	140 Foot	0.1249 ± 0.0035	26.5 ± 0.1	5590 ± 90	...	...	11.74 <sup>+0.32</sup> <sub>-0.48</sub>	4.91 <sup>+0.23</sup> <sub>-0.31</sub>	K	...
G021.603-00.169	VLA	0.1039 ± 0.0121	23.0 ± 3.8	7959 ± 1399	P	Y	16.03 <sup>+0.53</sup> <sub>-0.49</sub>	8.81 <sup>+0.42</sup> <sub>-0.42</sub>	K	...
G023.423-00.216	140 Foot	0.1162 ± 0.0008	24.3 ± 0.1	6500 ± 55	...	...	5.55 <sup>+1.37</sup> <sub>-0.87</sub>	3.42 <sup>+0.71</sup> <sub>-0.11</sub>	P	B09
G023.661-00.252	VLA	0.1737 ± 0.0079	20.5 ± 1.0	5583 ± 318	T	Y	10.98 <sup>+0.41</sup> <sub>-0.44</sub>	4.76 <sup>+0.23</sup> <sub>-0.31</sub>	K	...
G023.713+00.175	140 Foot	0.1027 ± 0.0015	26.8 ± 0.4	6840 ± 110	...	...	7.63 <sup>+0.16</sup> <sub>-0.15</sub>	3.62 <sup>+0.27</sup> <sub>-0.19</sub>	K	...
G024.195+00.242	VLA	0.1190 ± 0.0187	24.3 ± 4.8	6692 ± 1465	P	Y	...	6.17 <sup>+0.29</sup> <sub>-0.23</sub>	K	...

**Table 6** *continued*



Table 6 (*continued*)

Name	Telescope	$S_L/S_C$	$\Delta V$ (km s <sup>-1</sup> )	$T_e$ (K)	Type <sup>a</sup>	Taper <sup>b</sup>	$d$ (kpc)	$R$ (kpc)	Distance <sup>c</sup> Method	Distance Reference
G024.456+00.489	140 Foot	0.1020 ± 0.0008	29.2 ± 0.5	6370 ± 80	...	...	7.56 <sup>+0.23</sup> <sub>-0.23</sub>	3.80 <sup>+0.28</sup> <sub>-0.21</sub>	K	...
G024.844+00.093	140 Foot	0.1326 ± 0.0012	24.9 ± 0.2	5860 ± 90	...	...	7.48 <sup>+0.23</sup> <sub>-0.23</sub>	3.72 <sup>+0.19</sup> <sub>-0.18</sub>	K	...
G025.382-00.151	140 Foot	0.0974 ± 0.0027	25.6 ± 0.1	7460 ± 70	...	...	3.71 <sup>+0.40</sup> <sub>-0.29</sub>	5.20 <sup>+0.22</sup> <sub>-0.25</sub>	K	...
G025.397+00.033	VLA	0.0853 ± 0.0012	28.0 ± 0.4	7893 ± 142	P	N	16.40 <sup>+0.66</sup> <sub>-0.47</sub>	9.53 <sup>+0.55</sup> <sub>-0.38</sub>	K	...
G025.398+00.562	VLA	0.0774 ± 0.0014	32.0 ± 0.6	7610 ± 177	P	Y	14.11 <sup>+0.41</sup> <sub>-0.36</sub>	7.49 <sup>+0.28</sup> <sub>-0.28</sub>	K	...
G025.401+00.021	VLA	0.1074 ± 0.0046	22.4 ± 1.1	7871 ± 438	T	N	16.00 <sup>+0.59</sup> <sub>-0.44</sub>	9.25 <sup>+0.38</sup> <sub>-0.44</sub>	K	...
G025.867+00.118	140 Foot	0.1189 ± 0.0016	27.3 ± 0.4	6120 ± 100	...	...	7.53 <sup>+0.13</sup> <sub>-0.18</sub>	3.80 <sup>+0.17</sup> <sub>-0.16</sub>	K	...
G027.562+00.084	VLA	0.1594 ± 0.0057	20.8 ± 0.8	5765 ± 261	T	N	9.65 <sup>+0.50</sup> <sub>-0.58</sub>	4.43 <sup>+0.26</sup> <sub>-0.25</sub>	K	...
G028.320+01.243	VLA	0.0819 ± 0.0125	15.0 ± 2.7	14189 ± 2932	P	N	19.42 <sup>+1.15</sup> <sub>-0.98</sub>	12.63 <sup>+1.05</sup> <sub>-0.83</sub>	K	...
G028.451+00.001	VLA	0.0923 ± 0.0058	27.2 ± 1.9	7576 ± 629	T	N	15.25 <sup>+0.50</sup> <sub>-0.46</sub>	8.87 <sup>+0.38</sup> <sub>-0.38</sub>	K	...
G028.581+00.145	VLA	0.0946 ± 0.0079	26.9 ± 2.6	7490 ± 837	T	N	15.83 <sup>+0.55</sup> <sub>-0.59</sub>	9.38 <sup>+0.45</sup> <sub>-0.45</sub>	K	...
G028.746+03.458	GBT	0.1106 ± 0.0007	21.0 ± 0.1	8399 ± 73	...	...	14.79 <sup>+0.36</sup> <sub>-0.54</sub>	8.45 <sup>+0.30</sup> <sub>-0.38</sub>	K	...
G029.770+00.219	VLA	0.1029 ± 0.0071	21.4 ± 1.6	8465 ± 755	T	N	17.46 <sup>+0.93</sup> <sub>-0.60</sub>	11.00 <sup>+0.87</sup> <sub>-0.47</sub>	K	...
G029.956-00.020	140 Foot	0.0992 ± 0.0064	29.8 ± 0.1	6510 ± 90	...	...	5.14 <sup>+0.65</sup> <sub>-0.45</sub>	4.61 <sup>+0.21</sup> <sub>-0.24</sub>	P	Z14
G030.211+00.428	VLA	0.1263 ± 0.0168	17.6 ± 2.6	8355 ± 1446	T	N	15.46 <sup>+0.47</sup> <sub>-0.59</sub>	9.28 <sup>+0.34</sup> <sub>-0.49</sub>	K	...
G030.758-00.047	GBT	0.0908 ± 0.0003	33.5 ± 0.1	6567 ± 30	...	...	7.20 <sup>+0.11</sup> <sub>-0.17</sub>	4.63 <sup>+0.22</sup> <sub>-0.22</sub>	K	...
G031.268+00.478	GBT	0.0944 ± 0.0042	23.2 ± 1.0	8690 ± 462	...	...	14.75 <sup>+0.49</sup> <sub>-0.45</sub>	8.77 <sup>+0.39</sup> <sub>-0.34</sub>	K	...
G031.580+00.074	VLA	0.2544 ± 0.0357	13.5 ± 1.9	5769 ± 992	T	N	4.67 <sup>+0.88</sup> <sub>-0.59</sub>	4.97 <sup>+0.23</sup> <sub>-0.41</sub>	P	Z14
G032.030+00.048	VLA	0.2159 ± 0.0159	16.1 ± 1.2	5720 ± 519	T	N	5.16 <sup>+0.24</sup> <sub>-0.21</sub>	4.81 <sup>+0.08</sup> <sub>-0.09</sub>	P	S14
G032.272-00.226	VLA	0.0850 ± 0.0016	26.9 ± 0.6	8207 ± 200	T	N	12.52 <sup>+0.40</sup> <sub>-0.34</sub>	7.04 <sup>+0.28</sup> <sub>-0.22</sub>	K	...
G032.733+00.209	GBT	0.1638 ± 0.0037	21.0 ± 0.4	5856 ± 156	...	...	12.88 <sup>+0.40</sup> <sub>-0.35</sub>	7.39 <sup>+0.30</sup> <sub>-0.25</sub>	K	...
G032.800+00.190	GBT	0.0750 ± 0.0004	29.5 ± 0.1	8625 ± 49	...	...	13.01 <sup>+0.33</sup> <sub>-0.44</sub>	7.50 <sup>+0.27</sup> <sub>-0.29</sub>	K	...
G032.870-00.427	GBT	0.1817 ± 0.0043	18.2 ± 0.4	6074 ± 176	...	...	10.99 <sup>+0.34</sup> <sub>-0.45</sub>	6.03 <sup>+0.20</sup> <sub>-0.28</sub>	K	...
G032.928+00.606	VLA	0.0723 ± 0.0016	28.9 ± 0.7	8641 ± 244	P	N	17.66 <sup>+0.91</sup> <sub>-0.79</sub>	11.51 <sup>+0.91</sup> <sub>-0.59</sub>	K	...
G032.982-00.338	GBT	0.1485 ± 0.0040	20.9 ± 0.5	6411 ± 207	...	...	10.91 <sup>+0.39</sup> <sub>-0.39</sub>	5.99 <sup>+0.26</sup> <sub>-0.24</sub>	K	...
G034.041+00.052	VLA	0.1489 ± 0.0119	22.7 ± 1.9	5809 ± 591	T	Y	11.48 <sup>+0.32</sup> <sub>-0.43</sub>	6.52 <sup>+0.22</sup> <sub>-0.26</sub>	K	...
G034.133+00.471	VLA	0.1140 ± 0.0013	24.6 ± 0.3	6858 ± 96	T	N	11.55 <sup>+0.32</sup> <sub>-0.40</sub>	6.59 <sup>+0.21</sup> <sub>-0.27</sub>	K	...
G034.256+00.136	GBT	0.0999 ± 0.0006	24.4 ± 0.1	8084 ± 55	...	...	3.29 <sup>+0.30</sup> <sub>-0.38</sub>	5.96 <sup>+0.21</sup> <sub>-0.26</sub>	K	...
G034.686+00.068	VLA	0.1232 ± 0.0058	22.4 ± 1.1	6876 ± 418	T	Y	10.59 <sup>+0.43</sup> <sub>-0.37</sub>	6.03 <sup>+0.25</sup> <sub>-0.22</sub>	K	...
G035.126-00.755	VLA	0.1428 ± 0.0032	19.9 ± 0.5	6793 ± 193	T	N	2.24 <sup>+0.27</sup> <sub>-0.31</sub>	6.62 <sup>+0.26</sup> <sub>-0.23</sub>	K	...

Table 6 *continued*

Table 6 (continued)

Name	Telescope	$S_L/S_C$	$\Delta V$ (km s <sup>-1</sup> )	$T_e$ (K)	Type <sup>a</sup>	Taper <sup>b</sup>	$d$ (kpc)	$R$ (kpc)	Distance <sup>c</sup> Method	Distance Reference
G035.197-01.756	GBT	0.0947 ± 0.0005	23.6 ± 0.0	8603 ± 40	...	...	3.20 <sup>+0.49</sup> <sub>-0.49</sub>	6.00 <sup>+0.28</sup> <sub>-0.30</sub>	P	Z09
G035.948-00.149	VLA	0.1419 ± 0.0202	22.6 ± 3.6	6148 ± 1143	P	N	3.15 <sup>+0.36</sup> <sub>-0.36</sub>	6.10 <sup>+0.21</sup> <sub>-0.28</sub>	K	...
G037.754+00.560	GBT	0.1170 ± 0.0028	23.4 ± 0.8	7163 ± 246	...	...	11.99 <sup>+0.40</sup> <sub>-0.34</sub>	7.43 <sup>+0.28</sup> <sub>-0.24</sub>	K	...
G038.550+00.163	VLA	0.1149 ± 0.0038	23.8 ± 0.9	7019 ± 299	T	N	11.29 <sup>+0.34</sup> <sub>-0.42</sub>	7.05 <sup>+0.24</sup> <sub>-0.26</sub>	K	...
G038.643-00.227	VLA	0.1262 ± 0.0204	18.5 ± 3.5	7992 ± 1725	P	Y	6.51 <sup>+0.14</sup> <sub>-0.13</sub>	5.62 <sup>+0.22</sup> <sub>-0.23</sub>	K	...
G038.652+00.087	GBT	0.0738 ± 0.0015	27.0 ± 0.6	9428 ± 245	...	...	16.66 <sup>+0.79</sup> <sub>-0.85</sub>	11.35 <sup>+0.74</sup> <sub>-0.63</sub>	K	...
G038.840+00.495	VLA	0.0900 ± 0.0120	20.3 ± 3.2	9919 ± 1792	T	Y	16.74 <sup>+0.95</sup> <sub>-0.76</sub>	11.48 <sup>+0.83</sup> <sub>-0.66</sub>	K	...
G038.875+00.308	VLA	0.0882 ± 0.0009	27.8 ± 0.3	7719 ± 107	P	N	14.06 <sup>+0.46</sup> <sub>-0.57</sub>	9.16 <sup>+0.38</sup> <sub>-0.38</sub>	K	...
G039.196+00.224	VLA	0.0726 ± 0.0041	28.7 ± 1.9	8853 ± 658	P	N	14.56 <sup>+0.60</sup> <sub>-0.56</sub>	9.67 <sup>+0.49</sup> <sub>-0.42</sub>	K	...
G039.728-00.396	GBT	0.0874 ± 0.0020	25.7 ± 0.7	8503 ± 255	...	...	9.18 <sup>+0.50</sup> <sub>-0.46</sub>	6.00 <sup>+0.24</sup> <sub>-0.22</sub>	K	...
G039.864+00.645	VLA	0.0780 ± 0.0048	27.6 ± 2.0	8606 ± 707	T	N	16.52 <sup>+0.72</sup> <sub>-0.89</sub>	11.37 <sup>+0.69</sup> <sub>-0.69</sub>	K	...
G040.503+02.537	GBT	0.1074 ± 0.0006	22.4 ± 0.1	8223 ± 55	...	...	1.41 <sup>+0.30</sup> <sub>-0.32</sub>	7.35 <sup>+0.24</sup> <sub>-0.28</sub>	K	...
G043.146+00.013	VLA	0.0868 ± 0.0005	31.1 ± 0.2	6942 ± 48	T	Y	11.59 <sup>+0.45</sup> <sub>-0.42</sub>	7.91 <sup>+0.31</sup> <sub>-0.27</sub>	K	...
G043.165-00.031	VLA	0.0542 ± 0.0007	39.0 ± 0.6	8648 ± 144	T	N	11.05 <sup>+0.90</sup> <sub>-0.90</sub>	7.47 <sup>+0.68</sup> <sub>-0.48</sub>	P	Z13
G043.168+00.019	VLA	0.1280 ± 0.0015	24.1 ± 0.3	6282 ± 92	T	N	10.94 <sup>+0.98</sup> <sub>-0.77</sub>	7.45 <sup>+0.67</sup> <sub>-0.48</sub>	P	Z13
G043.170-00.004	VLA	0.0768 ± 0.0003	30.7 ± 0.1	7876 ± 35	T	Y	11.11 <sup>+0.83</sup> <sub>-0.98</sub>	7.60 <sup>+0.54</sup> <sub>-0.64</sub>	P	Z13
G043.432+00.516	VLA	0.0930 ± 0.0138	25.1 ± 5.6	8119 ± 1883	T	Y	12.93 <sup>+0.58</sup> <sub>-0.46</sub>	8.95 <sup>+0.41</sup> <sub>-0.38</sub>	K	...
G043.818+00.395	VLA	0.0788 ± 0.0056	31.0 ± 2.6	7806 ± 750	T	Y	12.59 <sup>+0.57</sup> <sub>-0.42</sub>	8.74 <sup>+0.44</sup> <sub>-0.29</sub>	K	...
G043.968+00.993	VLA	0.0822 ± 0.0054	31.9 ± 2.5	7255 ± 647	P	N	13.88 <sup>+0.66</sup> <sub>-0.53</sub>	9.79 <sup>+0.53</sup> <sub>-0.46</sub>	K	...
G044.418+00.535	GBT	0.0926 ± 0.0026	24.3 ± 0.7	8492 ± 299	...	...	16.93 <sup>+0.92</sup> <sub>-1.06</sub>	12.41 <sup>+0.86</sup> <sub>-0.92</sub>	K	...
G044.501+00.332	VLA	0.1064 ± 0.0063	19.7 ± 1.3	9044 ± 694	T	Y	15.38 <sup>+0.88</sup> <sub>-0.70</sub>	11.11 <sup>+0.70</sup> <sub>-0.60</sub>	K	...
G045.197+00.740	GBT	0.0556 ± 0.0010	30.5 ± 0.6	10841 ± 245	...	...	14.50 <sup>+0.83</sup> <sub>-0.54</sub>	10.45 <sup>+0.64</sup> <sub>-0.44</sub>	K	...
G045.453+00.044	GBT	0.0871 ± 0.0007	27.6 ± 0.1	8026 ± 63	...	...	8.11 <sup>+1.43</sup> <sub>-1.10</sub>	6.26 <sup>+0.57</sup> <sub>-0.31</sub>	P	W14
G046.495-00.241	140 Foot	0.1989 ± 0.0071	20.1 ± 0.2	4860 ± 80	...	...	5.71 <sup>+0.16</sup> <sub>-0.08</sub>	6.27 <sup>+0.21</sup> <sub>-0.19</sub>	K	...
G048.719+01.147	VLA	0.0943 ± 0.0083	26.6 ± 2.8	7606 ± 900	T	N	12.90 <sup>+0.63</sup> <sub>-0.59</sub>	9.70 <sup>+0.45</sup> <sub>-0.45</sub>	K	...
G048.922-00.285	140 Foot	0.0805 ± 0.0005	26.7 ± 0.2	8440 ± 60	...	...	5.27 <sup>+0.22</sup> <sub>-0.19</sub>	6.29 <sup>+0.01</sup> <sub>-0.00</sub>	P	W14
G049.002-00.303	140 Foot	0.1859 ± 0.0017	24.4 ± 0.2	8170 ± 50	...	...	5.30 <sup>+0.20</sup> <sub>-0.21</sub>	6.30 <sup>+0.01</sup> <sub>-0.00</sub>	P	W14
G049.201-00.365	140 Foot	0.0650 ± 0.0003	30.3 ± 0.1	9070 ± 70	...	...	5.31 <sup>+0.18</sup> <sub>-0.22</sub>	6.31 <sup>+0.01</sup> <sub>-0.00</sub>	P	W14
G049.384-00.298	140 Foot	0.0786 ± 0.0006	31.6 ± 0.3	8585 ± 65	...	...	5.43 <sup>+0.11</sup> <sub>-0.10</sub>	6.37 <sup>+0.19</sup> <sub>-0.11</sub>	K	...
G049.399-00.490	VLA	0.1167 ± 0.0021	24.1 ± 0.5	6675 ± 151	T	Y	5.34 <sup>+0.36</sup> <sub>-0.26</sub>	6.33 <sup>+0.01</sup> <sub>-0.00</sub>	P	W14

Table 6 continued

Table 6 (continued)

Name	Telescope	$S_L/S_C$	$\Delta V$ (km s <sup>-1</sup> )	$T_e$ (K)	Type <sup>a</sup>	Taper <sup>b</sup>	$d$ (kpc)	$R$ (kpc)	Distance <sup>c</sup> Method	Distance Reference
G049.489-00.378	GBT	0.0903 ± 0.0003	30.2 ± 0.0	7166 ± 25	...	...	5.42 <sup>+0.11</sup> <sub>-0.10</sub>	6.46 <sup>+0.19</sup> <sub>-0.15</sub>	K	...
G052.098+01.042	VLA	0.0854 ± 0.0011	28.7 ± 0.4	7725 ± 134	T	N	3.53 <sup>+1.36</sup> <sub>-0.82</sub>	6.77 <sup>+0.19</sup> <sub>-0.19</sub>	P	O10
G052.232+00.735	VLA	0.1083 ± 0.0085	20.8 ± 1.8	8258 ± 841	T	Y	10.47 <sup>+0.42</sup> <sub>-0.59</sub>	8.44 <sup>+0.32</sup> <sub>-0.32</sub>	K	...
G052.766+00.333	GBT	0.0841 ± 0.0011	25.4 ± 0.4	8970 ± 186	...	...	9.24 <sup>+0.55</sup> <sub>-0.37</sub>	7.84 <sup>+0.33</sup> <sub>-0.23</sub>	K	...
G055.114+02.422	VLA	0.0484 ± 0.0013	32.6 ± 1.0	11357 ± 409	T	Y	16.12 <sup>+1.23</sup> <sub>-1.07</sub>	13.24 <sup>+1.13</sup> <sub>-0.92</sub>	K	...
G059.796+00.241	GBT	0.0975 ± 0.0008	21.8 ± 0.2	9068 ± 120	...	...	8.79 <sup>+0.48</sup> <sub>-0.65</sub>	8.51 <sup>+0.32</sup> <sub>-0.34</sub>	K	...
G060.592+01.572	VLA	0.0692 ± 0.0048	26.8 ± 2.2	9883 ± 922	T	Y	12.14 <sup>+0.75</sup> <sub>-0.86</sub>	10.86 <sup>+0.53</sup> <sub>-0.66</sub>	K	...
G060.881-00.135	GBT	0.1229 ± 0.0010	21.2 ± 0.2	7463 ± 77	...	...	4.06 <sup>+0.08</sup> <sub>-0.09</sub>	7.66 <sup>+0.31</sup> <sub>-0.22</sub>	K	...
G061.473+00.094	GBT	0.0846 ± 0.0004	26.0 ± 0.1	8857 ± 43	...	...	3.99 <sup>+0.07</sup> <sub>-0.09</sub>	7.52 <sup>+0.19</sup> <sub>-0.22</sub>	K	...
G061.720+00.863	VLA	0.0777 ± 0.0076	25.9 ± 3.3	9170 ± 1282	P	N	13.96 <sup>+0.96</sup> <sub>-1.11</sub>	12.38 <sup>+0.85</sup> <sub>-0.91</sub>	K	...
G062.577+02.389	VLA	0.0766 ± 0.0079	22.0 ± 2.7	10626 ± 1470	T	Y	13.97 <sup>+0.96</sup> <sub>-1.12</sub>	12.57 <sup>+0.79</sup> <sub>-0.92</sub>	K	...
G063.164+00.449	GBT	0.0994 ± 0.0011	25.1 ± 0.1	7760 ± 90	...	...	3.76 <sup>+0.08</sup> <sub>-0.07</sub>	7.78 <sup>+0.25</sup> <sub>-0.25</sub>	K	...
G064.130-00.475	GBT	0.0973 ± 0.0005	23.9 ± 0.1	8452 ± 58	...	...	3.64 <sup>+0.08</sup> <sub>-0.07</sub>	7.66 <sup>+0.19</sup> <sub>-0.21</sub>	K	...
G068.144+00.915	GBT	0.0697 ± 0.0009	24.7 ± 0.3	10834 ± 207	...	...	11.92 <sup>+0.90</sup> <sub>-0.98</sub>	11.53 <sup>+0.88</sup> <sub>-0.53</sub>	K	...
G069.922+01.511	GBT	0.0712 ± 0.0003	27.0 ± 0.1	9703 ± 50	...	...	11.56 <sup>+0.88</sup> <sub>-1.04</sub>	11.69 <sup>+0.61</sup> <sub>-0.79</sub>	K	...
G070.280+01.583	VLA	0.0901 ± 0.0009	25.3 ± 0.3	8214 ± 109	T	Y	7.92 <sup>+0.78</sup> <sub>-0.63</sub>	9.37 <sup>+0.41</sup> <sub>-0.41</sub>	K	...
G070.293+01.599	GBT	0.0505 ± 0.0005	37.0 ± 0.2	10297 ± 121	...	...	7.96 <sup>+0.69</sup> <sub>-0.69</sub>	9.36 <sup>+0.43</sup> <sub>-0.37</sub>	K	...
G070.304+01.595	VLA	0.0992 ± 0.0017	23.4 ± 0.4	8211 ± 182	T	N	7.36 <sup>+0.65</sup> <sub>-0.71</sub>	8.95 <sup>+0.48</sup> <sub>-0.26</sub>	K	...
G070.329+01.589	VLA	0.0745 ± 0.0012	30.6 ± 0.5	8244 ± 170	T	N	7.35 <sup>+0.69</sup> <sub>-0.69</sub>	9.03 <sup>+0.40</sup> <sub>-0.35</sub>	K	...
G070.765+01.820	VLA	0.0896 ± 0.0105	24.9 ± 3.4	8412 ± 1317	T	N	12.68 <sup>+1.02</sup> <sub>-1.19</sub>	12.65 <sup>+0.83</sup> <sub>-0.90</sub>	K	...
G071.150+00.397	VLA	0.1035 ± 0.0016	24.2 ± 0.4	7551 ± 147	P	Y	6.56 <sup>+0.81</sup> <sub>-0.58</sub>	8.85 <sup>+0.30</sup> <sub>-0.39</sub>	K	...
G073.878+01.023	VLA	0.0744 ± 0.0037	30.8 ± 1.8	8177 ± 545	T	N	9.10 <sup>+1.03</sup> <sub>-0.63</sub>	10.52 <sup>+0.66</sup> <sub>-0.46</sub>	K	...
G074.155+01.646	VLA	0.1929 ± 0.0238	15.9 ± 2.0	6327 ± 980	P	Y	7.68 <sup>+0.75</sup> <sub>-0.75</sub>	9.68 <sup>+0.46</sup> <sub>-0.46</sub>	K	...
G074.753+00.912	VLA	0.0923 ± 0.0056	27.9 ± 1.9	7386 ± 592	T	N	9.03 <sup>+0.86</sup> <sub>-0.80</sub>	10.52 <sup>+0.61</sup> <sub>-0.53</sub>	K	...
G075.768+00.344	VLA	0.0900 ± 0.0005	27.0 ± 0.2	7743 ± 57	T	Y	3.49 <sup>+0.28</sup> <sub>-0.28</sub>	8.20 <sup>+0.05</sup> <sub>-0.05</sub>	P	A11
G075.842+00.404	GBT	0.0751 ± 0.0003	30.5 ± 0.1	8363 ± 32	...	...	3.73 <sup>+0.52</sup> <sub>-0.39</sub>	8.26 <sup>+0.11</sup> <sub>-0.08</sub>	P	R12
G076.155-00.286	GBT	0.0651 ± 0.0005	30.9 ± 0.2	9498 ± 119	...	...	7.13 <sup>+0.72</sup> <sub>-0.72</sub>	9.66 <sup>+0.36</sup> <sub>-0.51</sub>	K	...
G076.384-00.621	GBT	0.0407 ± 0.0002	42.0 ± 0.2	11245 ± 92	...	...	1.28 <sup>+0.11</sup> <sub>-0.08</sub>	8.13 <sup>+0.01</sup> <sub>-0.01</sub>	P	X13
G078.032+00.606	GBT	0.0832 ± 0.0005	27.2 ± 0.2	8567 ± 86	...	...	1.51 <sup>+0.07</sup> <sub>-0.09</sub>	8.16 <sup>+0.00</sup> <sub>-0.00</sub>	P	R12
G078.147+01.820	GBT	0.0910 ± 0.0008	24.6 ± 0.2	8596 ± 107	...	...	1.51 <sup>+0.07</sup> <sub>-0.10</sub>	8.16 <sup>+0.00</sup> <sub>-0.00</sub>	P	R12

Table 6 continued

Table 6 (*continued*)

Name	Telescope	$S_L/S_C$	$\Delta V$ (km s <sup>-1</sup> )	$T_e$ (K)	Type <sup>a</sup>	Taper <sup>b</sup>	$d$ (kpc)	$R$ (kpc)	Distance <sup>c</sup> Method	Distance Reference
G078.886+00.709	VLA	0.1525 ± 0.0048	19.5 ± 0.7	6530 ± 260	T	N	3.31 <sup>+0.29</sup> <sub>-0.27</sub>	8.35 <sup>+0.06</sup> <sub>-0.05</sub>	P	R12
G079.270+02.488	GBT	0.1161 ± 0.0021	20.8 ± 0.6	7977 ± 222	...	...	1.50 <sup>+0.08</sup> <sub>-0.09</sub>	8.20 <sup>+0.00</sup> <sub>-0.00</sub>	P	R12
G079.293+01.296	GBT	0.0729 ± 0.0007	30.0 ± 0.1	8693 ± 86	...	...	7.22 <sup>+0.85</sup> <sub>-0.80</sub>	9.90 <sup>+0.55</sup> <sub>-0.42</sub>	K	...
G080.350+00.718	GBT	0.0699 ± 0.0007	26.5 ± 0.3	10250 ± 155	...	...	9.31 <sup>+1.03</sup> <sub>-0.89</sub>	11.46 <sup>+0.68</sup> <sub>-0.68</sub>	K	...
G080.362+01.212	GBT	0.1058 ± 0.0030	23.0 ± 0.7	7921 ± 294	...	...	1.62 <sup>+0.06</sup> <sub>-0.08</sub>	8.21 <sup>+0.00</sup> <sub>-0.00</sub>	P	R12
G080.938-00.129	GBT	0.0774 ± 0.0004	28.7 ± 0.1	8853 ± 62	...	...	1.49 <sup>+0.09</sup> <sub>-0.07</sub>	8.24 <sup>+0.00</sup> <sub>-0.00</sub>	P	R12
G081.681+00.540	GBT	0.0608 ± 0.0002	35.9 ± 0.1	8829 ± 36	...	...	1.49 <sup>+0.09</sup> <sub>-0.08</sub>	8.26 <sup>+0.00</sup> <sub>-0.00</sub>	P	R12
G082.566+00.362	GBT	0.1038 ± 0.0011	23.4 ± 0.2	8030 ± 128	...	...	1.49 <sup>+0.10</sup> <sub>-0.06</sub>	8.28 <sup>+0.00</sup> <sub>-0.00</sub>	P	R12
G083.792+03.269	GBT	0.0943 ± 0.0012	23.1 ± 0.3	8643 ± 184	...	...	1.49 <sup>+0.09</sup> <sub>-0.08</sub>	8.31 <sup>+0.01</sup> <sub>-0.01</sub>	P	R12
G085.241+00.021	GBT	0.0799 ± 0.0011	26.9 ± 0.3	8824 ± 177	...	...	5.93 <sup>+0.70</sup> <sub>-0.86</sub>	9.76 <sup>+0.44</sup> <sub>-0.44</sub>	K	...
G092.920+02.823	140 Foot	0.1308 ± 0.0028	24.8 ± 0.5	10840 ± 270	...	...	7.08 <sup>+1.03</sup> <sub>-0.89</sub>	11.31 <sup>+0.65</sup> <sub>-0.69</sub>	K	...
G096.289+02.593	VLA	0.0634 ± 0.0022	28.3 ± 1.1	10169 ± 464	T	Y	10.13 <sup>+1.53</sup> <sub>-1.22</sub>	13.76 <sup>+1.31</sup> <sub>-0.87</sub>	K	...
G096.434+01.324	VLA	0.1125 ± 0.0085	21.8 ± 1.8	7745 ± 762	T	N	8.50 <sup>+0.70</sup> <sub>-1.40</sub>	12.44 <sup>+0.65</sup> <sub>-0.95</sub>	K	...
G097.515+03.173	VLA	0.0711 ± 0.0017	28.2 ± 0.7	9226 ± 281	T	Y	7.27 <sup>+1.10</sup> <sub>-0.82</sub>	11.78 <sup>+0.78</sup> <sub>-0.64</sub>	P	H15
G097.528+03.184	VLA	0.1029 ± 0.0060	24.1 ± 1.6	7726 ± 584	T	N	7.26 <sup>+1.12</sup> <sub>-0.89</sub>	11.76 <sup>+0.81</sup> <sub>-0.63</sub>	P	H15
G101.016+02.590	VLA	0.1510 ± 0.0218	16.8 ± 2.7	7600 ± 1434	T	N	6.87 <sup>+1.09</sup> <sub>-0.89</sub>	11.80 <sup>+0.79</sup> <sub>-0.69</sub>	K	...
G108.191+00.586	GBT	0.0759 ± 0.0004	25.8 ± 0.1	9590 ± 59	...	...	4.25 <sup>+0.62</sup> <sub>-0.46</sub>	10.48 <sup>+0.40</sup> <sub>-0.33</sub>	P	C14
G108.375-01.056	GBT	0.0806 ± 0.0009	26.1 ± 0.3	8992 ± 131	...	...	5.01 <sup>+0.77</sup> <sub>-0.88</sub>	10.98 <sup>+0.64</sup> <sub>-0.59</sub>	K	...
G108.764-00.952	GBT	0.0706 ± 0.0004	29.6 ± 0.2	9404 ± 81	...	...	4.54 <sup>+0.86</sup> <sub>-0.74</sub>	10.61 <sup>+0.71</sup> <sub>-0.43</sub>	K	...
G109.104-00.347	VLA	0.1998 ± 0.0222	25.7 ± 2.9	4061 ± 554	T	N	4.05 <sup>+0.69</sup> <sub>-0.85</sub>	10.31 <sup>+0.57</sup> <sub>-0.49</sub>	K	...
G110.099+00.042	GBT	0.0543 ± 0.0003	38.0 ± 0.2	9240 ± 75	...	...	4.56 <sup>+0.76</sup> <sub>-0.82</sub>	10.75 <sup>+0.58</sup> <sub>-0.58</sub>	K	...
G111.558+00.804	GBT	0.0829 ± 0.0005	27.1 ± 0.1	8483 ± 51	...	...	2.62 <sup>+0.15</sup> <sub>-0.10</sub>	9.62 <sup>+0.09</sup> <sub>-0.06</sub>	P	M09
G111.612+00.371	GBT	0.0885 ± 0.0005	26.8 ± 0.1	8428 ± 68	...	...	5.99 <sup>+0.85</sup> <sub>-1.04</sub>	11.92 <sup>+0.68</sup> <sub>-0.79</sub>	K	...
G112.212+00.229	GBT	0.0777 ± 0.0008	28.8 ± 0.2	8641 ± 118	...	...	3.62 <sup>+0.93</sup> <sub>-0.60</sub>	10.28 <sup>+0.66</sup> <sub>-0.44</sub>	K	...
G115.785-01.561	GBT	0.0806 ± 0.0017	26.8 ± 0.6	8794 ± 242	...	...	3.56 <sup>+0.79</sup> <sub>-0.68</sub>	10.40 <sup>+0.59</sup> <sub>-0.50</sub>	K	...
G118.345+04.856	140 Foot	0.0911 ± 0.0193	20.7 ± 0.3	9540 ± 1050	...	...	0.56 <sup>+0.53</sup> <sub>-0.42</sub>	8.66 <sup>+0.32</sup> <sub>-0.28</sub>	K	...
G124.637+02.535	VLA	0.0659 ± 0.0011	30.5 ± 0.6	9181 ± 198	P	N	7.31 <sup>+0.90</sup> <sub>-1.47</sub>	13.44 <sup>+1.22</sup> <sub>-0.86</sub>	K	...
G124.894+00.323	GBT	0.0781 ± 0.0031	27.0 ± 1.2	8975 ± 460	...	...	3.22 <sup>+0.71</sup> <sub>-0.65</sub>	10.50 <sup>+0.65</sup> <sub>-0.47</sub>	K	...
G128.772+02.009	GBT	0.0854 ± 0.0028	20.9 ± 0.7	10361 ± 427	...	...	8.51 <sup>+1.82</sup> <sub>-1.14</sub>	15.14 <sup>+1.64</sup> <sub>-1.09</sub>	K	...
G132.156-00.729	GBT	0.0769 ± 0.0006	24.9 ± 0.2	9785 ± 123	...	...	4.83 <sup>+0.96</sup> <sub>-0.90</sub>	12.09 <sup>+0.86</sup> <sub>-0.74</sub>	K	...

Table 6 *continued*

Table 6 (continued)

Name	Telescope	$S_L/S_C$	$\Delta V$ (km s <sup>-1</sup> )	$T_e$ (K)	Type <sup>a</sup>	Taper <sup>b</sup>	$d$ (kpc)	$R$ (kpc)	Distance <sup>c</sup> Method	Distance Reference
G133.712+01.221	GBT	0.0760 ± 0.0003	27.7 ± 0.0	8977 ± 38	...	...	1.95 <sup>+0.04</sup> <sub>-0.04</sub>	9.79 <sup>+0.03</sup> <sub>-0.03</sub>	P	X06:H06
G133.781+01.428	GBT	0.0785 ± 0.0005	27.5 ± 0.1	8752 ± 74	...	...	1.94 <sup>+0.05</sup> <sub>-0.03</sub>	9.79 <sup>+0.04</sup> <sub>-0.02</sub>	P	X06:H06
G135.188+02.701	VLA	0.1347 ± 0.0204	19.9 ± 3.3	7259 ± 1414	P	Y	7.37 <sup>+1.36</sup> <sub>-1.26</sub>	14.52 <sup>+1.27</sup> <sub>-1.18</sub>	K	...
G136.884+00.911	GBT	0.0995 ± 0.0025	23.5 ± 0.6	8204 ± 257	...	...	1.95 <sup>+0.04</sup> <sub>-0.04</sub>	9.86 <sup>+0.03</sup> <sub>-0.03</sub>	P	X06:H06
G138.494+01.634	GBT	0.0969 ± 0.0014	23.8 ± 0.3	8302 ± 131	...	...	2.87 <sup>+0.72</sup> <sub>-0.58</sub>	10.75 <sup>+0.56</sup> <sub>-0.61</sub>	K	...
G141.084-01.063	VLA	0.1400 ± 0.0203	18.8 ± 3.2	7300 ± 1431	T	Y	1.99 <sup>+0.61</sup> <sub>-0.49</sub>	10.04 <sup>+0.46</sup> <sub>-0.57</sub>	K	...
G150.596-00.955	GBT	0.0671 ± 0.0005	27.8 ± 0.1	10016 ± 83	...	...	2.74 <sup>+0.56</sup> <sub>-0.65</sub>	10.77 <sup>+0.59</sup> <sub>-0.63</sub>	K	...
G151.609-00.233	GBT	0.0543 ± 0.0004	31.7 ± 0.2	10795 ± 98	...	...	7.00 <sup>+1.44</sup> <sub>-1.25</sub>	14.75 <sup>+1.56</sup> <sub>-1.10</sub>	K	...
G154.646+02.438	GBT	0.0673 ± 0.0009	28.6 ± 0.4	9734 ± 175	...	...	4.39 <sup>+1.05</sup> <sub>-0.79</sub>	12.33 <sup>+1.17</sup> <sub>-0.67</sub>	K	...
G155.372+02.613	GBT	0.0703 ± 0.0013	25.6 ± 0.5	10253 ± 309	...	...	6.65 <sup>+1.36</sup> <sub>-1.26</sub>	14.76 <sup>+1.30</sup> <sub>-1.30</sub>	K	...
G169.180-00.905	GBT	0.0872 ± 0.0013	23.1 ± 0.4	9345 ± 179	...	...	...	$d$	K	...
G173.599+02.803	GBT	0.1060 ± 0.0013	20.9 ± 0.3	8612 ± 137	...	...	$d$	$d$	K	...
G173.937+00.298	GBT	0.0935 ± 0.0014	23.0 ± 0.3	8829 ± 158	...	...	$d$	$d$	K	...
G192.638-00.008	GBT	0.0971 ± 0.0010	22.1 ± 0.2	8833 ± 107	...	...	1.58 <sup>+0.08</sup> <sub>-0.06</sub>	9.89 <sup>+0.08</sup> <sub>-0.06</sub>	P	R10
G196.448-01.673	VLA	0.0928 ± 0.0035	22.6 ± 0.9	8884 ± 435	T	Y	5.23 <sup>+0.41</sup> <sub>-0.33</sub>	13.44 <sup>+0.40</sup> <sub>-0.32</sub>	P	H07
G209.037-19.377	GBT	0.0878 ± 0.0007	26.1 ± 0.0	8322 ± 55	...	...	0.41 <sup>+0.01</sup> <sub>-0.00</sub>	8.70 <sup>+0.01</sup> <sub>-0.00</sub>	P	S07:M07;K08
G213.076-02.213	GBT	0.0564 ± 0.0006	28.6 ± 0.3	11343 ± 162	...	...	6.58 <sup>+1.27</sup> <sub>-1.27</sub>	14.27 <sup>+1.23</sup> <sub>-1.15</sub>	K	...
G213.703-12.601	GBT	0.0750 ± 0.0004	29.8 ± 0.1	8986 ± 65	...	...	0.80 <sup>+0.42</sup> <sub>-0.34</sub>	9.01 <sup>+0.42</sup> <sub>-0.33</sub>	K	...
G218.737+01.850	GBT	0.0702 ± 0.0007	24.6 ± 0.3	10671 ± 143	...	...	5.39 <sup>+0.89</sup> <sub>-1.11</sub>	12.99 <sup>+0.86</sup> <sub>-1.00</sub>	K	...
G220.524-02.759	GBT	0.0473 ± 0.0021	31.8 ± 1.7	12037 ± 725	...	...	7.62 <sup>+1.47</sup> <sub>-1.35</sub>	14.92 <sup>+1.42</sup> <sub>-1.31</sub>	K	...
G225.470-02.587	GBT	0.1141 ± 0.0020	22.6 ± 0.4	7537 ± 158	...	...	0.09 <sup>+0.43</sup> <sub>-0.08</sub>	8.56 <sup>+0.28</sup> <sub>-0.24</sub>	K	...
G227.760-00.127	GBT	0.0485 ± 0.0007	28.9 ± 0.4	12495 ± 249	...	...	4.33 <sup>+0.84</sup> <sub>-0.84</sub>	11.73 <sup>+0.72</sup> <sub>-0.72</sub>	K	...
G231.481-04.401	GBT	0.1011 ± 0.0024	20.5 ± 0.6	9098 ± 286	...	...	4.49 <sup>+0.79</sup> <sub>-0.85</sub>	11.60 <sup>+0.73</sup> <sub>-0.68</sub>	K	...
G233.753-00.193	GBT	0.0822 ± 0.0015	24.1 ± 0.4	9482 ± 209	...	...	2.68 <sup>+0.67</sup> <sub>-0.63</sub>	10.13 <sup>+0.54</sup> <sub>-0.46</sub>	K	...
G243.244+00.406	GBT	0.0793 ± 0.0014	22.3 ± 0.2	10477 ± 214	...	...	4.09 <sup>+0.98</sup> <sub>-0.60</sub>	10.84 <sup>+0.73</sup> <sub>-0.52</sub>	K	...
G345.284+01.463	140 Foot	0.0891 ± 0.0006	24.1 ± 0.2	8530 ± 640	...	...	$d$	$d$	K	...
G345.410-00.953	140 Foot	0.1036 ± 0.0004	26.3 ± 0.1	6960 ± 50	...	...	$d$	$d$	K	...
G348.249-00.971	140 Foot	0.0918 ± 0.0005	28.2 ± 0.2	6610 ± 100	...	...	$d$	$d$	K	...
G348.710-01.044	140 Foot	0.1067 ± 0.0008	24.6 ± 0.2	7150 ± 90	...	...	3.32 <sup>+0.34</sup> <sub>-0.27</sub>	5.12 <sup>+0.25</sup> <sub>-0.32</sub>	P	W12
G351.130+00.449	140 Foot	0.1272 ± 0.0015	22.1 ± 0.2	6650 ± 70	...	...	$d$	$d$	K	...

Table 6 continued

Table 6 (*continued*)

Name	Telescope	$S_L/S_C$	$\Delta V$ (km s <sup>-1</sup> )	$T_e$ (K)	Type <sup>a</sup>	Taper <sup>b</sup>	$d$ (kpc)	$R$ (kpc)	Distance <sup>c</sup> Method	Distance Reference
G351.170+00.704	140 Foot	0.1283 ± 0.0009	25.9 ± 0.1	5610 ± 20	...	...	...	$d$	K	...
G351.246+00.673	VLA	0.1131 ± 0.0003	25.1 ± 0.1	6772 ± 24	T	Y	1.31 <sup>+0.15</sup> <sub>-0.12</sub>	7.05 <sup>+0.12</sup> <sub>-0.15</sub>	P	W14
G351.311+00.663	VLA	0.1301 ± 0.0004	24.1 ± 0.1	6230 ± 27	T	Y	1.32 <sup>+0.16</sup> <sub>-0.12</sub>	7.04 <sup>+0.12</sup> <sub>-0.15</sub>	P	W14
G351.367+00.640	140 Foot	0.1151 ± 0.0012	23.9 ± 0.1	6840 ± 40	...	...	1.31 <sup>+0.16</sup> <sub>-0.12</sub>	7.05 <sup>+0.11</sup> <sub>-0.17</sub>	P	W14
G351.472-00.458	140 Foot	0.1067 ± 0.0012	23.3 ± 0.5	7460 ± 120	...	...	...	...	K	...
G351.646-01.252	140 Foot	0.0848 ± 0.0005	28.1 ± 0.1	7620 ± 30	...	...	...	$d$	K	...
G351.688-01.169	140 Foot	0.1029 ± 0.0006	23.6 ± 0.1	7560 ± 90	...	...	...	$d$	K	...
G352.597-00.188	140 Foot	0.1172 ± 0.0025	20.9 ± 0.9	7560 ± 240	...	...	...	$d$	K	...
G353.038+00.581	140 Foot	0.1040 ± 0.0012	28.6 ± 0.1	6250 ± 30	...	...	...	$d$	K	...
G353.092+00.857	140 Foot	0.2296 ± 0.0024	28.7 ± 0.1	5630 ± 40	...	...	...	$d$	K	...
G353.195+00.910	140 Foot	0.0826 ± 0.0006	30.8 ± 0.2	7100 ± 40	...	...	...	$d$	K	...
G353.408-00.381	140 Foot	0.0912 ± 0.0008	24.0 ± 0.2	8480 ± 60	...	...	...	$d$	K	...

<sup>a</sup>"P" if measured at the location of peak continuum brightness; "T" if measured within the watershed segmentation region

<sup>b</sup>"N" if non-tapered image measurement; "Y" if  $w$ -tapered image measurement

<sup>c</sup>"K" for Monte Carlo kinematic distance; "P" for parallax distance

<sup>d</sup>Kinematic distances are unreliable in the direction of the Galactic center and anti-center

**References**—(A11) Ando et al. (2011); (B09) Brunthaler et al. (2009); (C14) Choi et al. (2014); (H06) Hachisuka et al. (2006); (H07) Honma et al. (2007); (H15) Hachisuka et al. (2015); (I13) Immer et al. (2013); (K08) Kim et al. (2008); (M07) Menten et al. (2007); (M09) Moscadelli et al. (2009); (O10) Oh et al. (2010); (RD09) Roman-Duval et al. (2009); (R09a) Reid et al. (2009a); (R09c) Reid et al. (2009b); (R10) Rygl et al. (2010); (R12) Rygl et al. (2012); (S07) Sandstrom et al. (2007); (S10) Sato et al. (2010); (S14) Sato et al. (2014); (Sa14) Sanna et al. (2014); (U12) Urquhart et al. (2012); (W12) Wu et al. (2012); (W14) Wu et al. (2014); (X06) Xu et al. (2006); (X11) Xu et al. (2011); (X13) Xu et al. (2013); (Z09) Zhang et al. (2009); (Z13) Zhang et al. (2013); (Z14) Zhang et al. (2014)

ence may be due to a problem with the derivation of the RRL-to-continuum brightness ratio or perhaps due to a fundamental difference in the RRL and/or continuum emission measured by the different telescopes. We know that there are a few issues with how the single dish RRL-to-continuum ratios are derived. B15 measured the continuum flux densities of their nebulae at  $\nu_C = 8556$  MHz, whereas the average frequency of their observed RRL transitions is  $\langle \nu_L \rangle = 8902$  MHz. In Appendix A, we show that the B15 strategy overestimates the true electron temperature by  $\sim 6\%$ . Furthermore, we do not scale the single dish and VLA RRL-to-continuum brightness ratios to a common frequency because each survey observed similar RRL transitions. The typical VLA  $\langle \text{Hn}\alpha \rangle$  weighted frequency is within 2% of the B15 average RRL frequency. Neither of these two effects can fully explain the observed 10% difference between the single dish and VLA RRL-to-continuum brightness ratios.

There are several factors that might affect the measured continuum and/or RRL flux densities: the single dish continuum flux densities are uncertain due to poor continuum background subtraction; the single dish telescopes are not pointed at the center of the continuum source during the RRL observation; the VLA is not sensitive to extended emission associated with the H II region; and/or the VLA is seeing more optically thick gas. (1) The continuum flux densities are the largest source of uncertainty in the single dish electron temperature derivation (see B15). If the continuum background level is poorly constrained, then the single dish continuum flux densities will be inaccurate. We limit our analysis to high continuum QF single dish nebulae, however, so these problems should be minimal. Furthermore, random errors in the single dish continuum background levels would not cause the observed systematic difference in single dish vs. interferometric electron temperatures. (2) The single dish RRL spectra must be measured at the location of the peak continuum brightness. If the telescope is not pointed properly, then the RRL flux densities will be underestimated. This is also not a likely explanation for the discrepancy, because B15 peaked on source for their RRL observations. (3) The VLA is not sensitive to diffuse emission. If the source of such emission has a different density and/or temperature, the VLA electron temperatures will differ from the single dish values. (4) Finally, the nebulae may be optically thick, and/or the compact emission visible to the VLA is more optically thick than the diffuse emission missed by the VLA. Optical depth effects such as these would lead to an underestimation of the VLA continuum flux densities and electron temperatures. Some

or all of these issues may be contributing to the remaining 4% discrepancy between the single dish and VLA RRL-to-continuum brightness ratios.

We wish to use as much data as possible to constrain the metallicity structure of the Galactic disk. Therefore, in subsequent analyses that combine the single dish and VLA electron temperatures, we multiply the single dish electron temperatures by 0.9 to accommodate the systematic offset between the VLA and single dish data.

#### 5.4. Distances

Distances to Galactic H II regions are derived in three main ways: (1) spectrophotometrically, (2) geometrically, and (3) kinematically. Spectrophotometric distances are only available for optically unobscured nebulae. Since most of the nebulae in our sample are very distant with lines of sight passing through the Galactic plane, we do not consider spectrophotometric distances in this analysis. The extremely fine angular resolution provided by very long baseline interferometry (VLBI) is used to measure the parallaxes and proper motions of masers associated with high-mass star forming regions (e.g., Reid & Honma 2014). Several hundred maser parallax measurements have been made as part of the Bar and Spiral Structure Legacy (BeSSeL) Survey<sup>1</sup>, the Japanese VLBI Exploration of Radio Astronomy (VERA)<sup>2</sup>, and various European VLBI Network (EVN)<sup>3</sup> projects. The vast majority of Galactic H II regions, however, lack parallax measurements. We must therefore rely on kinematic techniques to derive the distances to nebulae without a geometric distance determination.

Of the 189 Galactic H II regions in our sample with accurate electron temperature determinations, 46 (24%) have a maser parallax measurement. As in Wenger et al. (2018), we derive the parallax distance and distance uncertainties by Monte Carlo resampling the measured parallax within its uncertainties. We generate 5000 samples of the parallax distance, then we fit a kernel density estimator (KDE) to the distance distribution to calculate a probability distribution function (PDF). The peak of the PDF is the derived parallax distance, and the width of the PDF characterizes the parallax distance uncertainty (see Wenger et al. 2018).

Kinematic distances are computed by measuring the line of sight velocity of an object and assuming that object follows some Galactic rotation model (GRM). We use the Wenger et al. (2018) Monte Carlo kinematic dis-

<sup>1</sup> <http://bessel.vlbi-astrometry.org/>

<sup>2</sup> <http://veraserver.mtk.nao.ac.jp/>

<sup>3</sup> <http://www.evlbi.org/>

tance method and the Reid et al. (2014) GRM to derive the kinematic distances to our sample of Galactic H II regions. This method computes the distances and distance uncertainties by resampling the observed LSR velocities, the solar motion parameters, which define the LSR, and the GRM parameters to determine the kinematic distance PDFs. Wenger et al. (2018) find that the Monte Carlo kinematic distances are reasonably accurate when compared to the parallax distances for a sample of 75 Galactic high-mass star forming regions. The median difference between the kinematic and parallax distances for these nebulae is 17% (0.42 kpc).

Within the Solar circle, there exists a kinematic distance ambiguity (KDA). An axisymmetric GRM yields the same LSR velocity at two distances, and additional information must be used to break this degeneracy. The *WISE* Catalog lists the KDA resolutions (KDAR) for a subset of the known Galactic H II regions. As in Wenger et al. (2018), we use the *WISE* Catalog KDARs for nebulae with LSR velocities farther than  $20 \text{ km s}^{-1}$  from the tangent point velocity. All nebulae within  $20 \text{ km s}^{-1}$  of the tangent point velocity are assigned to the tangent point distance.

Due to line of sight velocity crowding, kinematic distances are inaccurate in the direction of the Galactic center and anti-center. Following Wenger et al. (2018), we remove all kinematic distance nebulae located within the zones  $-15^\circ < \ell < 15^\circ$  and  $160^\circ < \ell < 200^\circ$ . After removing these nebulae, we are left with 121 Galactic H II regions with kinematic distances. Our final catalog contains 167 nebulae with accurate electron temperatures and either a parallax (46) or kinematic (121) distance. Table 6 lists the relevant distance parameters for each nebulae: the heliocentric distance  $d$ ; the Galactocentric radius,  $R$ ; the distance method (“P” for parallax and “K” for kinematic); and the maser parallax observation reference, if any. Nebulae with accurate electron temperatures, without a parallax measurement, and in the direction of the Galactic center/anti-center are also included in this table for completeness. These nebulae are, however, excluded from all subsequent analyses.

### 5.5. Metallicity Structure

H II region electron temperatures are a proxy for their nebular metallicities (e.g., Churchwell & Walmsley 1975). The H II region electron temperature structure across the Galactic disk thus reveals structure in metallicity. Shaver et al. (1983) derived an empirical relationship between H II region metallicities, determined using optical collisionally excited lines to derive the oxygen and hydrogen column densities, and electron tempera-

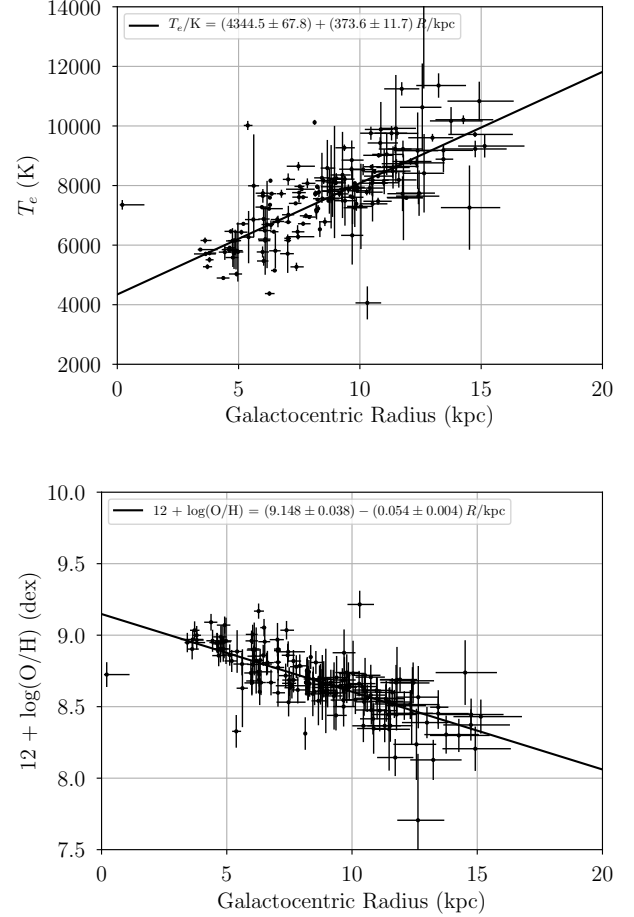


**Figure 6.** The nominal radial electron temperature (top) and metallicity (bottom) gradients. The abscissa error bars are the  $1\sigma$  uncertainties in the parallax or kinematic distances derived from our Monte Carlo distance analysis, and the ordinate error bars are the  $1\sigma$  uncertainties in the electron temperature or metallicity derived from the continuum and RRL uncertainties. The lines are the robust least squares linear model fits to the data as defined in the legends.

tures, determined from RRLs:

$$12 + \log_{10}(\text{O}/\text{H}) = (9.82 \pm 0.02) - (1.49 \pm 0.11) \frac{T_e}{10^4 \text{ K}} \quad (8)$$

where  $T_e$  is the nebular electron temperature.

We begin our investigation of Galactic chemical structure by measuring the radial electron temperature and metallicity gradients. Figure 6 shows the nebular electron temperature and metallicity gradients using the electron temperatures and Galactocentric radii from Table 6 and metallicities derived using Equation 8. The metallicity uncertainties are determined by propagating the electron temperature uncertainties through Equation 8. We use a robust least squares routine to fit a



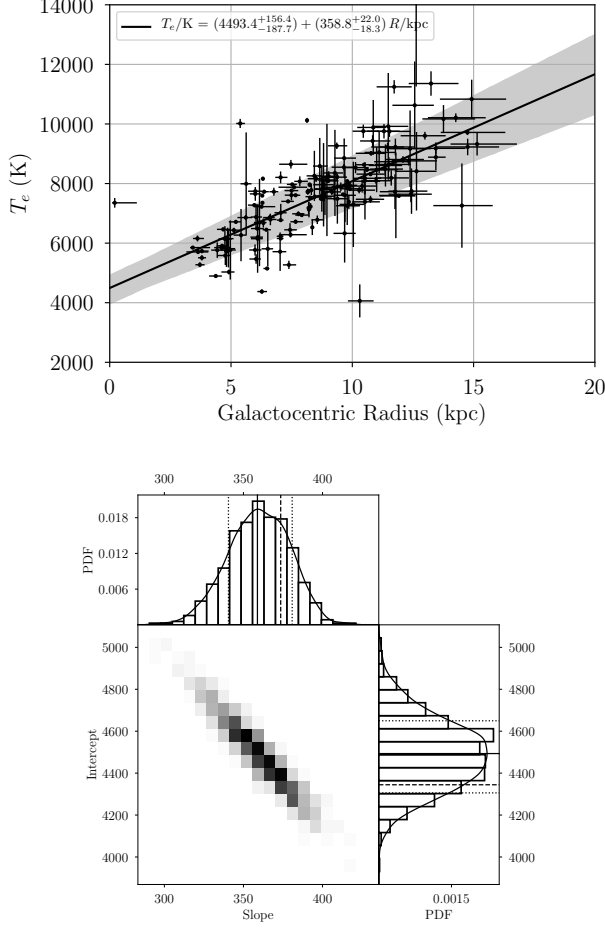


**Figure 7.** The most likely electron temperature gradient determined by Monte Carlo resampling the derived electron temperatures and Galactocentric radii. The top panel shows the data and the most likely linear model (black line) as defined in the legend. The error bars are the same as in Figure 6. The shaded region represents the range of fits from 1000 Monte Carlo realizations of the data. The bottom panel shows the covariances between the linear model parameters (slope, with units of  $\text{K kpc}^{-1}$ , and intercept, with units of K). The histograms are the PDFs of the Monte Carlo fit parameters, and the black curves are KDE fits to the PDFs. The solid lines are the peaks of the PDFs (the most likely fit parameters), and the dotted lines represent the  $1\sigma$  confidence intervals. The dashed lines are the nominal values of the fit parameters derived from the robust least squares fit to the data (i.e. without Monte Carlo resampling, as in Figure 6).

linear model to both distributions. The least squares fit is robust because we dampen the effect of outliers by minimizing a “soft” loss function,  $\rho(z) = \sqrt{1 + z^2} - 1$ , where  $z$  is the squared residuals. This routine does not consider the uncertainties of the data, because (1) there are uncertainties in both the dependent and independent variables, and (2) the Galactocentric radius uncer-

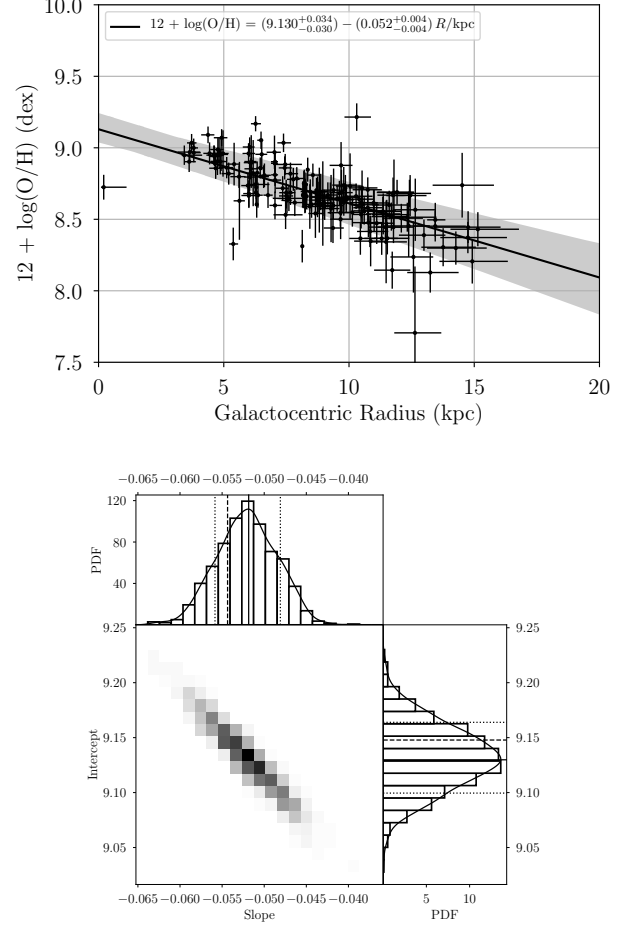


**Figure 8.** Same as Figure 7 for the radial metallicity gradient. The most likely linear model is defined in the legend. The covariance slope has units of  $\text{dex kpc}^{-1}$  and the intercept has units of dex.

tainties are asymmetric. Nonetheless, the best fit linear model to the nebular electron temperature distribution is  $T_e/\text{K} = (4345 \pm 68) + (374 \pm 12) R/\text{kpc}$ , and the best fit for the nebular metallicity distribution is  $12 + \log_{10}(\text{O}/\text{H}) = (9.148 \pm 0.038) - (0.054 \pm 0.004) R/\text{kpc}$ . Within the errors, these gradients are consistent with the gradients found by B15 using their “Best” distances and Green Bank sample:  $T_e/\text{K} \propto (402 \pm 33) R/\text{kpc}$  and  $12 + \log_{10}(\text{O}/\text{H}) \propto (-0.058 \pm 0.004) R/\text{kpc}$ .

A simple least squares fitting method cannot account for asymmetric uncertainties in both the abscissas (i.e., Galactocentric radii) and the ordinates (i.e., electron temperatures). Therefore, we estimate the true variance of the linear model by Monte Carlo resampling the data 1000 times. The electron temperatures are drawn from a Gaussian distribution centered at the derived electron temperature and with a width equal to the derived electron temperature uncertainty. The Galacto-

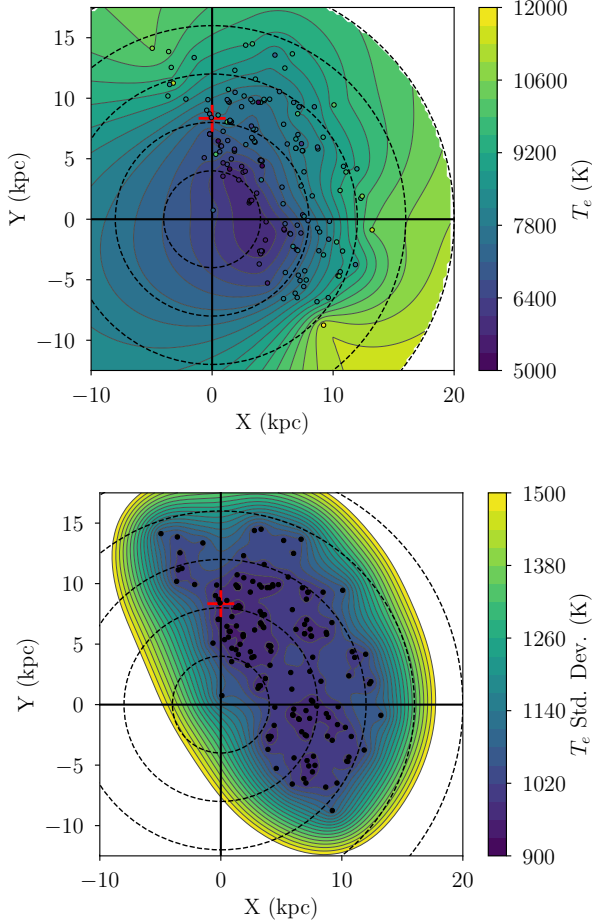


**Figure 9.** Kriging map of nebular electron temperatures. The top panel shows the Kriging interpolation in a face-on view of the Galactic disk. The points are the H II regions in our sample, colored by their derived electron temperatures. The bottom panel shows the Kriging standard deviation. The Galactic Center is located at the origin and the Sun is located at the red cross. The dashed circles are 4, 8, 12, 16, and 20 kpc in radius. White areas are outside  $R = 20$  kpc or have data values beyond the colorbar range.

centric radii are drawn from the parallax or kinematic distance PDFs. For each realization of the data, we fit a robust least squares linear model. Similar to the Monte Carlo kinematic distance method in Wenger et al. (2018), we estimate the most likely linear model parameters by fitting a KDE to the PDFs of each model parameter. The peak of this KDE is the most likely parameter, and the  $1\sigma$  confidence interval is derived from the bounds of the PDF such that (1) the PDF evaluated at the lower bound is equal to the PDF evaluated at the upper bound and (2) the integral of the normalized PDF between the bounds is 68.3%. Figures 7 and 8 show, respectively, the most likely linear model pa-

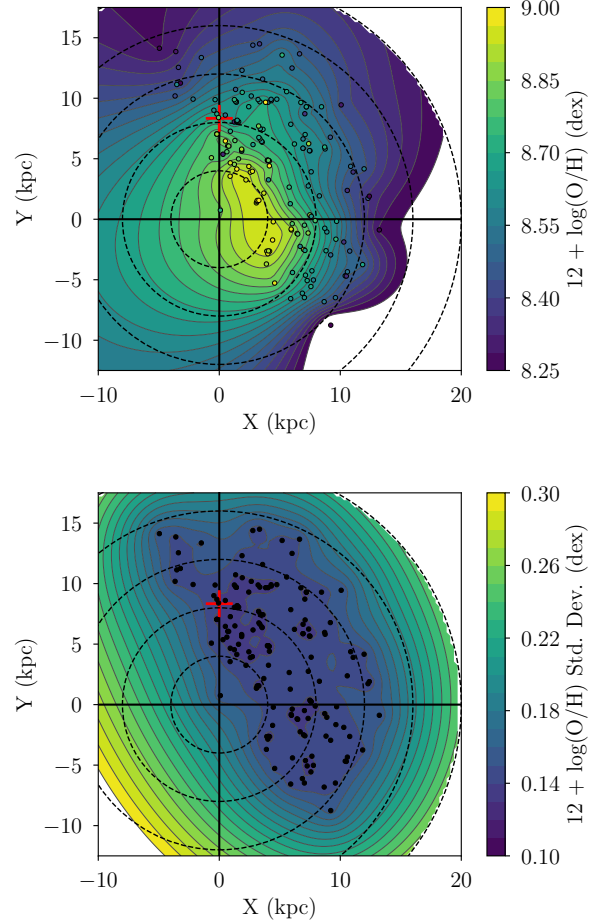


**Figure 10.** Same as Figure 9 for the nebular metallicities.

rameters derived from this Monte Carlo method and the covariance between the model parameters for the electron temperature and metallicity gradients. The most likely fits are  $T_e/\text{K} = 4493^{+156}_{-188} + 359^{+22}_{-18} R/\text{kpc}$  and  $12 + \log_{10}(\text{O}/\text{H}) = 9.130^{+0.034}_{-0.030} - 0.052^{+0.004}_{-0.004} R/\text{kpc}$ . These gradients are within  $1\sigma$  of the nominal least-squares values, and the asymmetric uncertainties are more accurate given the uncertainties in the derived electron temperatures and distances.

To visualize the variations in nebular electron temperature in the Galactic disk, we use Kriging to spatially interpolate between discrete nebulae (see also B15). The Kriging method computes the average semivariance of the data as a function of the spatial separation between the data points. The average semivariance is measured in many separation bins, known as “lags,” and the semivariogram (average semivariance as a function of lag) is fitted with a model. The expected value of the data at any position is derived from this semivariogram model (see Feigelson & Babu 2012).

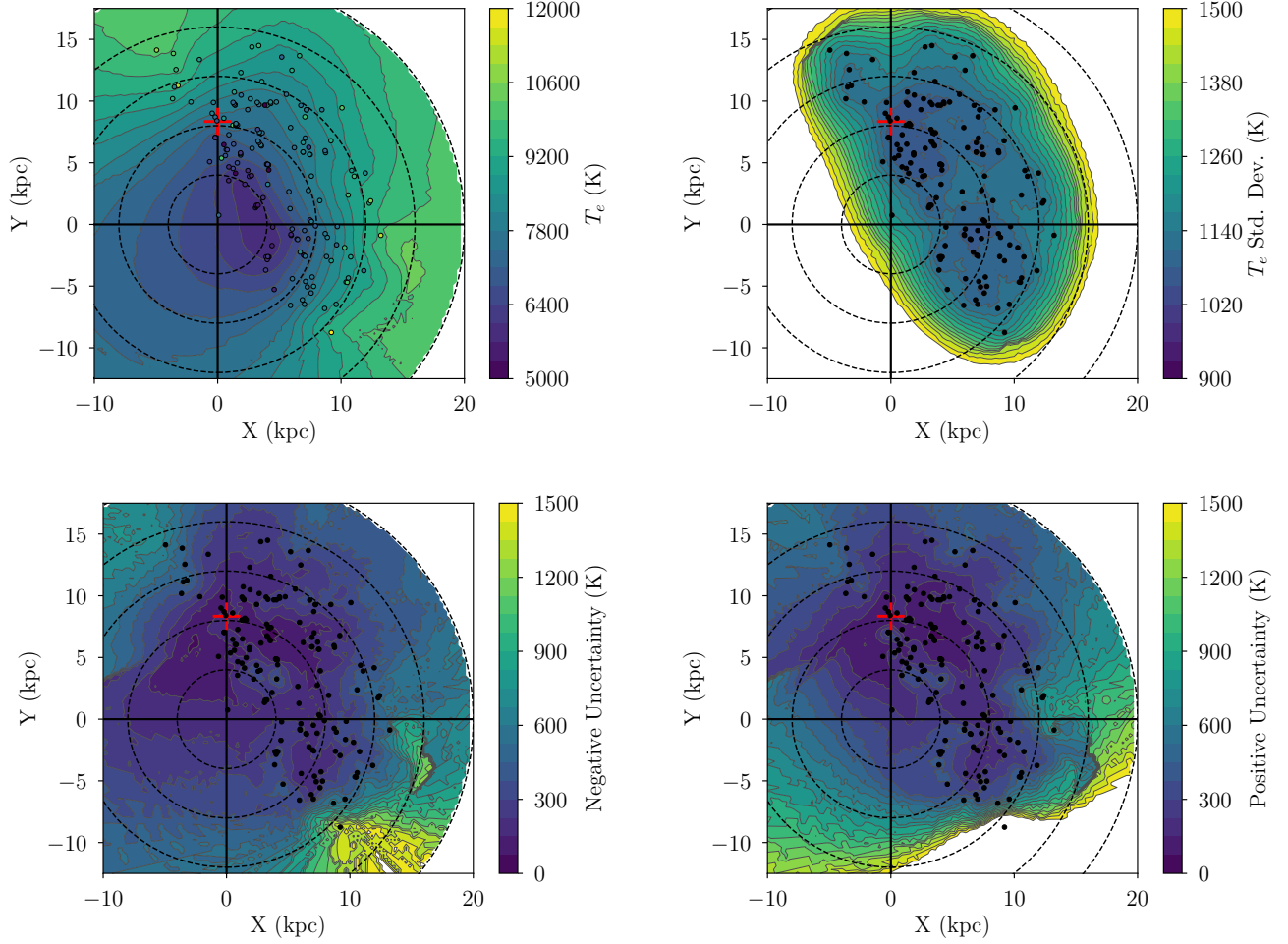


**Figure 11.** Most likely Kriging map of nebular electron temperatures determined by Monte Carlo resampling the derived electron temperatures and distances. Shown are the most likely Kriging interpolation values (top left), most likely Kriging standard deviation values (top right), lower  $1\sigma$  bounds (bottom left), and upper  $1\sigma$  bounds (bottom right) on the Kriging interpolation confidence intervals. The features in each plot are the same as in Figure 9.

We compute the nominal Kriging map of nebular electron temperatures using the Table 6 electron temperatures and distances. Figure 9 shows this electron temperature map, where we use a linear semivariogram model to interpolate between the discrete H II region positions. The top panel is the Kriging result and the bottom panel is the standard deviation of the Kriging interpolation. This standard deviation map characterizes the intrinsic scatter of the data across the Galactic disk. The H II region points are colored by their electron temperature to highlight the differences between the actual nebular electron temperature and the interpolated value at that position. Figure 10 shows the same Kriging results with a linear semivariogram model for the H II region metallicities. Qualitatively, these figures are similar to the electron temperature and metallicity maps in B15. It is clear from these figures that the radial

gradients have a strong dependence on Galactocentric azimuth.

These Kriging results consider neither the uncertainties in the nebular electron temperatures and metallicities nor the H II region distance uncertainties. We estimate the most likely Kriging map of nebular electron temperatures and metallicities using a Monte Carlo technique in the same way as we determined the most likely radial gradients. We Monte Carlo resample the data within their uncertainties 1000 times, and, for each realization of the data, we generate a Kriging map. At each pixel of the Kriging map, we construct a PDF of the interpolation values, fit a KDE, and locate the peak and bounds of the KDE. The peak is the most likely Kriging value at that position, and the bounds represent the  $1\sigma$  confidence interval, as before.

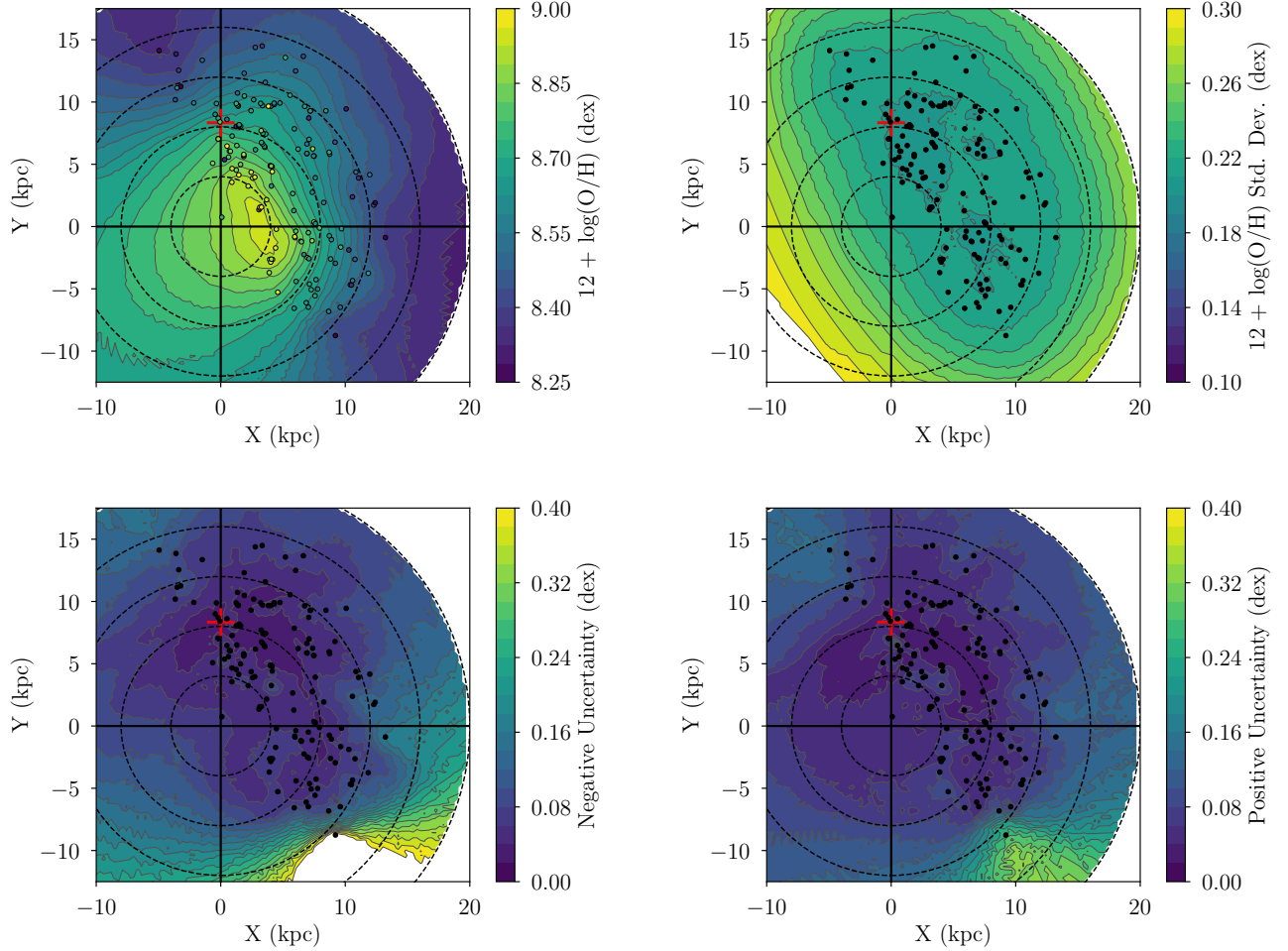


**Figure 12.** Same as Figure 11 for the nebular metallicities.

Figures 11 and 12 show the most likely Kriging interpolation map, most likely standard deviation map, and the upper and lower  $1\sigma$  confidence interval bound maps for the nebular electron temperatures and metallicities, respectively. The qualitative structure in the Monte Carlo Kriging interpolation maps is similar to that in the nominal Kriging maps, though the  $1\sigma$  confidence interval bound maps reveal where the Kriging interpolation is ill constrained. For most of the Galactic disk, the most likely Kriging values have  $1\sigma$  bounds  $\lesssim 500$  K in electron temperature and  $\lesssim 0.8$  dex in metallicity. These uncertainties are significantly less than the most likely Kriging standard deviations of  $\sim 1000$  K and  $\sim 0.25$  dex, which suggests that the intrinsic scatter in the nebular electron temperatures and metallicities exceeds the formal uncertainties.

## 6. DISCUSSION

The radial gradient is the most prominent feature in the metallicity structure of the Galactic disk. Our

Monte Carlo analysis of nebular metallicities results in a most likely H II region oxygen gradient of  $-0.052 \pm 0.004$  dex  $\text{kpc}^{-1}$ . Mollá et al. (2019a) list the oxygen abundance gradients derived from a variety of tracers (see their Table 2). The derived gradients range from about  $-0.05$  dex  $\text{kpc}^{-1}$  for H II regions and Cepheids to about  $0$  dex  $\text{kpc}^{-1}$  for old stellar populations. Our H II region oxygen gradient is consistent with those found using Cepheids (e.g.,  $-0.0529 \pm 0.0083$  dex  $\text{kpc}^{-1}$  from Korotin et al. 2014), other H II region samples (e.g.,  $-0.0525 \pm 0.0189$  dex  $\text{kpc}^{-1}$  from Fernández-Martín et al. 2017), and the Mollá et al. (2019a) binned H II region sample ( $-0.048 \pm 0.005$  dex  $\text{kpc}^{-1}$ ).

The large variance in the measured radial metallicity gradients of different tracers is likely due to two primary effects: (1) changes in the metallicity gradient with time and (2) dynamical evolution of stellar populations. The radial gradient as traced by stars is flatter at larger heights above the Galactic midplane (Cheng et al. 2012; Anders et al. 2017). There is evidence that

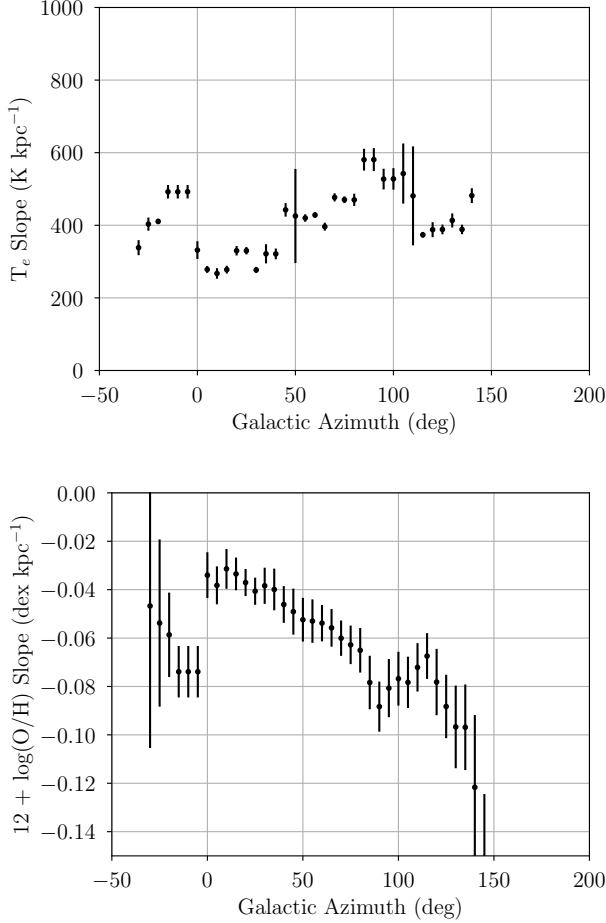


**Figure 13.** Nominal variations in the radial electron temperature (top) and metallicity (bottom) gradients as a function of Galactocentric azimuth. The Galaxy is divided into  $30^\circ$  bins spaced every  $5^\circ$  in Galactocentric azimuth. The points are the slopes of the robust least squares linear model fit to the data in each bin, and the error bars are the  $1\sigma$  uncertainties in the fitted slopes. Bins below  $\sim 0^\circ$  and above  $\sim 120^\circ$  are sparsely populated and their slopes are unreliable.

the stellar metallicity gradient also flattens in the inner galaxy (Hayden et al. 2015). These stellar populations are likely older, and thus their metallicity gradient reflects that of a younger Galaxy. Radial migration also plays an important role in stellar metallicity gradients (Sellwood & Binney 2002). The dynamical influence of non-axisymmetric features, like spiral arms and bars, can cause stars to migrate from their birth locations. Some studies have found that radial migration significantly affects the observed stellar metallicity gradients (e.g. Minchev et al. 2013, 2014), whereas others find only an increase in the stellar metallicity dispersion at all Galactocentric radii (e.g. Grand et al. 2014). These effects should have little impact on the H II region metal-

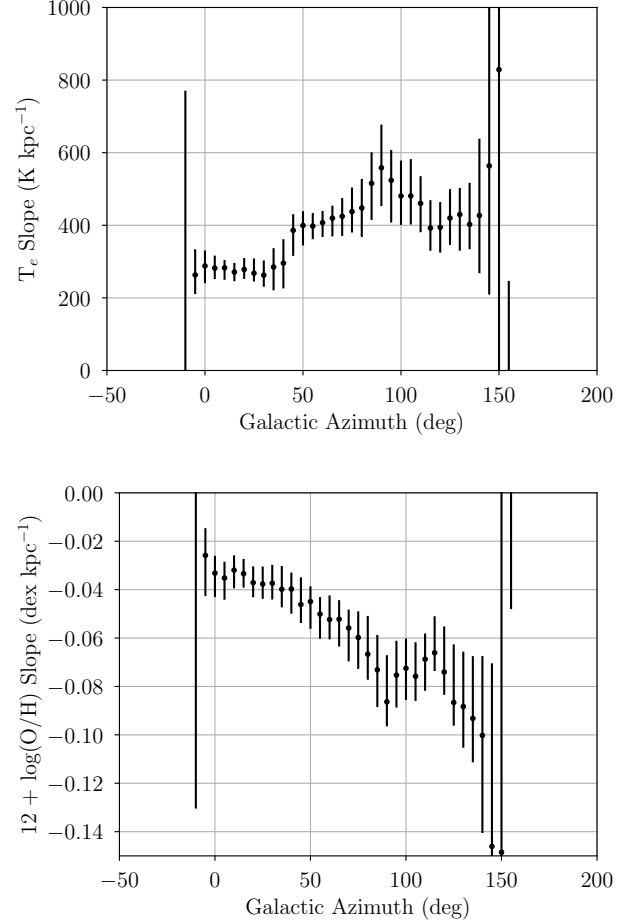


**Figure 14.** Same as Figure 13 for the most likely gradients derived from our Monte Carlo analysis. The error bars are the  $1\sigma$  confidence intervals on the most likely slopes.

licity gradient, because these nebulae are very young ( $\lesssim 10$  Myr) compared to the dynamical timescale of the Galaxy ( $\sim 250$  Myr). For example, Grand et al. (2014) use a chemodynamical simulation of a Milky Way-size galaxy to show that, over time, the gas metallicity maintains a low dispersion at all radii, whereas the dispersion of the stellar metallicity increases due to radial migration.

Evidence for azimuthal variations in the radial electron temperature and metallicity gradients has been found in the Milky Way (e.g., B15) and other galaxies (e.g., Ho et al. 2017). Here we expand upon the B15 analysis by using a larger sample of Galactic H II regions and a more accurate kinematic distance derivation technique. Evidence for azimuthal structure is already apparent in Figures 9–12, and here we test the statistical significance of these azimuthal variations.

To quantify the azimuthal structure in the nebular electron temperature and metallicity radial gradients,



we divide the Galaxy into azimuthal bins and compute the radial gradients within each bin. Following B15, we use bins of size  $30^\circ$  in Galactocentric azimuth centered every  $5^\circ$  from  $-50^\circ$  to  $200^\circ$ . Using the nebulae in each bin, we make a robust least squares linear fit to their derived electron temperatures and metallicities as a function of their Galactocentric radii. Figure 13 shows the best fit linear model slopes as a function of Galactocentric azimuth for the nebular electron temperature and metallicity gradients. Unlike B15, we do not exclude bins with only a few nebulae, nor those with nebulae spanning a small range of Galactocentric radii. The uncertainties in these bins will be correctly determined in the subsequent Monte Carlo analysis. In this simple least squares analysis, however, the best fit parameters and their uncertainties are unreliable in sparsely populated bins, such as those below  $\sim 0^\circ$  and above  $\sim 120^\circ$ . Nonetheless, we find a similar structure in the electron temperature and metallicity gradient slopes as found by B15. The electron temperature and metallicity slopes vary by a factor of 2 and 3, respectively, between Galactocentric azimuths of  $\sim 20^\circ$  and  $\sim 100^\circ$ . These variations are slightly less in magnitude than those found by B15, probably because of our much larger sample size near  $100^\circ$  in Galactocentric azimuth.

Multiple sources of uncertainty affect the apparent azimuthal variations shown in Figure 13. These sources include the derived electron temperature uncertainties and the distance uncertainties, which affect both the derived Galactocentric radii and azimuths of the nebulae. To better quantify these sources of uncertainty and to test the statistical significance of the apparent azimuthal variations, we perform yet another Monte Carlo analysis. We Monte Carlo resample the nebular electron temperatures, metallicities, and distances to generate 1000 realizations of the data. As before, the electron temperatures and metallicities are drawn from a Gaussian distribution, whereas the distances are drawn from the parallax or kinematic distance PDFs. For each realization of the data, we fit the radial gradients in each of the several Galactocentric azimuth bins. Finally, we fit a KDE to the linear model parameter PDFs to estimate the most likely parameters and their confidence intervals.

Figure 14 shows the most likely electron temperature and metallicity gradients from our Monte Carlo analysis. The most obvious difference between this and the nominal gradients in Figure 13 is the larger error bars. This Monte Carlo analysis properly accounts for the uncertainties in both the nebular electron temperatures/metallicities and distances, so these error bars more accurately reflect the uncertainties in

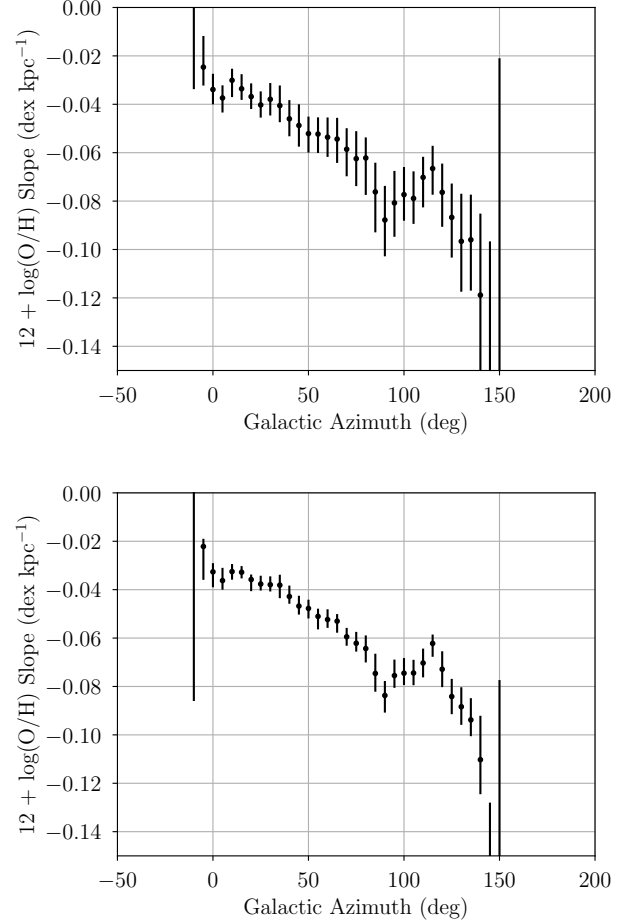


**Figure 15.** Same as the metallicity gradients in Figure 14, except we only Monte Carlo resample the derived metallicities (top) or distances (bottom).

the gradients within each azimuth bin. Despite the larger uncertainties, the azimuthal variations in the radial gradients remain statistically significant. The electron temperature gradient ranges from  $\sim 250$  K  $\text{kpc}^{-1}$  at  $\sim 30^\circ$  to  $\sim 500$  K  $\text{kpc}^{-1}$  at  $\sim 100^\circ$ , a factor of  $\sim 2$  increase, and the metallicity gradient ranges from about  $-0.035$  dex  $\text{kpc}^{-1}$  to about  $-0.075$  dex  $\text{kpc}^{-1}$  over the same range, a factor of  $\sim 2$  decrease.

The derived electron temperatures and metallicities are the largest source of error in the radial gradient determinations. Figure 15 shows the radial metallicity gradients in each Galactocentric azimuth bin where we Monte Carlo resample only the metallicity (top) or only the distances (bottom). The gradient uncertainties are a factor of  $\sim 2$  larger when we resample only the metallicities.

The azimuthal variations in the metallicity gradient are predicted by some simulations (Di Matteo et al. 2013; Grand et al. 2016). Grand et al. (2016), for exam-

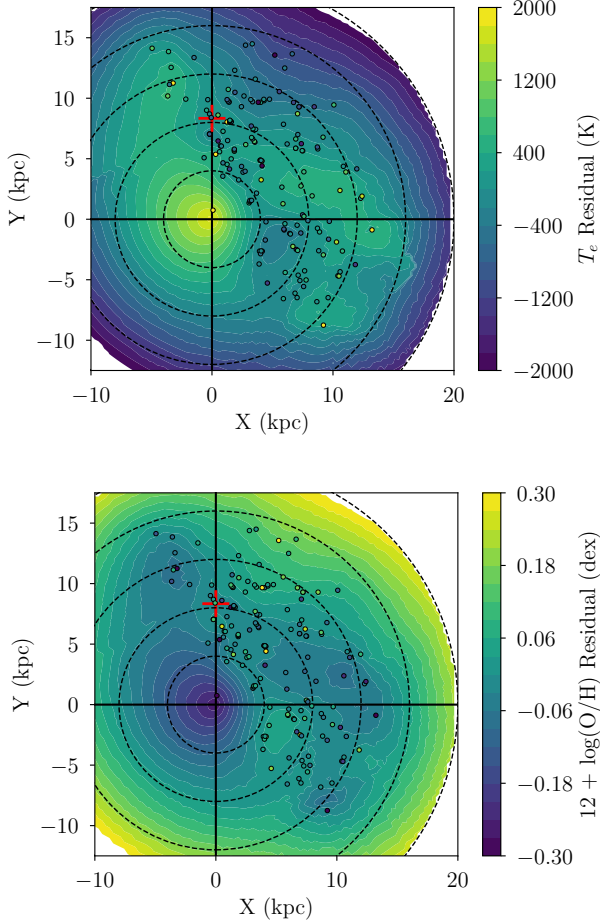


**Figure 16.** Most likely electron temperature (top) and metallicity (bottom) Kriging map residuals. The residuals are determined by subtracting the most likely gradient from the Monte Carlo Kriging maps. The features in each plot are the same as in Figure 9.

ple, find azimuthal metallicity structure in the young, thin disk stellar population of a cosmological simulation of a Milky Way analogue. The azimuthal variations are induced by the non-axisymmetric peculiar motions near spiral arms, which drives radial migration and a redistribution of metals. The magnitude of the azimuthal variations is  $\sim 0.1$  dex in their simulation. If such stellar azimuthal metallicity structure is persistent over long periods of time, the enrichment of the ISM by these stars might explain the observed azimuthal structure in the HII region metallicity distribution. Di Matteo et al. (2013) find a similar magnitude of variation in metallicities as traced by old stars in an N-body simulation. In Figure 16 we show the residuals of the electron temperature and metallicity Monte Carlo Kriging maps after subtracting the most likely radial gradients. Excluding the Galactic center and edge of the map, the magnitude

of variation in the metallicity residual map is  $\sim 0.1$  dex, which is consistent with the Grand et al. (2016) simulation. In the first quadrant, the residual structure between  $R \sim 6$  kpc and  $\sim 12$  kpc is qualitatively similar to the simulated residuals in Grand et al. (2016) and may be evidence for spiral arm induced radial migration in the Milky Way.

Recent two-dimensional chemical evolution models also predict azimuthal structure in the gas-phase oxygen abundance. For example, Spitoni et al. (2019) find that density fluctuations due to spiral arms produce oxygen abundance variations on the order of  $\sim 0.1$  dex, with the most azimuthal structure apparent at and beyond the corotation radius. The magnitude of these abundance fluctuations decreases with time as the model galaxy becomes well-mixed. This model does not consider stellar migration and enrichment, which, according to the Grand et al. (2016) simulation, are likely important factors. Mollá et al. (2019b) use a 2D chemical evolution code applied to a Milky Way analogue to conclude that spiral arms only marginally alter the azimuthal metallicity structure. Their model predicts present-day oxygen abundance variations of  $\sim 0.03$  dex increasing to  $\sim 0.1$  dex in the outer Galaxy. The oxygen abundance variations are more significant within 1–2 Gyr after spiral arms are introduced in their model.

The nebulae in this study cover only about half of the Galactic disk. The Southern HII Region Discovery Survey (SHRDS; Wenger et al. 2019) is finding hundreds of new HII regions in the third and fourth Galactic quadrants, and the SHRDS interferometric observations will allow for accurate electron temperature and metallicity derivations. In a future work, we will combine these northern sky nebulae with newly-discovered southern sky HII regions to create a map of HII region metallicities across the entire Galactic disk. We will use this map to test the chemodynamical evolution simulations by searching for evidence of metallicity structure associated with spiral arms, the Galactic bar, and/or other components of the Milky Way.

## 7. SUMMARY

We use the VLA to measure the  $\sim 8$ – $10$  GHz RRL and radio continuum flux densities of 82 Galactic HII regions. We derive the RRL-to-continuum brightness ratio, electron temperature, and metallicity of these nebulae. Including previous single dish observations, the catalog of Galactic HII regions with accurate electron temperatures and distances now contains 167 nebulae spanning Galactocentric radii 4 – 16 kpc and azimuths  $-20^\circ$  –  $140^\circ$ .

The distances to Galactic H II regions are the largest source of uncertainty in previous studies using these nebulae to trace Galactic metallicity structure (e.g., B15). Maser parallax distances have been determined for 46 of our nebulae. For the remainder, we use a novel Monte Carlo kinematic distance technique to determine distances (Wenger et al. 2018). Both the kinematic distances and distance uncertainties to the nebulae in our sample are more accurate than in the B15 study. In this work, the RRL-to-continuum brightness ratio uncertainties are about twice as important as the distance uncertainties.

Using a Monte Carlo analysis, we derive respectively the most likely Milky Way radial electron temperature and metallicity gradients as:  $T_e/\text{K} = 4493^{+156}_{-188} + 359^{+22}_{-18} R/\text{kpc}$  and  $12 + \log_{10}(\text{O}/\text{H}) = 9.130^{+0.034}_{-0.030} - 0.052^{+0.004}_{-0.004} R/\text{kpc}$ . This metallicity gradient is consistent with previous H II region studies (e.g., B15) and young stellar tracers, such as Cepheids (e.g., Korotin et al. 2014). We generate maps of the electron temperature and metallicity structure of the Galactic disk using a Monte Carlo Kriging analysis. These maps reveal significant azimuthal variations in the Galaxy’s metallicity structure. The radial metallicity gradient varies by a factor of  $\sim 2$  ( $\sim 0.04 \text{ dex kpc}^{-1}$ ) between Galactocentric azimuths of  $\sim 30^\circ$  and  $\sim 100^\circ$ . We find non-axisymmetric spatial metallicity variations on the order of  $\sim 0.1 \text{ dex}$ , which is consistent with the Grand et al. (2016) chemodynamical simulation. These variations may be evidence for radial migration and metal mixing induced by the Milky Way’s spiral arms.

The Southern H II Region Discovery Survey (Wenger et al. 2019) will add hundreds of nebulae with electron

temperature and metallicity derivations to the third and fourth Galactic quadrants. With H II region coverage across the entire Galactic disk, we will investigate the association between the Milky Way’s metallicity structure and the locations of spiral arms. Such structure is a test of chemodynamical simulations and can be directly compared to extragalactic systems.

#### ACKNOWLEDGMENTS

We thank the anonymous reviewer for their constructive feedback on this manuscript. T.V.W. is supported by the NSF through the Grote Reber Fellowship Program administered by Associated Universities, Inc./National Radio Astronomy Observatory, the D.N. Batten Foundation Fellowship from the Jefferson Scholars Foundation, the Mars Foundation Fellowship from the Achievement Rewards for College Scientists Foundation, and the Virginia Space Grant Consortium. L.D.A. is supported in part by NSF grant AST-1516021. T.M.B. is supported in part by NSF grant AST-1714688.

The National Radio Astronomy Observatory is a facility of the National Science Foundation operated under cooperative agreement by Associated Universities, Inc.

#### *Facility:* VLA

*Software:* Astropy (Astropy Collaboration et al. 2013), CASA (McMullin et al. 2007), KDUtills (Wenger et al. 2017), Matplotlib (Hunter 2007), NumPy & SciPy (van der Walt et al. 2011), PyKriging (Murphy 2014), Python (<https://www.python.org/>), WISP (Wenger 2018)

#### REFERENCES

- Altenhoff, W. J., Mezger, P. G., Wendker, H., & Westerhout, G. 1960, Veröffentlichungen der Universitäts-Sternwarte zu Bonn, 59, 48
- Anders, F., Chiappini, C., Rodrigues, T. S., et al. 2017, A&A, 597, A30
- Anderson, L. D., Armentrout, W. P., Johnstone, B. M., et al. 2015a, ApJS, 221, 26
- Anderson, L. D., Armentrout, W. P., Luisi, M., et al. 2018, ApJS, 234, 33
- Anderson, L. D., Bania, T. M., Balser, D. S., et al. 2014, ApJS, 212, 1
- Anderson, L. D., Bania, T. M., Balser, D. S., & Rood, R. T. 2011, ApJS, 194, 22
- . 2012, ApJ, 754, 62
- Anderson, L. D., Hough, L. A., Wenger, T. V., Bania, T. M., & Balser, D. S. 2015b, ApJ, 810, 42
- Ando, K., Nagayama, T., Omodaka, T., et al. 2011, PASJ, 63, 45
- Astropy Collaboration, Robitaille, T. P., Tollerud, E. J., et al. 2013, A&A, 558, A33
- Balser, D. S. 1995, PhD thesis, Boston University
- Balser, D. S., Anish Rosh, D., Jeyakumar, S., et al. 2016, ApJ, 816, 22
- Balser, D. S., Bania, T. M., Rood, R. T., & Wilson, T. L. 1999, ApJ, 510, 759
- Balser, D. S., Rood, R. T., Bania, T. M., & Anderson, L. D. 2011, ApJ, 738, 27
- Balser, D. S., Wenger, T. V., Anderson, L. D., & Bania, T. M. 2015, ApJ, 806, 199
- Bania, T. M., Anderson, L. D., & Balser, D. S. 2012, ApJ, 759, 96



- Bania, T. M., Anderson, L. D., Balser, D. S., & Rood, R. T. 2010, *ApJL*, 718, L106
- Bertrand, G. 2005, *Journal of Mathematical Imaging and Vision*, 22, 217
- Bihl, S., Johnston, K. G., Beuther, H., et al. 2016, *A&A*, 588, A97
- Bird, J. C., Kazantzidis, S., & Weinberg, D. H. 2012, *MNRAS*, 420, 913
- Bovy, J., Nidever, D. L., Rix, H.-W., et al. 2014, *ApJ*, 790, 127
- Brocklehurst, M., & Seaton, M. J. 1972, *MNRAS*, 157, 179
- Brunthaler, A., Reid, M. J., Menten, K. M., et al. 2009, *ApJ*, 693, 424
- Cheng, J. Y., Rockosi, C. M., Morrison, H. L., et al. 2012, *ApJ*, 746, 149
- Chiappini, C., Romano, D., & Matteucci, F. 2003, *MNRAS*, 339, 63
- Choi, Y. K., Hachisuka, K., Reid, M. J., et al. 2014, *ApJ*, 790, 99
- Churchwell, E., & Walmsley, C. M. 1975, *A&A*, 38, 451
- Di Matteo, P., Haywood, M., Combes, F., Semelin, B., & Snaith, O. N. 2013, *A&A*, 553, A102
- Feigelson, E. D., & Babu, G. J. 2012, *Modern Statistical Methods for Astronomy* (Cambridge University Press)
- Fernández-Martín, A., Pérez-Montero, E., Vílchez, J. M., & Mampaso, A. 2017, *A&A*, 597, A84
- Grand, R. J. J., Kawata, D., & Cropper, M. 2014, *MNRAS*, 439, 623
- Grand, R. J. J., Springel, V., Kawata, D., et al. 2016, *MNRAS*, 460, L94
- Hachisuka, K., Choi, Y. K., Reid, M. J., et al. 2015, *ApJ*, 800, 2
- Hachisuka, K., Brunthaler, A., Menten, K. M., et al. 2006, *ApJ*, 645, 337
- Hayden, M. R., Holtzman, J. A., Bovy, J., et al. 2014, *AJ*, 147, 116
- Hayden, M. R., Bovy, J., Holtzman, J. A., et al. 2015, *ApJ*, 808, 132
- Ho, I.-T., Seibert, M., Meidt, S. E., et al. 2017, *ApJ*, 846, 39
- Ho, I. T., Meidt, S. E., Kudritzki, R.-P., et al. 2018, *A&A*, 618, A64
- Honma, M., Bushimata, T., Choi, Y. K., et al. 2007, *PASJ*, 59, 889
- Hunter, J. D. 2007, *Computing In Science & Engineering*, 9, 90
- Immer, K., Reid, M. J., Menten, K. M., Brunthaler, A., & Dame, T. M. 2013, *A&A*, 553, A117
- Kardashev, N. S. 1959, *Soviet Astronomy*, 3, 813
- Kim, M. K., Hirota, T., Honma, M., et al. 2008, *PASJ*, 60, 991
- Korotin, S. A., Andrievsky, S. M., Luck, R. E., et al. 2014, *MNRAS*, 444, 3301
- Lockman, F. J. 1989, *ApJS*, 71, 469
- Lockman, F. J., Pisano, D. J., & Howard, G. J. 1996, *ApJ*, 472, 173
- Luck, R. E., Kovtyukh, V. V., & Andrievsky, S. M. 2006, *AJ*, 132, 902
- McMullin, J. P., Waters, B., Schiebel, D., Young, W., & Golap, K. 2007, in *ASPC, Vol. 376, Astronomical Data Analysis Software and Systems XVI*, ed. R. A. Shaw, F. Hill, & D. J. Bell, 127
- Menten, K. M., Reid, M. J., Forbrich, J., & Brunthaler, A. 2007, *A&A*, 474, 515
- Menzel, D. H. 1968, *Nature*, 218, 756
- Mezger, P. G., & Henderson, A. P. 1967, *ApJ*, 147, 471
- Mezger, P. G., & Hoglund, B. 1967, *ApJ*, 147, 490
- Minchev, I., Chiappini, C., & Martig, M. 2013, *A&A*, 558, A9
- . 2014, *A&A*, 572, A92
- Minchev, I., Anders, F., Recio-Blanco, A., et al. 2018, *MNRAS*, 481, 1645
- Mollá, M., Díaz, Á. I., Cavichia, O., et al. 2019a, *MNRAS*, 482, 3071
- Mollá, M., Wekesa, S., Cavichia, O., et al. 2019b, *MNRAS*, 490, 665
- Moscadelli, L., Reid, M. J., Menten, K. M., et al. 2009, *ApJ*, 693, 406
- Murphy, B. S. 2014, *American Geophysical Union Fall Meeting Abstracts*, H51K
- Oh, C. S., Kobayashi, H., Honma, M., et al. 2010, *PASJ*, 62, 101
- Oster, L. 1961, *AJ*, 66, 50
- Pedicelli, S., Bono, G., Lemasle, B., et al. 2009, *A&A*, 504, 81
- Quireza, C., Rood, R. T., Balser, D. S., & Bania, T. M. 2006a, *ApJS*, 165, 338
- Quireza, C., Rood, R. T., Bania, T. M., Balser, D. S., & Maciel, W. J. 2006b, *ApJ*, 653, 1226
- Reid, M. J., & Honma, M. 2014, *ARA&A*, 52, 339
- Reid, M. J., Menten, K. M., Brunthaler, A., et al. 2009a, *ApJ*, 693, 397
- Reid, M. J., Menten, K. M., Zheng, X. W., Brunthaler, A., & Xu, Y. 2009b, *ApJ*, 705, 1548
- Reid, M. J., Menten, K. M., Brunthaler, A., et al. 2014, *ApJ*, 783, 130
- Roman-Duval, J., Jackson, J. M., Heyer, M., et al. 2009, *ApJ*, 699, 1153
- Rygl, K. L. J., Brunthaler, A., Reid, M. J., et al. 2010, *A&A*, 511, A2

- Rygl, K. L. J., Brunthaler, A., Sanna, A., et al. 2012, *A&A*, 539, A79
- Sánchez-Menguiano, L., Sánchez, S. F., Pérez, I., et al. 2016, *A&A*, 587, A70
- . 2017, *A&A*, 603, A113
- Sandstrom, K. M., Peek, J. E. G., Bower, G. C., Bolatto, A. D., & Plambeck, R. L. 2007, *ApJ*, 667, 1161
- Sanna, A., Reid, M. J., Menten, K. M., et al. 2014, *ApJ*, 781, 108
- Sato, M., Reid, M. J., Brunthaler, A., & Menten, K. M. 2010, *ApJ*, 720, 1055
- Sato, M., Wu, Y. W., Immer, K., et al. 2014, *ApJ*, 793, 72
- Searle, L. 1971, *ApJ*, 168, 327
- Sellwood, J. A., & Binney, J. J. 2002, *MNRAS*, 336, 785
- Shaver, P. A., McGee, R. X., Newton, L. M., Danks, A. C., & Pottasch, S. R. 1983, *MNRAS*, 204, 53
- Snaith, O., Haywood, M., Di Matteo, P., et al. 2015, *A&A*, 578, A87
- Spitoni, E., Cescutti, G., Minchev, I., et al. 2019, *A&A*, 628, A38
- Urquhart, J. S., Hoare, M. G., Lumsden, S. L., et al. 2012, *MNRAS*, 420, 1656
- van der Walt, S., Colbert, S. C., & Varoquaux, G. 2011, *Computing in Science & Engineering*, 13, 22
- Wenger, T. 2018, *Astrophysics Source Code Library*, ascl:1812.001
- Wenger, T., Balser, D., Anderson, L., & Bania, T. 2017, *Astrophysics Source Code Library*, ascl:1712.001
- Wenger, T. V., Balser, D. S., Anderson, L. D., & Bania, T. M. 2018, *ApJ*, 856, 52
- Wenger, T. V., Dickey, J. M., Jordan, C. H., et al. 2019, *ApJS*, 240, 24
- Wu, Y. W., Xu, Y., Menten, K. M., Zheng, X. W., & Reid, M. J. 2012, in *IAU Symposium*, Vol. 287, *Cosmic Masers - from OH to H0*, ed. R. S. Booth, W. H. T. Vlemmings, & E. M. L. Humphreys, 425–426
- Wu, Y. W., Sato, M., Reid, M. J., et al. 2014, *A&A*, 566, A17
- Xu, Y., Moscadelli, L., Reid, M. J., et al. 2011, *ApJ*, 733, 25
- Xu, Y., Reid, M. J., Zheng, X. W., & Menten, K. M. 2006, *Science*, 311, 54
- Xu, Y., Li, J. J., Reid, M. J., et al. 2013, *ApJ*, 769, 15
- Zhang, B., Reid, M. J., Menten, K. M., et al. 2013, *ApJ*, 775, 79
- Zhang, B., Zheng, X. W., Reid, M. J., et al. 2009, *ApJ*, 693, 419
- Zhang, B., Moscadelli, L., Sato, M., et al. 2014, *ApJ*, 781, 89

## APPENDIX

## A. ELECTRON TEMPERATURE DERIVATIONS

Here we derive the relationship between the nebular electron temperature, hydrogen radio recombination line (RRL) brightness, and radio continuum brightness of an H II region. This derivation relies on several assumptions: (1) the nebula is homogeneous, isothermal, and in local thermodynamic equilibrium (LTE); (2) the nebula is optically thin in both radio continuum and RRL emission; (3) the nebula is composed solely of ionized hydrogen and singly-ionized helium; and (4) the RRL and continuum brightness are measured with the same telescope in the Rayleigh-Jeans limit.

The free-free radio continuum absorption coefficient of an isothermal plasma is

$$\frac{k_C(\nu)}{\text{pc}^{-1}} = 3.014 \times 10^{-2} \left( \frac{T_e}{\text{K}} \right)^{-1.5} \left( \frac{\nu}{\text{GHz}} \right)^{-2} \times \left[ \ln \left( 4.955 \times 10^{-2} \left( \frac{\nu}{\text{GHz}} \right)^{-1} \right) + 1.5 \ln \left( \frac{T_e}{\text{K}} \right) \right] \left( \frac{n_i n_e}{\text{cm}^{-6}} \right), \quad (\text{A1})$$

where  $T_e$  is the electron temperature,  $\nu$  is the observed frequency,  $n_i$  is the ion number density, and  $n_e$  is the electron number density (Oster 1961). Altenhoff et al. (1960) approximate the absorption coefficient as

$$\frac{k_C(\nu)}{\text{pc}^{-1}} \simeq 8.235 \times 10^{-2} \left( \frac{T_e}{\text{K}} \right)^{-1.35} \left( \frac{\nu}{\text{GHz}} \right)^{-2.1} \left( \frac{n_i n_e}{\text{cm}^{-6}} \right), \quad (\text{A2})$$

which is accurate within 10% for  $100 \text{ MHz} < \nu < 35 \text{ GHz}$  and  $5000 \text{ K} < T_e < 12000 \text{ K}$  (Mezger & Henderson 1967). The free-free optical depth is the integral of this absorption coefficient along the line of sight,  $\tau_C(\nu) = \int k_C(\nu) dl$ . In a homogeneous medium with line of sight depth  $l$ , the optical depth simplifies to  $\tau_C(\nu) = k_C l$ .

The LTE hydrogen RRL absorption coefficient for the transition from principle quantum state  $m$  to  $n$  is

$$k_L^*(\nu) = \left( \frac{h\nu_L}{kT_e} \right) \left( \frac{\pi e^2}{m_e c} \right) \left( \frac{h^2}{2\pi m_e kT_e} \right)^{3/2} n_e n_p \exp \left( \frac{\chi_n}{kT_e} \right) n^2 f_{nm} \phi_\nu(\nu), \quad (\text{A3})$$

where  $\nu_L$  is the RRL rest frequency,  $\chi_n$  is the energy required to ionize the atom from state  $n$ ,  $f_{nm}$  is the oscillator strength of the  $m$  to  $n$  transition,  $\phi_\nu(\nu)$  is the normalized line profile with inverse frequency units,  $n_p$  is the hydrogen number density,  $h$  is the Planck constant,  $k$  is the Boltzmann constant,  $e$  is the electron charge,  $m_e$  is the electron mass, and  $c$  is the speed of light (Brocklehurst & Seaton 1972; Balser 1995). The Rydberg formula determines the transition frequency between state  $m$  and  $n$ :

$$\nu_L = Z^2 R c (n^{-2} - m^{-2}), \quad (\text{A4})$$

where  $Z$  is the effective nuclear charge and  $R$  is the Rydberg constant. For hydrogen,  $Z = 1$  and  $R = R_\infty(1 - m_e/m_p)$ , where  $R_\infty$  is the Rydberg constant for an infinite mass and  $m_p$  is the proton mass. If we let  $\Delta n = m - n$ , then the hydrogen transition frequencies are

$$\nu_L = R_\infty c \left( 1 - \frac{m_e}{m_p} \right) \left[ n^{-2} - (n + \Delta n)^{-2} \right]. \quad (\text{A5})$$

For the low  $\Delta n$  transitions in the radio regime (e.g. H109 $\alpha$ ),  $\Delta n \ll n$  and

$$\nu_L \simeq 2R_\infty c \left( 1 - \frac{m_e}{m_p} \right) \frac{\Delta n}{n^3}. \quad (\text{A6})$$

Substituting these frequencies into Equation A3, and assuming that we are observing in the Rayleigh-Jeans limit  $\chi_n \ll kT_e$ , the LTE RRL absorption coefficient becomes

$$k_L^*(\nu) = 2R_\infty c \left( \frac{h}{kT_e} \right) \left( 1 - \frac{m_e}{m_p} \right) \left( \frac{\pi e^2}{m_e c} \right) \left( \frac{h^2}{2\pi m_e kT_e} \right)^{3/2} n_e n_p \frac{\Delta n}{n} f_{nm} \phi_\nu(\nu). \quad (\text{A7})$$

Evaluating the constants and moving to astrophysically relevant units, this equation becomes

$$\frac{k_L^*(\nu)}{\text{pc}^{-1}} \simeq 1.070 \times 10^7 \left( \frac{T_e}{\text{K}} \right)^{-2.5} \left( \frac{n_e n_p}{\text{cm}^{-6}} \right) \frac{\Delta n}{n} f_{nm} \left( \frac{\phi_\nu(\nu)}{\text{Hz}^{-1}} \right). \quad (\text{A8})$$

The RRL optical depth is the integral of this absorption coefficient along the line of sight, which is  $\tau_L^*(\nu) = k_L^*(\nu)l$  for a homogeneous medium.

In an optically thin medium in LTE, the specific intensity of some emission with optical depth  $\tau$  is  $I_\nu \simeq B_\nu(T)\tau$ , where  $B_\nu(T)$  is the Planck function at some temperature  $T$ . Assuming the RRL and continuum emission originate in the same volume of homogeneous, isothermal gas with electron temperature,  $T_e$ , the RRL-to-continuum specific intensity ratio at  $\nu_L$  is

$$\begin{aligned} \frac{I_L(\nu_L)}{I_C(\nu_L)} &= \frac{\tau_L^*(\nu_L)}{\tau_C(\nu_L)} = \frac{k_L^*(\nu_L)}{k_C(\nu_L)} \\ \frac{I_L(\nu_L)}{I_C(\nu_L)} &= 1.300 \times 10^8 \left( \frac{T_e}{\text{K}} \right)^{-1.15} \left( \frac{\nu_L}{\text{GHz}} \right)^{2.1} \frac{n_p}{n_i} \frac{\Delta n}{n} f_{nm} \left( \frac{\phi_\nu(\nu_L)}{\text{Hz}^{-1}} \right). \end{aligned} \quad (\text{A9})$$

For a Gaussian line profile with full-width half-maximum line width  $\Delta\nu$ ,

$$\phi_\nu(\nu) = \frac{2}{\Delta\nu} \left( \frac{\ln 2}{\pi} \right)^{1/2} \exp \left[ -4 \ln 2 \frac{(\nu - \nu_L)^2}{\Delta\nu^2} \right] \quad (\text{A10})$$

and

$$\phi_\nu(\nu_L) = \frac{2}{\Delta\nu} \left( \frac{\ln 2}{\pi} \right)^{1/2}. \quad (\text{A11})$$

Using Equation A11 in Equation A9, we find

$$\frac{I_L(\nu_L)}{I_C(\nu_L)} = 1.221 \times 10^8 \frac{\Delta n}{n} \left( \frac{T_e}{\text{K}} \right)^{-1.15} \left( \frac{\nu_L}{\text{GHz}} \right)^{2.1} \left( \frac{\Delta\nu}{\text{Hz}} \right)^{-1} \frac{n_p}{n_i} f_{nm}. \quad (\text{A12})$$

If the nebulae is composed of only hydrogen and singly ionized helium, then

$$\frac{n_p}{n_i} = \frac{n_p}{n_p + n_{\text{He}^+}} = \left( 1 + \frac{n_{\text{He}^+}}{n_p} \right)^{-1} = (1 + y)^{-1}, \quad (\text{A13})$$

where  $n_{\text{He}^+}$  is the singly ionized helium number density and  $y \equiv n_{\text{He}^+}/n_p$  is the ratio of singly ionized helium to hydrogen by number. We use the Doppler equation to convert the FWHM line width from frequency to velocity units:

$$\frac{\Delta\nu}{\text{Hz}} = \frac{\Delta V}{c} \left( \frac{\nu_L}{\text{Hz}} \right) = 3.336 \times 10^3 \left( \frac{\nu_L}{\text{GHz}} \right) \left( \frac{\Delta V}{\text{km s}^{-1}} \right) \quad (\text{A14})$$

where  $\Delta V$  is the FWHM line width in velocity units. The RRL-to-continuum specific intensity ratio at  $\nu_L$  is thus

$$\frac{I_L(\nu_L)}{I_C(\nu_L)} = 3.661 \times 10^4 \left( \frac{T_e}{\text{K}} \right)^{-1.15} \left( \frac{\nu_L}{\text{GHz}} \right)^{1.1} \left( \frac{\Delta V}{\text{km s}^{-1}} \right)^{-1} (1 + y)^{-1} \frac{\Delta n}{n} f_{nm}. \quad (\text{A15})$$

The expression  $(f_{nm}\Delta n/n)$  is not a strong function of  $n$  for  $\Delta n = 1$  hydrogen RRLs. For example,  $(f_{nm}\Delta n/n) = 0.19435, 0.19395, \text{ and } 0.19363$  for  $\Delta n = 1$  and  $n = 80, 90, \text{ and } 100$ , respectively, using the oscillator strengths from [Menzel \(1968\)](#). This variation is less than 0.3% across these Hn $\alpha$  transitions, so we adopt the H90 $\alpha$  oscillator strength to simplify the RRL-to-continuum specific intensity equation as

$$\frac{I_L(\nu_L)}{I_C(\nu_L)} = 7.100 \times 10^3 \left( \frac{T_e}{\text{K}} \right)^{-1.15} \left( \frac{\nu_L}{\text{GHz}} \right)^{1.1} \left( \frac{\Delta V}{\text{km s}^{-1}} \right)^{-1} (1 + y)^{-1}. \quad (\text{A16})$$

Solving for the electron temperature, we find

$$\frac{T_e}{\text{K}} = \left[ 7.100 \times 10^3 \left( \frac{I_C(\nu_L)}{I_L(\nu_L)} \right) \left( \frac{\nu_L}{\text{GHz}} \right)^{1.1} \left( \frac{\Delta V}{\text{km s}^{-1}} \right)^{-1} (1 + y)^{-1} \right]^{0.87} \quad (\text{A17})$$

A.1. *Single Dish Observations*

Single dish telescopes measure intensity in units of antenna temperature,  $T_A$ . In the absence of atmospheric attenuation, the antenna temperature is related to the brightness temperature distribution,  $T_B(\theta)$ , by

$$T_A = \frac{\eta_b}{\Omega_b} 2\pi \int_0^\infty f(\theta) T_B(\theta) \sin \theta d\theta, \quad (\text{A18})$$

where  $\eta_b$  is the telescope beam efficiency,  $\Omega_b$  is the telescope main beam solid angle,  $f(\theta)$  is the telescope beam pattern, and the integral is the convolution of the source brightness distribution with the telescope beam (Mezger & Henderson 1967). For a Gaussian beam with half-power beam width (HPBW)  $\theta_b$ , the beam pattern is  $f(\theta) = \exp[-4 \ln(2) \theta^2 / \theta_b^2]$  and the beam solid angle is  $\Omega_b = 2\pi \int_0^\infty f(\theta) \theta d\theta = \pi \theta_b^2 / (4 \ln 2)$ . Similarly, if the source brightness distribution is Gaussian with amplitude  $T_B$  and half-power width  $\theta_s$ , then the source brightness temperature distribution is  $T_B(\theta) = T_B \exp[-4 \ln(2) \theta^2 / \theta_s^2]$ . In astronomy,  $\theta$  is typically very small,  $\sin \theta \simeq \theta$ , and the integral in Equation A18 is

$$\begin{aligned} \int_0^\infty f(\theta) T_B(\theta) \sin \theta d\theta &\simeq \int_0^\infty f(\theta) T_B(\theta) \theta d\theta \\ &= T_B \int_0^\infty \exp \left[ -4 \ln(2) \theta^2 \left( \frac{\theta_s^2 + \theta_b^2}{\theta_s^2 \theta_b^2} \right) \right] \theta d\theta \\ &= \frac{T_B}{8 \ln 2} \left( \frac{\theta_s^2 \theta_b^2}{\theta_s^2 + \theta_b^2} \right), \end{aligned} \quad (\text{A19})$$

where we use  $\int_0^\infty x \exp(-ax^2) dx = 1/(2a)$ . The antenna temperature is thus

$$T_A = \eta_b T_B \left( \frac{\theta_s^2}{\theta_s^2 + \theta_b^2} \right). \quad (\text{A20})$$

For a resolved source,  $\theta_s \gg \theta_b$  and  $T_A \simeq \eta_b T_B$ . For an unresolved source,  $\theta_s \ll \theta_b$  and  $T_A \simeq \eta_b T_B (\theta_s^2 / \theta_b^2)$ .

Brightness temperature is defined as

$$T_B \equiv \frac{c^2}{2k\nu^2} I_\nu, \quad (\text{A21})$$

where  $I_\nu$  is the specific intensity. For an optically thin medium,  $I_\nu = B_\nu(T)\tau$ , where  $T$  is the blackbody temperature of the emission and  $\tau$  is the optical depth. In the Rayleigh-Jeans limit, the brightness temperature is simply

$$T_B = \frac{c^2}{2k\nu^2} B_\nu(T)\tau \simeq T\tau. \quad (\text{A22})$$

Substituting Equation A22 into Equation A20, we find

$$T_A = \eta_b T \tau \left( \frac{\theta_s^2}{\theta_s^2 + \theta_b^2} \right). \quad (\text{A23})$$

If the RRL and continuum antenna temperatures are measured with the same telescope and at the same frequency, and if both sources of emission originate from the same volume of homogeneous and isothermal gas with electron temperature  $T_e$ , Equation A16 is trivially

$$\frac{T_L(\nu_L)}{T_C(\nu_L)} = 7.100 \times 10^3 \left( \frac{T_e}{\text{K}} \right)^{-1.15} \left( \frac{\nu_L}{\text{GHz}} \right)^{1.1} \left( \frac{\Delta V}{\text{km s}^{-1}} \right)^{-1} (1+y)^{-1}, \quad (\text{A24})$$

where  $T_C(\nu_L)$  and  $T_L(\nu_L)$  are the continuum and RRL antenna temperatures measured at the RRL frequency  $\nu_L$ , respectively. Equation A17 becomes

$$\frac{T_e}{\text{K}} \simeq \left[ 7.100 \times 10^3 \left( \frac{T_C(\nu_L)}{T_L(\nu_L)} \right) \left( \frac{\nu_L}{\text{GHz}} \right)^{1.1} \left( \frac{\Delta V}{\text{km s}^{-1}} \right)^{-1} (1+y)^{-1} \right]^{0.87}. \quad (\text{A25})$$

### A.2. Averaging Single Dish RRLs

In Galactic H II region surveys, we average multiple RRL transitions to increase the RRL signal-to-noise ratio. Each RRL transition is an independent measurement of the nebular electron temperature, so the electron temperature derived from many RRL-to-continuum antenna temperature measurements is

$$\frac{T_e}{\text{K}} = \left[ 7.100 \times 10^3 \left( \frac{\Delta V}{\text{km s}^{-1}} \right)^{-1} (1+y)^{-1} \right]^{0.87} \left\langle \left[ \left( \frac{T_C(\nu_L)}{T_L(\nu_L)} \right) \left( \frac{\nu_L}{\text{GHz}} \right)^{1.1} \right]^{0.87} \right\rangle, \quad (\text{A26})$$

assuming that adjacent RRL transitions have similar FWHM line widths in velocity units (e.g., [Balser et al. 2011](#)). Previous single dish RRL studies have used different strategies for averaging RRL transitions. [Balser et al. \(2011\)](#) and [Balser et al. \(2015\)](#), for example, scale each RRL antenna temperature to account for the variations in telescope beam size with frequency, then average the re-scaled RRL spectra. They measure the continuum antenna temperature at one frequency within the RRL frequency range, then take the ratio of the average RRL antenna temperatures to this continuum temperature. This strategy is an approximation to Equation A26.

Here we compute the difference between the true electron temperature and the [Balser et al. \(2011\)](#) and [Balser et al. \(2015\)](#) approximation using multiple RRL transitions. From Equation A26, the factor we need to derive is

$$\begin{aligned} X_{\text{true}} &= \left\langle \left[ \left( \frac{T_C(\nu_L)}{T_L(\nu_L)} \right) \left( \frac{\nu_L}{\text{GHz}} \right)^{1.1} \right]^{0.87} \right\rangle \\ &= \left( \frac{T_e}{\text{K}} \right) \left[ 7.100 \times 10^3 \left( \frac{\Delta V}{\text{km s}^{-1}} \right)^{-1} (1+y)^{-1} \right]^{-0.87}, \end{aligned} \quad (\text{A27})$$

where  $T_e \propto X_{\text{true}}$  and  $X_{\text{true}}$  is the only variable in Equation A26 that depends on the RRL transition. [Balser et al. \(2011\)](#) and [Balser et al. \(2015\)](#) approximate this factor as

$$X = \left[ \left( \frac{T_C(\nu_C)}{\langle T_L^*(\nu_L) \rangle} \right) \left( \frac{\langle \nu_L \rangle}{\text{GHz}} \right)^{1.1} \right]^{0.87}, \quad (\text{A28})$$

where  $\nu_C$  is the observed continuum frequency and  $T_L^*(\nu_L)$  is the RRL antenna temperature corrected for the variation of telescope beam size with frequency. They re-scale the observed RRL antenna temperature,  $T_L(\nu_L)$ , using

$$T_L^*(\nu_L) = T_L(\nu_L) \left( \frac{\theta_s^2 + \theta_b^2}{\theta_s^2 + (\theta_b^*)^2} \right), \quad (\text{A29})$$

where  $\theta_b$  is the HPBW at  $\nu_L$ , and  $\theta_b^*$  is the HPBW at  $\nu_C$ , and  $\theta_s$  is the half-power width of the source. The observed source brightness distribution is the convolution of the actual source brightness and the telescope beam. With the assumption that the telescope beam and source brightness distribution are Gaussian, the convolution is also a Gaussian with half-power width  $\theta_o^2 = \theta_s^2 + \theta_b^2$ . [Balser et al. \(2011\)](#) and [Balser et al. \(2015\)](#) measure the source half-power width at  $\nu_C$ , which is  $(\theta_o^*)^2 = \theta_s^2 + (\theta_b^*)^2$ . The true, deconvolved source size is  $\theta_s^2 = (\theta_o^*)^2 - (\theta_b^*)^2$ , and the re-scaled antenna temperature in terms of observables is

$$T_L^*(\nu_L) = T_L(\nu_L) \left( \frac{(\theta_o^*)^2 - (\theta_b^*)^2 + \theta_b^2}{(\theta_o^*)^2} \right). \quad (\text{A30})$$

For a point source,  $(\theta_o^*)^2 \simeq (\theta_b^*)^2$  and  $T_L^*(\nu_L) \simeq T_L(\nu_L)[\theta_b^2/(\theta_b^*)^2]$ , whereas if the source is very resolved,  $(\theta_o^*)^2 \gg (\theta_b^*)^2$  and  $T_L^*(\nu_L) \simeq T_L(\nu_L)$ .

Using Equations A8, A11, and A14, the line center LTE optical depth of the  $i$ th RRL transition is

$$\tau_{L,i}^*(\nu_{L,i}) = 584.47 \left( \frac{T_e}{\text{K}} \right)^{-2.5} \left( \frac{n_e n_p}{\text{cm}^{-6}} \right) \left( \frac{\nu_{L,i}}{\text{GHz}} \right)^{-1} \left( \frac{\Delta V}{\text{km s}^{-1}} \right)^{-1} \left( \frac{l}{\text{pc}} \right), \quad (\text{A31})$$

where we have assumed  $\tau_{L,i}^* = \int k_{L,i}^* dl = k_{L,i}^* l$  for a homogeneous medium with an LTE absorption coefficient  $k_{L,i}^*$  and a line of sight depth  $l$ . The antenna temperature of this transition is

$$\begin{aligned} T_{L,i}(\nu_{L,i}) &= T_e \tau_{L,i}^* (\nu_{L,i}) \eta_b \left( \frac{\theta_s^2}{\theta_s^2 + \theta_b^2} \right) \\ &= 584.47 \eta_b \left( \frac{T_e}{\text{K}} \right)^{-1.5} \left( \frac{n_e n_p}{\text{cm}^{-6}} \right) \left( \frac{\nu_{L,i}}{\text{GHz}} \right)^{-1} \left( \frac{\Delta V}{\text{km s}^{-1}} \right)^{-1} \left( \frac{l}{\text{pc}} \right) \\ &\quad \times \left( \frac{\theta_s^2}{\theta_s^2 + \theta_b^2} \right) \end{aligned} \quad (\text{A32})$$

and the re-scaled RRL antenna temperature is

$$\begin{aligned} T_{L,i}^*(\nu_{L,i}) &= 584.47 \eta_b \left( \frac{T_e}{\text{K}} \right)^{-1.5} \left( \frac{n_e n_p}{\text{cm}^{-6}} \right) \left( \frac{\nu_{L,i}}{\text{GHz}} \right)^{-1} \left( \frac{\Delta V}{\text{km s}^{-1}} \right)^{-1} \left( \frac{l}{\text{pc}} \right) \\ &\quad \times \left( \frac{\theta_s^2}{\theta_s^2 + (\theta_b^*)^2} \right). \end{aligned} \quad (\text{A33})$$

The average re-scaled RRL antenna temperature of several RRL transitions is

$$\begin{aligned} \langle T_L^*(\nu_L) \rangle &= 584.47 \eta_b \left( \frac{T_e}{\text{K}} \right)^{-1.5} \left( \frac{n_e n_p}{\text{cm}^{-6}} \right) \left( \frac{\Delta V}{\text{km s}^{-1}} \right)^{-1} \left( \frac{l}{\text{pc}} \right) \\ &\quad \times \left\langle \left( \frac{\nu_L}{\text{GHz}} \right)^{-1} \left( \frac{\theta_s^2}{\theta_s^2 + (\theta_b^*)^2} \right) \right\rangle \end{aligned} \quad (\text{A34})$$

assuming that the RRLs have similar FWHM line widths in velocity units.

From Equation A2, the continuum optical depth at frequency  $\nu_C$  is

$$\tau_C(\nu_C) = 8.235 \times 10^{-2} \left( \frac{T_e}{\text{K}} \right)^{-1.35} \left( \frac{\nu_C}{\text{GHz}} \right)^{-2.1} \left( \frac{n_i n_e}{\text{cm}^{-6}} \right) \left( \frac{l}{\text{pc}} \right), \quad (\text{A35})$$

where, again, we have assumed that the medium is homogeneous. The continuum antenna temperature is

$$\begin{aligned} T_C(\nu_C) &= T_e \tau_C(\nu_C) \eta_b \left( \frac{\theta_s^2}{\theta_s^2 + (\theta_b^*)^2} \right) \\ &= 8.235 \times 10^{-2} \eta_b \left( \frac{T_e}{\text{K}} \right)^{-0.35} \left( \frac{\nu_C}{\text{GHz}} \right)^{-2.1} \left( \frac{n_i n_e}{\text{cm}^{-6}} \right) \left( \frac{l}{\text{pc}} \right) \\ &\quad \times \left( \frac{\theta_s}{\theta_s + (\theta_b^*)^2} \right). \end{aligned} \quad (\text{A36})$$

Substituting Equations A34 and A36 into the Balser et al. (2011) and Balser et al. (2015) approximation of  $X$ , we find

$$\begin{aligned} X &= \left( \frac{T_e}{\text{K}} \right) \left[ 1.409 \times 10^{-4} \left( \frac{\nu_C}{\text{GHz}} \right)^{-2.1} \left( \frac{\Delta V}{\text{km s}^{-1}} \right) (1 + y) \left( \frac{\langle \nu_L \rangle}{\text{GHz}} \right)^{1.1} \right]^{0.87} \\ &\quad \times \left\langle \left( \frac{\nu_L}{\text{GHz}} \right)^{-1} \right\rangle^{-0.87}. \end{aligned} \quad (\text{A37})$$

The ratio of the  $X$  approximation and  $X_{\text{true}}$  is

$$\frac{X}{X_{\text{true}}} = \left( \frac{\nu_C}{\text{GHz}} \right)^{-1.827} \left( \frac{\langle \nu_L \rangle}{\text{GHz}} \right)^{0.957} \left\langle \left( \frac{\nu_L}{\text{GHz}} \right)^{-1} \right\rangle^{-0.87}. \quad (\text{A38})$$

As a sanity check on this expression, if the RRL and continuum antenna temperatures are measured at only one RRL frequency, then  $\nu_C = \nu_L = \langle \nu_L \rangle$  and this ratio is unity. Balser et al. (2015) measured the continuum antenna

temperature at  $\nu_C = 8.556$  GHz and the RRL antenna temperature for 6 H $n\alpha$  transitions (H87 $\alpha$  to H93 $\alpha$ , excluding H90 $\alpha$ ). The average RRL frequency is  $\langle\nu_L\rangle = 8.903$  GHz, but Balser et al. (2015) use  $\langle\nu_L\rangle = 9$  GHz. With these values, the  $X$  ratio is

$$\frac{X}{X_{\text{true}}} = 1.057. \quad (\text{A39})$$

Therefore, Balser et al. (2015) and other studies that average the same RRL transitions and observe the same continuum frequency will overestimate the derived electron temperatures by  $\sim 5.7\%$ .

Quireza et al. (2006a) and Quireza et al. (2006b) use different RRL transitions and calibration strategies to derive electron temperatures. In their C II survey, they observe H91 $\alpha$  and H92 $\alpha$ . They assume both transitions have the same antenna temperature in the bright H II region W3, and they use this assumption to calibrate H92 $\alpha$  relative to H91 $\alpha$ . From Equation A32, this calibration factor is

$$\frac{T_{L, \text{H91}\alpha}}{T_{L, \text{H92}\alpha}} = \left( \frac{\nu_{\text{H92}\alpha}}{\nu_{\text{H91}\alpha}} \right) \left( \frac{\theta_s^2 + \theta_{b, \text{H92}\alpha}^2}{\theta_s^2 + \theta_{b, \text{H91}\alpha}^2} \right). \quad (\text{A40})$$

W3 is unresolved in their survey, so  $\theta_s^2 + \theta_b^2 \simeq \theta_b^2$ . Using  $\theta_b^2 \propto \nu^{-2}$  for a Gaussian beam, this factor becomes

$$\frac{T_{L, \text{H91}\alpha}}{T_{L, \text{H92}\alpha}} \simeq \left( \frac{\nu_{\text{H91}\alpha}}{\nu_{\text{H92}\alpha}} \right) = 1.033. \quad (\text{A41})$$

Therefore, the average RRL antenna temperature in their surveys is

$$\begin{aligned} \langle T_L(\nu_L) \rangle &= \frac{1}{2} (T_{L, \text{H91}\alpha} + 1.033 T_{L, \text{H92}\alpha}) \\ \langle T_L(\nu_L) \rangle &= 292.235 \eta_b \left( \frac{T_e}{\text{K}} \right)^{-1.5} \left( \frac{n_e n_p}{\text{cm}^{-6}} \right) \left( \frac{\Delta V}{\text{km s}^{-1}} \right)^{-1} l \\ &\quad \times \left[ \left( \frac{\nu_{\text{H91}\alpha}}{\text{GHz}} \right)^{-1} \left( \frac{\theta_s^2}{\theta_s^2 + \theta_{b, \text{H91}\alpha}^2} \right) + 1.033 \left( \frac{\nu_{\text{H92}\alpha}}{\text{GHz}} \right)^{-1} \left( \frac{\theta_s^2}{\theta_s^2 + \theta_{b, \text{H92}\alpha}^2} \right) \right]. \end{aligned} \quad (\text{A42})$$

The continuum antenna temperature at  $\nu_C$  is given by Equation A36, and the Quireza et al. (2006a,b)  $X$  is

$$\begin{aligned} X &= \left( \frac{T_e}{\text{K}} \right) \left[ 2.818 \times 10^{-4} \left( \frac{\nu_C}{\text{GHz}} \right)^{-2.1} \left( \frac{\Delta V}{\text{km s}^{-1}} \right) (1 + y) \left( \frac{\langle\nu_L\rangle}{\text{GHz}} \right)^{1.1} \right]^{0.87} \\ &\quad \times \left[ \left( \frac{\nu_{\text{H91}\alpha}}{\text{GHz}} \right)^{-1} \left( \frac{\theta_s^2 + (\theta_b^*)^2}{\theta_s^2 + \theta_{b, \text{H91}\alpha}^2} \right) + 1.033 \left( \frac{\nu_{\text{H92}\alpha}}{\text{GHz}} \right)^{-1} \left( \frac{\theta_s^2 + (\theta_b^*)^2}{\theta_s^2 + \theta_{b, \text{H92}\alpha}^2} \right) \right]^{-0.87}. \end{aligned} \quad (\text{A43})$$

The ratio of this  $X$  approximation to  $X_{\text{true}}$  is

$$\begin{aligned} \frac{X}{X_{\text{true}}} &= 1.829 \left( \frac{\nu_C}{\text{GHz}} \right)^{-1.827} \left( \frac{\langle\nu_L\rangle}{\text{GHz}} \right)^{0.957} \\ &\quad \times \left[ \left( \frac{\nu_{\text{H91}\alpha}}{\text{GHz}} \right)^{-1} \left( \frac{\theta_s^2 + (\theta_b^*)^2}{\theta_s^2 + \theta_{b, \text{H91}\alpha}^2} \right) + 1.033 \left( \frac{\nu_{\text{H92}\alpha}}{\text{GHz}} \right)^{-1} \left( \frac{\theta_s^2 + (\theta_b^*)^2}{\theta_s^2 + \theta_{b, \text{H92}\alpha}^2} \right) \right]^{-0.87}. \end{aligned} \quad (\text{A44})$$

Quireza et al. (2006a) and Quireza et al. (2006b) did not account for the variation in telescope beam size in their analysis. Therefore, their ratio  $X/X_{\text{true}}$  has a dependence on the source size. In the limit that the source is unresolved



at all frequencies,  $\theta_s^2 \ll \theta_b^2$ . For Gaussian beams with  $\theta^2 \propto \nu^{-2}$ , the ratio in this limit becomes

$$\begin{aligned} \lim_{\theta_s^2 \ll \theta_b^2} \frac{X}{X_{\text{true}}} &= 1.829 \left( \frac{\nu_C}{\text{GHz}} \right)^{-1.827} \left( \frac{\langle \nu_L \rangle}{\text{GHz}} \right)^{0.957} \\ &\quad \times \left[ \left( \frac{\nu_{\text{H91}\alpha}}{\text{GHz}} \right)^{-1} \left( \frac{(\theta_b^*)^2}{\theta_{b, \text{H91}\alpha}^2} \right) + 1.033 \left( \frac{\nu_{\text{H92}\alpha}}{\text{GHz}} \right)^{-1} \left( \frac{(\theta_b^*)^2}{\theta_{b, \text{H92}\alpha}^2} \right) \right]^{-0.87} \\ \lim_{\theta_s^2 \ll \theta_b^2} \frac{X}{X_{\text{true}}} &= 1.829 \left( \frac{\nu_C}{\text{GHz}} \right)^{-1.827} \left( \frac{\langle \nu_L \rangle}{\text{GHz}} \right)^{0.957} \\ &\quad \times \left[ \left( \frac{\nu_{\text{H91}\alpha}}{\text{GHz}} \right)^{-1} \left( \frac{\nu_{\text{H91}\alpha}^2}{\nu_C^2} \right) + 1.033 \left( \frac{\nu_{\text{H92}\alpha}}{\text{GHz}} \right)^{-1} \left( \frac{\nu_{\text{H92}\alpha}^2}{\nu_C^2} \right) \right]^{-0.87} \\ \lim_{\theta_s^2 \ll \theta_b^2} \frac{X}{X_{\text{true}}} &= 1.829 \left( \frac{\nu_C}{\text{GHz}} \right)^{-0.087} \left( \frac{\langle \nu_L \rangle}{\text{GHz}} \right)^{0.957} \left[ \left( \frac{\nu_{\text{H91}\alpha}}{\text{GHz}} \right) + 1.033 \left( \frac{\nu_{\text{H92}\alpha}}{\text{GHz}} \right) \right]^{-0.87}. \end{aligned} \quad (\text{A45})$$

Using the RRL frequencies,  $\nu_C = 8.665 \text{ GHz}$ , and  $\langle \nu_L \rangle = \nu_{\text{H91}\alpha}$ , which is what [Quiroza et al. \(2006a,b\)](#) use, we find

$$\lim_{\theta_s^2 \ll \theta_b^2} \frac{X}{X_{\text{true}}} = 1.0. \quad (\text{A46})$$

For unresolved sources, [Quiroza et al. \(2006a,b\)](#) correctly calculate the electron temperatures in their C II survey. In the resolved case,  $\theta_s^2 \gg \theta_b^2$  and

$$\begin{aligned} \lim_{\theta_s^2 \gg \theta_b^2} \frac{X}{X_{\text{true}}} &= 1.829 \left( \frac{\nu_C}{\text{GHz}} \right)^{-1.827} \left( \frac{\langle \nu_L \rangle}{\text{GHz}} \right)^{0.957} \left[ \left( \frac{\nu_{\text{H91}\alpha}}{\text{GHz}} \right)^{-1} + 1.033 \left( \frac{\nu_{\text{H92}\alpha}}{\text{GHz}} \right)^{-1} \right]^{-0.87} \\ \lim_{\theta_s^2 \gg \theta_b^2} \frac{X}{X_{\text{true}}} &= 0.956. \end{aligned} \quad (\text{A47})$$

Therefore, the [Quiroza et al. \(2006b\)](#) electron temperatures for the C II survey nebulae are underestimated by up to 5% depending on the source morphology.

In their  $^3\text{He}$  survey, [Quiroza et al. \(2006a,b\)](#) only observe the H91 $\alpha$  transition. The  $X$  ratio for this survey is simpler:

$$\frac{X}{X_{\text{true}}} = \left( \frac{\nu_C}{\text{GHz}} \right)^{-1.827} \left( \frac{\nu_{\text{H91}\alpha}}{\text{GHz}} \right)^{1.827} \left( \frac{\theta_s^2 + (\theta_b^*)^2}{\theta_s^2 + \theta_{b, \text{H91}\alpha}^2} \right)^{-0.87}, \quad (\text{A48})$$

with limits

$$\begin{aligned} \lim_{\theta_s^2 \ll \theta_b^2} \frac{X}{X_{\text{true}}} &= \left( \frac{\nu_C}{\text{GHz}} \right)^{-1.827} \left( \frac{\nu_{\text{H91}\alpha}}{\text{GHz}} \right)^{1.827} \left( \frac{(\theta_b^*)^2}{\theta_{b, \text{H91}\alpha}^2} \right)^{-0.87} \\ &= \left( \frac{\nu_C}{\text{GHz}} \right)^{-0.087} \left( \frac{\nu_{\text{H91}\alpha}}{\text{GHz}} \right)^{0.087} \\ \lim_{\theta_s^2 \ll \theta_b^2} \frac{X}{X_{\text{true}}} &= 1.0 \end{aligned} \quad (\text{A49})$$

and

$$\begin{aligned} \lim_{\theta_s^2 \gg \theta_b^2} \frac{X}{X_{\text{true}}} &= \left( \frac{\nu_C}{\text{GHz}} \right)^{-1.827} \left( \frac{\nu_{\text{H91}\alpha}}{\text{GHz}} \right)^{1.827} \\ \lim_{\theta_s^2 \gg \theta_b^2} \frac{X}{X_{\text{true}}} &= 0.983. \end{aligned} \quad (\text{A50})$$

[Quiroza et al. \(2006b\)](#) underestimate their electron temperatures by up to 2% in their  $^3\text{He}$  survey.

In Table 7 we list the  $X/X_{\text{true}}$  factors for the [Quiroza et al. \(2006a\)](#), [Quiroza et al. \(2006b\)](#), [Balser et al. \(2011\)](#), and B15 single dish studies. For each survey, we list the author; the observed RRL transitions; the observed continuum frequency; the average RRL frequency they used in the electron temperature equation; and the  $X/X_{\text{true}}$  factor.

**Table 7.** Single Dish Electron Temperature Corrections

Author	RRLs	$\nu_C$	$< \nu_L >^a$	$X/X_{\text{true}}$
		GHz	GHz	
Quireza et al. (2006a,b) C II Survey	H91 $\alpha$ ;H92 $\alpha$	8.665	8.585	0.956 to 1.0
Quireza et al. (2006a,b) $^3\text{He}$ Survey	H91 $\alpha$	8.665	8.585	0.983 to 1.0
Balser et al. (2011, 2015)	H87 $\alpha$ to H93 $\alpha$	8.665	9.0	1.057

<sup>a</sup> Average RRL frequency used by the author, which is not the actual average RRL frequency

### A.3. Interferometer Observations

Interferometers measure intensity in units of flux density per synthesized beam,  $S$ , which is related to brightness temperature,  $T_B$ , by the Rayleigh-Jeans law:

$$S = \frac{2kc^2}{\nu^2} T_B. \quad (\text{A51})$$

If the RRL and continuum flux densities are measured at the same frequency, with the same telescope, and with the same synthesized beam size, the RRL-to-continuum flux density ratio and electron temperature are given by Equations A16 and A17, respectively, where  $I_C$  is the continuum flux density and  $I_L$  is the RRL flux density.

### A.4. Averaging Interferometer RRLs

An important difference between interferometric observations and single dish observations is that interferometers measure the RRL and continuum emission simultaneously. At each RRL frequency, we measure the RRL flux density and continuum flux density with the same synthesized beam. If the source is homogeneous and isothermal, we can ignore all effects of the varying beam size.

In our VLA survey analysis, we extract spectra from our data cubes in two ways: from the pixel of brightest continuum emission, such that the spectrum has units of flux density per beam, or from the sum of all pixels within a region, such that the spectrum has units of flux density. We average these spectra weighted by the continuum brightness and rms noise in the line-free regions, so our interferometric  $X$  factor is

$$X = \left[ \left( \frac{\langle S_C(\nu_L) \rangle^*}{\langle S_L(\nu_L) \rangle^*} \right) \left( \frac{\langle \nu_L \rangle^*}{\text{GHz}} \right)^{1.1} \right]^{0.87}, \quad (\text{A52})$$

where  $S_C$  and  $S_L$  are the continuum and RRL brightness or flux density, respectively, and  $\langle \rangle^*$  indicates a weighted average. If we assume that the spectral rms noise is the same in each RRL transition, then the weighted average values are simply

$$\langle S_C(\nu_L) \rangle^* = \frac{\sum_i S_C^2(\nu_{L,i})}{\sum_i S_C(\nu_{L,i})} \quad (\text{A53})$$

$$\langle S_L(\nu_L) \rangle^* = \frac{\sum_i S_L(\nu_{L,i}) S_C(\nu_{L,i})}{\sum_i S_C(\nu_{L,i})} \quad (\text{A54})$$

$$\langle \nu_L \rangle^* = \frac{\sum_i \nu_{L,i} S_C(\nu_{L,i})}{\sum_i S_C(\nu_{L,i})}. \quad (\text{A55})$$

From Equations A2 and A51, the continuum brightness at the  $i$ th RRL frequency is

$$S_C(\nu_{L,i}) = \frac{2k\nu_{L,i}^2}{c^2} T_e \tau_C(\nu_{L,i})$$

$$\frac{S_C(\nu_{L,i})}{\text{Jy sr}^{-1}} = 2.530 \times 10^3 \left( \frac{T_e}{\text{K}} \right)^{-0.35} \left( \frac{\nu_{L,i}}{\text{GHz}} \right)^{-0.1} \left( \frac{n_i n_e}{\text{cm}^{-6}} \right) \left( \frac{l}{\text{pc}} \right) \quad (\text{A56})$$

for a homogeneous nebula with depth  $l$ . The RRL frequency is the only factor that depends on RRL transition, so

$$\sum_i \frac{S_C(\nu_{L,i})}{\text{Jy sr}^{-1}} = 2.530 \times 10^3 \left( \frac{T_e}{\text{K}} \right)^{-0.35} \left( \frac{n_i n_e}{\text{cm}^{-6}} \right) \left( \frac{l}{\text{pc}} \right) \sum_i \left( \frac{\nu_{L,i}}{\text{GHz}} \right)^{-0.1} \quad (\text{A57})$$

and

$$\begin{aligned} \frac{\langle S_C(\nu_L) \rangle^*}{\text{Jy sr}^{-1}} &= 2.530 \times 10^3 \left( \frac{T_e}{\text{K}} \right)^{-0.35} \left( \frac{n_i n_e}{\text{cm}^{-6}} \right) \left( \frac{l}{\text{pc}} \right) \\ &\times \left[ \sum_i \left( \frac{\nu_{L,i}}{\text{GHz}} \right)^{-0.2} \right] \left[ \sum_i \left( \frac{\nu_{L,i}}{\text{GHz}} \right)^{-0.1} \right]^{-1}. \end{aligned} \quad (\text{A58})$$

Using Equations A8 and A51, the LTE brightness of the  $i$ th RRL is

$$\begin{aligned} S_L(\nu_{L,i}) &= \frac{2k\nu_{L,i}^2}{c^2} T_e \tau_L^*(\nu_{L,i}) \\ \frac{S_L(\nu_{L,i})}{\text{Jy sr}^{-1}} &= 1.796 \times 10^7 \left( \frac{T_e}{\text{K}} \right)^{-1.5} \left( \frac{\nu_{L,i}}{\text{GHz}} \right) \left( \frac{n_p n_e}{\text{cm}^{-6}} \right) \left( \frac{\Delta V}{\text{km s}^{-1}} \right)^{-1} \left( \frac{l}{\text{pc}} \right) \end{aligned} \quad (\text{A59})$$

for a homogeneous medium with depth  $l$ . The average RRL brightness is

$$\begin{aligned} \frac{\langle S_L(\nu_L) \rangle^*}{\text{Jy sr}^{-1}} &= 1.796 \times 10^7 \left( \frac{T_e}{\text{K}} \right)^{-0.5} \left( \frac{n_p n_e}{\text{cm}^{-6}} \right) \left( \frac{\Delta V}{\text{km s}^{-1}} \right)^{-1} \left( \frac{l}{\text{pc}} \right) \\ &\times \left[ \sum_i \left( \frac{\nu_{L,i}}{\text{GHz}} \right)^{0.9} \right] \left[ \sum_i \left( \frac{\nu_{L,i}}{\text{GHz}} \right)^{-0.1} \right]^{-1}. \end{aligned} \quad (\text{A60})$$

The average RRL frequency is

$$\frac{\langle \nu_L \rangle^*}{\text{GHz}} = \left[ \sum_i \left( \frac{\nu_{L,i}}{\text{GHz}} \right)^{0.9} \right] \left[ \sum_i \left( \frac{\nu_{L,i}}{\text{GHz}} \right)^{-0.1} \right]^{-1}, \quad (\text{A61})$$

so the interferometric  $X$  approximation simplifies to

$$X = \left( \frac{T_e}{\text{K}} \right) \left[ 1.409 \times 10^{-4} \left( \frac{\Delta V}{\text{km s}^{-1}} \right) (1 + y) \left( \frac{\sum_i \nu_{L,i}^{-0.2}}{\sum_i \nu_{L,i}^{0.9}} \right) \left( \frac{\sum_i \nu_{L,i}^{0.9}}{\sum_i \nu_{L,i}^{-0.1}} \right)^{1.1} \right]^{0.87}. \quad (\text{A62})$$

The ratio of this approximation to  $X_{\text{true}}$  is

$$\frac{X}{X_{\text{true}}} = \left[ \left( \frac{\sum_i \nu_{L,i}^{-0.2}}{\sum_i \nu_{L,i}^{0.9}} \right) \left( \frac{\sum_i \nu_{L,i}^{0.9}}{\sum_i \nu_{L,i}^{-0.1}} \right)^{1.1} \right]^{0.87} \quad (\text{A63})$$

We observe the seven RRL transitions from H87 $\alpha$  to H93 $\alpha$ . Our  $X$  factor ratio is thus

$$\frac{X}{X_{\text{true}}} = 1.0 \quad (\text{A64})$$

Our strategy for averaging multiple RRL transitions to compute electron temperatures is accurate.